RECONFIGURABLE RESONANT AND LEAKY-WAVE ANTENNAS FOR FUTURE WIRELESS SYSTEMS

by

Shu-Lin Chen

Supervisor: **Prof. Yingjie Jay Guo**

Co-supervisor: **Dr Pei-Yuan Qin**

Dissertation submitted in fulfilment of the requirements

for the degree of

DOCTOR OF PHILOSOPHY

School of Electrical and Data Engineering
Faculty of Engineering and Information Technology
University of Technology Sydney
Sydney, NSW 2007, Australia

July 2019

ABSTRACT

Reconfigurable antennas (RAs), which have agilities in their frequency and radiation characteristics, are emerging as one of the key enabling components for wireless systems. Compared with single-function legacy antennas, RAs can greatly enhance the system functionalities and flexibilities. In this dissertation, on the basis of state-of-the-art of RAs, a thorough investigation, development, and implementation are conducted on reconfigurable resonant and leaky-wave antennas to fully exploit and extend the benefits of RAs.

In order to enable advanced technologies for reconfigurable resonant antennas, challenging and promising gaps associated with novel designs are addressed on polarization-reconfigurable antenna, pattern-reconfigurable antenna, as well as combined polarization- and pattern-reconfigurable antenna. In particular, a reconfigurable center-fed shorting-via loaded patch antenna is designed that can switch among four linear polarizations at a 45° rotation. Furthermore, by reconfiguring parasitic striplines and bottom reflecting metal pieces around a radiating dipole, five switchable beams including broadside, titled, and endfire directions, are achieved. Finally, a cavity-backed proximity-coupled patch antenna operating at 11 GHz is designed and reconfigured to switch among three linear polarizations, and its main beam can be steered to about $+20°$, $0°$, $-20°$ with a measured gain variation between 7.2 and 8.1 dBi for each polarization.

As one of the most widely used types of non-resonant antennas, leaky-wave antennas (LWAs) serially leak power through open traveling-wave structures, and they generally have inherent beam scanning capability by sweeping the source frequency. One main challenge in LWAs is to realize a wide-angle continuous

circular-polarization (CP) beam scan. A novel benzene-ring-shaped slot-loaded CP substrate-integrated-waveguide LWA with partially reflecting wall vias is developed herein to scan a CP beam from -42.8° to $+54.3^\circ$ with a gain variation of only 3.3 dBic. Moreover, a polarization reconfigurable LWA that can switch between its circular-polarization and linear-polarization states is investigated and accomplished to further improve the diversity and functionality delivered by the LWA system. Finally, to eliminate the frequency-dependant beam scanning behaviour, a reconfigurable composite right/left-handed (CRLH) LWA is developed that facilitates fixed-frequency continuous beam scanning over a wide operational frequency band.

Since the wireless systems are evolving towards multi-functionality to enable fast, secure, and reliable connections, it is believed that the developed reconfigurable resonant and leaky-wave antennas can find wide applications in current and beyond wireless systems.

CERTIFICATE OF ORIGINAL AUTHORSHIP

I, Shu-Lin Chen declare that this thesis, is submitted in fulfilment of the requirements for the award of the degree of DOCTOR OF PHILOSOPHY, in the Faculty of Engineering and Information Technology at the University of Technology Sydney.

This thesis is wholly my own work unless otherwise reference or acknowledged. In addition, I certify that all information sources and literature used are indicated in the thesis.

This document has not been submitted for qualifications at any other academic institution.

This research is supported by the Australian Government Research Training Program.

Production Note:
Signature: Signature removed prior to publication.

Date: 29/07/2019

ACKNOWLEDGMENTS

My three years of doctoral study at University of Technology Sydney (UTS), Australia have seemed like a second. At this final stage of my study career, thousands of words fill my mind.

I would like to express my deepest appreciation and gratitude to my supervisor, Prof Y. Jay Guo. He has provided me the opportunity and invaluable guidance in pursuing my doctoral degree. Prof Guo is expert in various fields including antennas and wireless communications. As a senior professor, he is always thoughtful and resourceful in providing me with helpful suggestions and effective ideas for my research. Moreover, I have been profoundly touched by Prof Guo's kind, friendly, generous, and considerate nature, which inspires and motivates me.

I would like to express the sincere appreciation and gratitude to my co-supervisor, Dr Pei-Yuan Qin. He introduced me to UTS for the first time, and helped me apply for the doctoral study. Without his help and support, I would not even have had the chance to study at UTS. As co-supervisor, he is always friendly and patient in discussing my research problems.

I would like to express the sincere appreciation and gratitude to Prof Richard W. Ziolkowski, an idol in the lab due to his hard and consistent working with "7-11", for his thoroughness and precision in research, and also for his kindness and modest approach to life. His "why" questions have pushed me into a more insightful research and understanding. I am sincerely grateful for all his guidance and support.

I would like to express the sincere appreciation and gratitude to Dr Debabrata K. Karmokar. He guided me with the research on the leaky-wave antennas. He is always helpful, and provides lots of interesting and useful ideas. I am indeed lucky to work with him.

I would like to express the sincere appreciation and gratitude to Prof Bevan Jones. He is not only teaching me his knowledge but also brings me many classic books that help my understanding. Moreover, I deeply thank him for his careful and thorough proofreading for this thesis. I would also like to acknowledge Prof Trevor S. Bird. He is extremely kind, and also knowledgable to give valuable and critical suggestions on my research.

I would like to extend my gratitude to Prof Zheng Li, Prof Yanhui Liu, and Dr Wei Lin for their consistent support, advice and encouragement on my work.

I would like to thank Prof Xi Chen, Prof Jianquan Huang, Dr Xi Yang, and all other members of the Electromagnetic Informatics Lab (EIL) at Global Big Data Technologies Centre (GBDTC), especially, Dr Ding Can, Dr He Zhu, Haihan Sun, Tianyu Yang, Lizhao Song, Jiwei Lian, Xuan Wang, Ming Li for their kind help and support.

I believe Love is one of the most important chapters in our life. I would like to sincerely thank Anna Tu for her earnest and generous love. We spent beautiful and unforgettable days together in London and Xiamen, etc.. You well, sun shine!

Finally, I am forever thankful, indebted to my parents (Yicheng Chen & Defeng Luo) and my brother (Zhulin Chen) for their consistent guidance, encouragement and love.

To My parents

&

Brother and sister

Contents

Abstract **iii**

Acknowledgments **ix**

Table of Contents **xiii**

List of Figures **xix**

List of Tables **xxix**

Acronyms **xxxi**

1 Introduction **1**

1.1 Motivation and Scope 2

1.2 Organisation of the Thesis 3

1.3 Contributions 5

1.4 Publications 8

2 Background and State-of-the-Art **13**

2.1 Resonant Antennas 13

2.1.1 Basic Characteristics 13

2.1.2 Dipole Antenna 14

2.2 Non-Resonant Antennas 15
2.2.1 Basic Characteristics 15
2.2.2 Leaky-Wave Antenna 15
2.3 State-of-the-Art 17
2.3.1 Multi-Linear Polarization-Reconfigurable Resonant Antenna 17
2.3.2 Pattern-Reconfigurable Resonant Antenna with Switchable Beams . 19
2.3.3 Combined Polarization- and Pattern-Reconfigurable Resonant Antenna 22
2.3.4 Frequency-Based Pattern-Reconfigurable Circularly Polarized Leaky-Wave Antenna 24
2.3.5 Frequency-Based Pattern-Reconfigurable Leaky-Wave Antenna with Polarization Flexibility 27
2.3.6 Fixed-Frequency Pattern-Reconfigurable Leaky-Wave Antenna . . . 29
2.4 Summary 31

3 Multi-Linear Polarization-Reconfigurable Patch Antenna 33

3.1 Center-Fed Circular Patch Antenna with a Shorting Post 34
3.1.1 Antenna Configuration 34
3.1.2 Cavity Mode Analysis 34
3.1.3 Parameter Study and Discussions 36
3.1.4 Fabrication and Measurement 38
3.2 Multi-Linear Polarization Reconfigurable Antenna with Shorting Posts . . 40
3.2.1 Antenna Configuration and Analysis 40
3.2.2 Fabrication and Measurement 43
3.3 Conclusion 45

4 Pattern-Reconfigurable Dipole Antenna with Switchable Beams in the

Elevation Plane **47**

4.1 Antenna Design and Analysis 48

4.1.1 Antenna Configuration 48

4.1.2 Pattern Reconfiguration Mechanism 51

4.1.3 DC Feed Network 53

4.2 Results and Discussion 54

4.3 Conclusion 58

5 Combined Polarization- and Pattern-Reconfigurable Proximity-Coupled Patch Antenna **59**

5.1 Reconfigurable Antenna Design and Analysis 60

5.1.1 Antenna Configuration 60

5.1.2 Polarization Reconfiguration and Beam Steering Mechanism 63

5.1.3 DC Feed Network Design 65

5.2 Parameter Study and Discussion 67

5.3 Results and Discussion 70

5.4 Conclusion 74

6 Frequency-Based Pattern-Reconfigurable Circularly Polarized Leaky-Wave Antenna **75**

6.1 Unit Cell Requirements to Achieve Continuous Beam Scanning 76

6.2 I-Shaped Slot-Loaded SIW LWA with PRW Vias 82

6.2.1 Antenna Configuration 82

6.2.2 Beam Scanning 83

6.2.3 Circular Polarization Analysis 83

6.3 Benzene-Ring-Shaped Slot-Loaded SIW CP LWA with PRW Vias 87

6.3.1 Antenna Configuration 87

6.3.2 Design Parameter Study . . . 88
6.3.3 Simulated and Measured Results . . . 91
6.4 Discussion . . . 95
6.5 Conclusion . . . 96

7 Frequency-Based Pattern-Reconfigurable Leaky-Wave Antenna with Polarization Flexibility 97

7.1 Frequency-Based Beam Steerable CP LWA . . . 98
7.1.1 Antenna Configuration . . . 98
7.1.2 Working Mechanisms . . . 100
7.1.3 Simulated and Measured Results . . . 102
7.2 Frequency-Based Beam Steerable LP LWA . . . 106
7.2.1 Antenna Configuration and Analysis . . . 107
7.2.2 Simulated and Measured Results . . . 109
7.3 Polarization-Reconfigurable Frequency-Based Continuous Beam Scanning LWA . . . 112
7.3.1 Polarization-Reconfigurable LWA Working in Its CP State . . . 115
7.3.2 Polarization-Reconfigurable LWA Working in Its LP State . . . 119
7.4 Conclusion . . . 123

8 Fixed-Frequency Pattern-Reconfigurable Leaky-Wave Antenna 125

8.1 Theory . . . 126
8.2 Frequency-Based Continuous Beam Scanning CRLH LWA . . . 132
8.3 Fixed-Frequency Continuous Beam Scanning CRLH LWA . . . 136
8.3.1 Antenna Configuration . . . 136
8.3.2 DC Biasing Strategy . . . 139
8.4 Results and Discussion . . . 140

8.4.1 Simulated Results 140
8.4.2 Measured Results 144
8.4.3 Discussion 148
8.5 Conclusion 150

9 Conclusions and Future Work **153**
9.1 Conclusions 153
9.2 Future Work 155

10 Calculation of Phase Constant from T-Type Circuit Parameters **157**

Bibliography **159**

List of Figures

2.1 Configuration of the half-wavelength dipole antenna. 14

2.2 Configuration of the periodic slot-loaded SIW LWA reported in [20]. This is an example of the periodic LWA. 16

2.3 Top view of the six-linear polarization switching patch antenna reported in [36]. 18

2.4 Configuration of the circular patch antenna with four bow-tie shaped slots reported in [37]. 19

2.5 A schematic of unmanned aerial vehicle (UAV) communications. 20

2.6 Antenna configuration loaded with PIN diodes reported in [54]. Left: transverse plane of waveguide with only vertical reflector and slot 1 radiating. Right: longitudinal plane of waveguide with only slots, diodes and reflector. 21

2.7 Reconfigurable conformal antenna array. 23

2.8 Prototype of the combined polarization and pattern reconfigurable reported in [65]. 24

2.9 Configuration of slot-loaded periodic SIW CP LWA reported in [83]. (a) Unit cell. (b) Complete LWA. (c) Prototype. 26

2.10 Configuration of polarization flexible SIW-based CRLH LWA reported in [97]. 29

2.11 Configuration of reconfigurable 2-bit microstrip line LWA reported in [105]. 30

3.1 Geometry of the center-fed circular patch antenna with a shorting post. . 35
3.2 Current distribution of the center-fed circular patch antenna at 2.45 GHz. (a) Without a shorting post. (b) With a shorting post along x axis. . . . 36
3.3 Input reflection coefficients. (a) Varying with the outer patch radius R. (b) Varying with the inner patch radius R_r. 38
3.4 Input reflection coefficients. (a) Varying with the ring slot width w_s. (b) Varying with the shorting post radius r. 38
3.5 Simulated and measured input reflection coefficients of the center-fed circular patch antenna with a shorting post. 39
3.6 Simulated and measured radiation patterns at 2.45 GHz. (a) E plane. (b) H plane. 39
3.7 Geometry of the multi-linear polarization reconfigurable antenna with shorting posts. (a) $\phi = 67.5°$ side view. (b) Top view of the patch layer. (c) Top view of the biasing layer. 41
3.8 Top view of the multi-linear polarization reconfigurable antenna prototype with shorting posts. (a) Patch layer. (b) Biasing layer. 44
3.9 Simulated and measured input reflection coefficients of the multi-linear polarization reconfigurable antenna with shorting posts. (a) $\phi = 0°$ and $\phi = 135°$. (b) $\phi = 45°$ and $\phi = 90°$ polarizations. 44
3.10 Simulated and measured radiation patterns for $\phi = 0°$ polarization at 2.45 GHz. (a) E plane. (b) H plane. 45

4.1 Geometry of the developed pattern reconfigurable antenna. (a) Overall view. (b) Front view. 49
4.2 Bottom view of the radiating layer. 50
4.3 Top view of the reflecting layer. 50
4.4 Configuration of the feed substrate. (a) Front view. (b) Back view. 51

4.5 Photograph of the fabricated antenna prototype. 55
4.6 Simulated and measured reflection coefficients. (a) Mode 1. (b) Mode 2 and Mode 4. (c) Mode 3 and Mode 5. 56
4.7 Simulated and measured in the H-plane radiation patterns at 2.45 GHz for Mode 1 to Mode 5. (Red solid line: simulated co-pol.; Black dash line: measured co-pol.; Blue dash–dotted line: measured X-pol.) 57

5.1 Configuration of the developed cavity-backed reconfigurable microstrip antenna. 60
5.2 Top view of the patch layer. 61
5.3 Top view of the feed layer. 62
5.4 Top view of the cavity-backed ground plane. 63
5.5 Demonstration of beam steering mechanism. (a) Three-element array. (b) Pattern modes. 64
5.6 Input reflection coefficients versus feed line width of W_d for different working modes. 67
5.7 Realized gains and cross-polarization levels versus parasitic line length of L_1 for different working modes. (a) Realized gains. (b) Cross-polarization levels. 68
5.8 Realized gains and cross-polarization levels versus distance of d_{H} for different working modes. (a) Realized gains. (b) Cross-polarization levels. 69
5.9 Prototype of the developed cavity-backed reconfigurable microstrip antenna. (a)Top view. (b) Overall view. 70
5.10 Simulated and measured $|S_{11}|$ at 11 GHz for all the nine working modes. . 71

5.11 Simulated and measured H-plane radiation patterns at 11 GHz for all the nine working modes. (a) Mode 1. (b) Mode 2. (c) Mode 3. (d) Mode 4. (e) Mode 5. (f) Mode 6. (g) Mode 7. (h) Mode 8. (i) Mode 9. 72

6.1 Top view of the unit cell, Unit A, and its corresponding equivalent circuit. 77

6.2 Dispersion diagrams of the Unit A model obtained with equivalent circuit and eigenmode simulations. 79

6.3 Unit B model and its corresponding equivalent circuit. 80

6.4 Unit B dispersion diagrams obtained from its equivalent circuit and eigenmode simulation. 81

6.5 I-shaped slot-loaded SIW LWA with PRW vias configuration. 82

6.6 Main beam angle when the source frequency is varied as calculated from the simulations of the eigenmode (infinite) and complete (finite) structure. 84

6.7 Simulated directivity and axial ratio values of the six-cell I-shaped slot-loaded SIW LWA with PRW vias. 84

6.8 Top view of the field distribution on the Unit B at 10.5 GHz. (a) E-fields distribution ($t = 0$). (b) H-field distribution ($t = 0$). (c) E-fields distribution ($t = \pi/4$). (d) H-fields distribution ($t = \pi/4$). 85

6.9 Unit B radiation mechanism analysis. (a) E-fields distribution. (b) Equivalent magnetic current sources. 86

6.10 Benzene-ring-shaped slot-loaded SIW CP LWA with PRW vias. (a) Evolution of Unit C from Unit B. (b) Complete six-cell based structure. 87

6.11 The axial ratio (AR) values as a function of the source frequency for different values of W_{b1}. 89

6.12 The axial ratio (AR) values as a function of the source frequency for different values of W_{b2}. 89

6.13 The axial ratio (AR) as a function of the source frequency for different values of D_2. 90
6.14 Photograph of the fabricated benzene-ring-shaped slot-loaded CP SIW LWA with PRW vias prototype. 91
6.15 Simulated and measured S-parameters of the benzene-ring-shaped slot-loaded CP SIW LWA with PRW vias. 92
6.16 Simulated gain patterns of the optimized design at five different frequencies. 93
6.17 Simulated 3-D gain pattern of the optimized design at 9.8 GHz. 93
6.18 Measured gain patterns of the prototype at five different frequencies. . . . 94
6.19 Simulated and measured axial ratio (AR) values together with the corresponding realized gain values as functions of the source frequency. 95

7.1 Top view of the CP LWA. Photograph of the prototype antenna is shown in the bottom inset. 99
7.2 Dispersion diagrams of the $n = -1$ and 0 spatial harmonics and the unit cell configuration of the CP LWA. 100
7.3 Top view of E-field distribution on the surface just above one unit cell of the main patch of the optimized CP LWA at 2.8 GHz for four time snapshots separated by a quarter period. 101
7.4 Measured and simulated S-parameters of the optimized CP LWA. 103
7.5 Simulated radiation patterns of the CP LWA at five frequencies within its bandwidth. Solid line: Co-polarization (LHCP); Dash line: Cross-polarization (RHCP). 104
7.6 Simulated 3-D realized gain patterns of the CP LWA at three frequencies within its operating bandwidth: (a) 2.65, (b) 2.955, and (c) 3.25 GHz. . . . 104

7.7 Measured radiation patterns of the CP LWA at five frequencies within its bandwidth. Solid line: Co-polarization (LHCP); Dash line: Cross-polarization (RHCP). 105
7.8 Measured and simulated realized gain and axial ratio values of the CP LWA as functions of the source frequency. 106
7.9 Top view of the shorted-stub loaded LP LWA. Photograph of the prototype antenna is shown in the bottom inset. 107
7.10 Top view of E-field distribution on the surface just above one unit cell of the main patch of the optimized LP LWA at 2.8 GHz for four time snapshots separated by a quarter period. 108
7.11 Measured and simulated S-parameters of the optimized LP LWA. 109
7.12 Simulated radiation patterns of the LP LWA at five frequencies within its bandwidth. Solid line: Co-polarization; Dash line: Cross-polarization. . . . 110
7.13 Measured radiation patterns of the LP LWA at five frequencies within its bandwidth. Solid line: Co-polarization; Dash line: Cross-polarization. . . . 111
7.14 Measured and simulated realized gain and cross polarization (cross pol.) values of the LP LWA as functions of the source frequency. 111
7.15 Top view of the polarization-reconfigurable LWA. The bottom left inset shows the shorted stubs and the right inset shows the diode placements and biasing arrangements. 112
7.16 Photograph of the fabricated polarization-reconfigurable LWA prototype. . 114
7.17 Measured and simulated S-parameters of the optimized polarization reconfigurable LWA operating in its CP state. 115
7.18 Simulated radiation patterns of the optimized polarization-reconfigurable LWA at five frequencies within its CP bandwidth. Solid line: Co-polarization (LHCP); Dash line: Cross-polarization (RHCP). 116

7.19 Measured radiation patterns of the optimized polarization-reconfigurable LWA at five frequencies within its CP bandwidth. Solid line: Co-polarization (LHCP); Dash line: Cross-polarization (RHCP). 117
7.20 Simulated AR values as functions of the observation angle at five operating frequencies for the optimized polarization-reconfigurable LWA in its CP state. 117
7.21 Measured AR values as functions of the observation angle at five operating frequencies for the optimized polarization-reconfigurable LWA in its CP state. 118
7.22 Measured and simulated realized gain and axial ratio values of the optimized polarization-reconfigurable LWA operating in its CP state as functions of the source frequency. 118
7.23 Simulated total efficiency of the optimized polarization-reconfigurable LWA operating in its CP and LP states. 119
7.24 Measured and simulated S-parameters of the optimized polarization reconfigurable LWA operating in its LP state. 120
7.25 Simulated radiation patterns of the optimized polarization-reconfigurable LWA at five frequencies within its LP bandwidth. Solid line: Co-polarization; Dash line: Cross-polarization. 121
7.26 Measured radiation patterns of the optimized polarization-reconfigurable LWA at five frequencies within its LP bandwidth. Solid line: Co-polarization; Dash line: Cross-polarization. 122
7.27 Measured and simulated realized gain and cross polarization (cross pol.) values of the optimized polarization-reconfigurable LWA operating in its LP state as functions of the source frequency. 122

8.1 T-type equivalent circuit of a 1-D conventional CRLH structure. 127
8.2 Dispersion diagrams for different values of $\widetilde{L}_L$ in the equivalent CRLH circuit. 128

8.3 Dispersion diagrams for different values of $\widetilde{L}_L$ and $\widetilde{C}_L$ in the equivalent circuit. 129

8.4 Dispersion diagrams for different values of $\widetilde{L}_L$, $\widetilde{C}_L$, and $\widetilde{L}_R$ in the equivalent circuit. 131

8.5 Configuration of a single-layer frequency-based continuous beam scanning CRLH LWA. The top inset represents a unit cell of the antenna. 132

8.6 Dispersion diagrams of the unit cell of the frequency-based continuous beam scanning CRLH LWA. 134

8.7 Simulated S-parameters of the frequency-based continuous beam scanning CRLH LWA. 135

8.8 Simulated realized gain and beam angle values of the frequency-based continuous beam scanning CRLH LWA. 135

8.9 Side view (not to scale) of the developed fixed-frequency beam scanning CRLH LWA. 136

8.10 The fixed-frequency beam scanning CRLH LWA configuration. (a) Top view of the patch layer. (b) Bottom view of the ground layer. (c) Bottom view of the biasing layer. 137

8.11 A 3D view (not to scale) of the fixed-frequency beam scanning CRLH LWA without the substrates being present. 139

8.12 Capacitance values of C_{V1} and C_{V2} as functions of the simulated main beam direction at 4.75, 5, and 5.25 GHz. 141

8.13 S-parameters as functions of the simulated main beam direction at 4.75, 5, and 5.25 GHz. 142

8.14 Sidelobe level (SLL) and realized gain as functions of the simulated main beam direction at 4.75, 5, and 5.25 GHz. 142

8.15 Simulated radiation patterns for the antenna's six operating states at 5 GHz. 143

8.16 Realized gain as a function of the frequency for six operating states of the antenna at 5 GHz. 144

8.17 Photographs of the fabricated fixed-frequency beam scanning CRLH LWA prototype. (a) Before assembly. (b) After assembly. 145

8.18 Measured radiation patterns for five of the antenna's operating states at 5.0 GHz. 147

8.19 Measured radiation patterns for four of the antenna's operating states at 5.25 GHz. 148

List of Tables

3.1 Dimensions of the Center-Fed Circular Patch Antenna with a Shorting Post 37

3.2 Dimensions of the Reconfigurable Multi-Polarization Antenna with Shorting Posts. 43

3.3 Simulated and Measured Gains for Four Polarization States 45

4.1 Five Reconfigurable Working Modes 52

4.2 Optimized Values for the Parameters of the Proposed Pattern-Reconfigurable Antenna 55

4.3 Simulated Gains, Measured Gains and Half-Power Beamwidth for Five Pattern Modes 58

5.1 Nine Reconfigurable Working Modes 66

5.2 Optimized Parameters for Cavity-Backed Proximity-Coupled Reconfigurable Microstrip Antenna 67

5.3 Simulated and Measured Realized Gains for All the Nine Working Modes . 73

6.1 Optimized Design Parameters of the I-shaped Slot-loaded SIW CP LWA with PRW Vias 83

6.2 Optimized Values of the Design Parameters of the Benzene-Ring-Shaped Slot-Loaded SIW CP LWA with PRW Vias 91

7.1 Optimized Values for the CP LWA Design Parameters 102

8.1 Optimized Design Parameter Values (in Millimeters) of the Frequency-Based Continuous Beam Scanning CRLH LWA 133

8.2 Design Parameter Values of the Optimized Fixed-Frequency Beam Scanning CRLH LWA 140

8.3 Measured Performance Characteristics of the Fixed-Frequency Beam Scanning CRLH LWA Operating at 5 GHz 146

8.4 Measured Performance Characteristics of the Fixed-Frequency Beam Scanning CRLH LWA Operating at 5.25 GHz 147

8.5 Realized Gain Values for the Six Operating States with Different Values of R_{V1} and R_{V2} 149

Acronyms

AR	Axial ratio
CP	Circular-polarization
CRLH	Composite right/left-handed
EMC	Electromagnetic compatibility
EMI	Electromagnetic interference
HPBW	Half-power beamwidth
LHCP	Left-handed circular polarization
LP	Linear-polarization
LWA	Leaky-wave antenna
MIMO	Multiple-input-multiple-output
OSB	Open stopband
PRW	Partially reflecting wall
RA	Reconfigurable antenna
RHCP	Right-handed circular polarization
SIW	Substrate-integrated-waveguide
SSPP	Spoof surface plasmon polariton
UAV	Unmanned aerial vehicle
1-D	One-dimensional
3-D	three-dimensional
5G	Fifth-generation

Chapter 1

Introduction

Antennas that can radiate or receive electromagnetic waves are considered to be compulsory and key components of current as well as future wireless systems. For single-function legacy antennas their characteristics are fixed according to the particular circumstances. Such antennas severely limit the system functionality and flexibility. As opposed to these legacy antennas, reconfigurable antennas (RAs) allow modifying their characteristics by means of switching, use of active devices or other means [1]. Typical reconfigurable characteristics of an antenna are frequency, polarization, pattern or combinations of these. RAs have the potential to greatly enhance system capabilities and, hence, a large amount of research has been dedicated to the control of single characteristics as well as the combined characteristics, such as frequency-polarization, frequency-pattern, polarization-pattern and frequency-polarization-pattern. Although significant advances have been made on RAs, there are several challenging yet very promising gaps in the reported research. Some of these areas will be investigated and discussed in this dissertation.

1.1 Motivation and Scope

The future goals of the wireless systems are to provide high data-rate, multi-functional and reliable connections. For example, the emerging fifth-generation (5G) wireless systems must support a large user base, a high speed data transfer, and a huge system capacity. Massive multiple-input multiple-output (MIMO) technology is considered as providing a promising contribution to meeting these demands. This system employs a large number of service antennas at each base station to produce significant beamforming gains. Consequently, the capacity and the radiated energy efficiency can be increased by 10 times and 100 times, respectively [2, 3].

Several challenging yet critical issues arise due to the large number of the antennas. One concern is the complex RF chains associated with the adaptive processing systems. Accordingly, the costs, weight, and occupancy of the feed network will greatly increase. Another concern is the effect of mutual coupling between these antennas. Future platforms may require compact antenna arrangements and, hence, severe mutual coupling occur for these closely-spaced antennas, which may cause detrimental electromagnetic interference (EMI) and electromagnetic compatibility (EMC) problems. Furthermore, the associated heat dissipation will be a big challenge to handle for the large compact antenna system.

Reconfigurable antennas (RAs) can modify their fundamental characteristics to fit the fast-changing environment. The number of the antennas can be significantly reduced by employing the RAs rather than single-function conventional antennas while still maintaining the system capacity. Moreover, RAs can inherently deliver great diversity and multi-functionality in a cost-effective configuration. Therefore, RAs are highly promising candidates to overcome the aforementioned challenging issues for the future wireless systems [4–6].

It is recognized that for various wireless applications, different types of antennas are ap-

propriate for accommodating specific situations. Two types of antennas, that are resonant antennas and non-resonant antennas or named as traveling-wave antennas, are studied here. The resonant antennas radiate from a standing wave while the non-resonant antennas radiate from a traveling wave. Various configurations of RAs of both these types that can meet certain requirements for future wireless systems are examined in this dissertation. The reconfigurable resonant antennas, such as microstrip patch antennas and dipole antennas, and the reconfigurable non-resonant antennas, such as leaky-wave antennas, are explored, discussed and developed in this dissertation with the aim of advancing current antenna technology.

1.2 Organisation of the Thesis

This dissertation includes eight chapters. Chapters 1 and 2 are the introduction and background of the dissertation, respectively. Chapters 3 to 8 focus on each of six separate examples of RAs. Specifically, Chapters 3 to 5 focus on reconfigurable resonant antennas while Chapters 6 to 8 are concentrate on the reconfigurable LWAs. The detailed organization of each chapter is given as follows:

Chapter 1 briefly introduces the motivation and scope of reconfigurable resonant and leaky-wave antennas. Furthermore, it also presents the organization and contributions of this dissertation. The author's publication is listed in the last part of this chapter.

Chapter 2 reviews the background and state-of-the-art of the research on reconfigurable resonant and leaky-wave antennas. Basic theory and operating mechanisms of the resonant antennas and leaky-wave antennas are described. Detailed investigations on each research topic including challenges and state-of-the-art technology, are conducted.

Chapter 3 focuses on the multi-linear polarization reconfigurable patch antenna. The chapter includes designs, analyses, and fabrication details of a non-reconfigurable center-

fed circular patch antenna with a shorting post. A multi-linear polarization reconfigurable antenna is introduced based on the initial non-reconfigurable element. Simulated as well as the measured data of the fabricated reconfigurable antenna validates the desired multi-linear polarization reconfigurability.

Chapter 4 presents a pattern reconfigurable dipole antenna with switchable beams in the elevation plane using PIN diodes. Detailed antenna configuration associated with the DC biasing network for the PIN diodes is presented. Analyses of the operating mechanism for switching modes by manipulating the PIN diodes are included. The RA was fabricated and measured. The results confirm the antenna's pattern reconfigurability between broadside, titled and endfire beams.

Chapter 5 introduces a combined polarization and pattern reconfigurable proximity-coupled patch antenna. The polarization switching and beam steering mechanisms are described. A parameter study is included to investigate and optimize the antenna performance. The measured antenna prototype can select among nine different states with simultaneous polarization and pattern reconfiguration.

Chapter 6 describes a frequency-based pattern-reconfigurable circularly polarized LWA. For an initial study, an I-shaped slot-loaded SIW LWA with partially reflecting wall (PRW) vias is investigated, designed, and analysed. According to the circular polarization performance analysis on the initial I-shaped LWA, an optimized benzene-ring-shaped slot-loaded SIW CP LWA with PRW vias is developed to achieve improved CP performance over a wide angular scan range. The measured results verify that a continuously scanned CP beam through a wide angle from backward to forward directions is achieved.

Chapter 7 develops a frequency-based pattern-reconfigurable LWA with polarization flexibility. To begin with, based on the analysis of the slot-loaded SIW LWA with partially reflecting wall (PRW) vias in Chapter 6, a variation of slot-loaded SIW-based LWA is presented to attain the frequency-based CP beam scanning. A row of shorted stubs

is incorporated into this CP LWA to obtain the frequency-based LP beam scanning. Finally, a reconfigurable CP and LP frequency-based LWA is achieved by introducing PIN diodes into the LP LWA configuration. The final measured results demonstrate the both polarization and pattern reconfigurability for this frequency-based LWA.

Chapter 8 illustrates a fixed-frequency pattern-reconfigurable LWA over a wide operating band. Initially, a simple single-layer non-reconfigurable CRLH LWA is developed to realize a frequency-based continuous beam scanning. The dispersion properties of the equivalent circuit are investigated and analysed. Two sets of varactor diodes with DC biasing line are incorporated to achieve the fixed-frequency beam scanning capability. The measured results confirm the fixed-frequency continuous beam scanning performance over a wide operating band.

1.3 Contributions

The key contributions of this dissertation are advancing RA technology by utilizing novel methods or designs on both the reconfigurable resonant and leaky-wave antennas. Specific contributions are outlined below:

1. A novel method to achieve multi-linear polarization reconfiguration is developed in Chapter 3. A centre-fed circular patch antenna with a shorting post is developed through theoretical analysis and construction of a physical prototype. Accordingly, a novel multi-linear polarization reconfigurable antenna at a 45° interval is realized by using multiple sets of shorting posts and simple yet effective DC biasing networks.

2. A new and simple way to realize beam switching between broadside, titled and endfire directions is presented in Chapter 4. Simple dipole antenna is employed as the main radiator, and parasitic strips and reflecting metal pieces are reconfigured

to achieve the pattern reconfiguration. It effectively achieves the desired beam switching performance in a compact and cost-effective configuration.

3. A novel method to attain polarization agility and beam switching in a single reconfigurable antenna is developed in Chapter 5. It utilizes a novel two-layer planar microstrip structure, i.e., a combined reconfigurable proximity-coupled feed network and a parasitic-element network. The fabricated prototype can operate at any of nine different working states with a stable gain ranging from 7.2 to 8.1 dBi.

4. A novel method that incorporates both partially reflecting wall (PRW) vias and slot elements to realize wide-angle CP beam scanning is presented in Chapter 6. An equivalent circuit and equivalent radiating sources are employed to thoroughly investigate the radiation performance of this developed LWA. Subsequently, a novel benzene-ring-shaped slot-loaded CP SIW LWA with PRW vias is developed to achieve the CP beam scanning performance.

5. A novel technique that realizes both polarization agility and beam scanning functionality in a single-layer LWA is developed in Chapter 7. Three variations of LWAs, i.e., a frequency-based beam scanning CP LWA, a frequency-based beam scanning LP LWA, and a polarization reconfigurable beam scanning LWA, are presented, and prototypes of all of these antennas were fabricated and measured. The final reconfigurable LWA achieves switchable polarization states with frequency-based continuous beam scanning while maintaining a simple feed along with low-profile and easy integration properties.

6. A novel way to achieve fixed-frequency beam scanning LWA over a wide operating band is presented in Chapter 8. It conducts an in-depth analysis of the ability to tune its dispersion features through modifications of its effective circuit parameters.

Consequently, two groups of varactor diodes are incorporated into a single-layer non-reconfigurable frequency-based continuous beam scanning CRLH LWA to control its dispersion behavior. The final reconfigurable CRLH LWA prototype fulfills the required fixed-frequency beam scanning performance.

1.4 Publications

A List of Publications, including both accepted and submitted, based on research conducted during the author's candidature is given below.

Journal Articles

1. **S.-L. Chen**, D. K. Karmokar, Z. Li, P. Y. Qin, R. W. Ziolkowski, and Y. J. Guo, "Circular-Polarized Substrate-Integrated-Waveguide Leaky-Wave Antenna with Wide-Angle and Consistent-Gain Continuous Beam Scanning," *IEEE Transactions on Antennas and Propagation*, vol. 67, no. 7, pp. 4418-4428, Jul. 2019.

2. **S.-L. Chen**, P.-Y. Qin, C. Ding, and Y. J. Guo, "Cavity-Backed Proximity-Coupled Reconfigurable Microstrip Antenna with Agile Polarizations and Steerable Beams," *IEEE Transactions on Antennas and Propagation*, vol. 65, no. 10, pp. 5553-5558, Oct. 2017.

3. **S.-L. Chen**, F. Wei, P.-Y. Qin, Y. J. Guo, and X. Chen, "A Multi-Linear Polarization Reconfigurable Unidirectional Patch Antenna," *IEEE Transactions on Antennas and Propagation*, vol. 65, no. 8, pp. 4299-4304, Oct. 2017.

4. **S.-L. Chen**, D. K. Karmokar, P. Y. Qin, R. W. Ziolkowski, and Y. J. Guo, "Polarization-Reconfigurable Leaky-Wave Antenna with Frequency-Based Continuous Beam Scanning Through Broadside," *IEEE Transactions on Antennas and Propagation*, Minor revision, May 2019.

5. **S.-L. Chen**, D. K. Karmokar, Z. Li, P. Y. Qin, R. W. Ziolkowski, and Y. J. Guo, "Continuous Beam Scanning at a Fixed Frequency with a Composite Right/Left-Handed Leaky-Wave Antenna Operating Over a Wide Frequency Band," *IEEE*

Transactions on Antennas and Propagation, Major revision, Feb. 2019.

6. **S.-L. Chen**, P.-Y. Qin, W. Lin, and Y. J. Guo, "Pattern-Reconfigurable Antenna with Five Switchable Beams in Elevation Plane," *IEEE Antennas and Wireless Propagation Letters*, vol. 17, pp. 454-457, Mar. 2018.

7. **S.-L. Chen**, P.-Y. Qin, Y. J. Guo, Y. Liu, and P. You, "Generalized 2-D Numerical Pattern Synthesis Algorithm for Low Cross Polarization and Low Sidelobe Synthesis," *IEEE Antennas and Wireless Propagation Letters*, vol. 16, pp. 2578-2581, Aug. 2017.

8. W. Lin, **S.-L. Chen**, R. W. Ziolkowski, and Y. J. Guo, "Reconfigurable, Wideband, Low-Profile, Circularly Polarized Antenna and Array Enabled by an Artificial Magnetic Conductor Ground," *IEEE Transactions on Antennas and Propagation*, vol. 66, no. 3, pp. 1564-1569, Mar. 2018.

9. Z. Li, Y. J. Guo, **S.-L. Chen**, and J. Wang, "A Period-Reconfigurable Leaky-Wave Antenna with Fixed-Frequency and Wide-Angle Beam Scanning," *IEEE Transactions on Antennas and Propagation*, vol. 67, no. 6, pp. 3720-3732, Mar. 2019.

10. D. K. Karmokar, Y. J. Guo, P. Y. Qin, **S.-L. Chen**, and T. S. Bird, "Substrate Integrated Waveguide-Based Periodic Backward-to-Forward Scanning Leaky-Wave Antenna with Low Cross-Polarization," *IEEE Transactions on Antennas and Propagation*, vol. 66, no. 8, pp. 3846-3856, Aug. 2018.

11. D. K. Karmokar, Y. J. Guo, **S.-L. Chen**, and T. S. Bird, "Composite Right/Left-Handed Leaky-Wave Antennas for Wide-Angle Beam Scanning with Flexibly Chosen Frequency Range," *IEEE Transactions on Antennas and Propagation*, Minor revision, May 2019.

12. D. K. Karmokar, **S.-L. Chen**, T. S. Bird, and Y. J. Guo, "Single-Layer Multi-Via Loaded CRLH Leaky-Wave Antennas for Wide-Angle Beam Scanning with Consistent Gain," *IEEE Antennas and Wireless Propagation Letters*, vol. 18, no. 2, pp. 313-317, Feb. 2019.

13. P.-Y. Qin, L.-Y. Ji, **S.-L. Chen**, and Y. J. Guo, "Dual-Polarized Wideband Fabry–Perot Antenna With Quad-Layer Partially Reflective Surface," *IEEE Antennas and Wireless Propagation Letters*, vol. 17, no. 4, pp. 551-554, Apr. 2018.

14. Y. J. Guo, P.-Y. Qin, **S.-L. Chen**, W. Lin, and R. W. Ziolkowski, "Advances in Reconfigurable Antenna Systems Facilitated by Innovative Technologies," *IEEE Access*, vol. 6, pp. 5780-5794, Jan. 2018.

15. P. You, Y. Liu, **S.-L. Chen**, K. D. Xu, W. Li, and Q. H. Liu, "Synthesis of Unequally Spaced Linear Antenna Arrays with Minimum Element Spacing Constraint by Alternating Convex Optimization," *IEEE Antennas and Wireless Propagation Letters*, vol. 16, pp. 3126-3130, Oct. 2017.

Conference Papers

16. **S.-L. Chen**, W. Lin, P.-Y. Qin, Y. J. Guo, and R. W. Ziolkowski, "A Novel Low-Profile Wideband Reconfigurable CP Antenna Array," *12th European Conference on Antennas and Propagation (EuCAP 2018)*, pp. 1-5, Apr. 2018.

17. P.-Y. Qin, **S.-L. Chen**, and Y. J. Guo, "A Compound Reconfigurable Microstrip Antenna with Agile Polarizations and Steerable Beams," *Antennas and Propagation (ISAP), 2017 International Symposium on*, pp. 1-2, Oct. 2017. (***Finalist Award***).

18. **S.-L. Chen**, P.-Y. Qin, and Y. J. Guo, "Multi-Linear Polarization Reconfigurable Center-Fed Circular Patch Antenna with Shorting Posts," *APS/URSI, 2017 IEEE*

International Symposium on, pp. 2209-2210, Jul. 2017. (***Honorable Mention Award***).

19. **S.-L. Chen**, P.-Y. Qin, Y. J. Guo, Y. Liu, and P. You, "Array Pattern Synthesis Using Numerical Pattern Synthesis Algorithm Including Mutual Coupling," *APS/URSI, 2017 IEEE International Symposium on*, pp. 2295-2296, Jul. 2017.

Chapter 2

Background and State-of-the-Art

This chapter basically introduces resonant and non-resonant antennas. As one of the simplest resonant antennas, dipole antenna is taken as an example to explain the operating mechanism of the resonant antennas. As an important and most widely used non-resonant antenna, leaky-wave antenna has been reviewed. Several challenging aspects of both the reconfigurable resonant and leaky-wave antennas are highlighted. Corresponding their relevance to the work described in this thesis, the detailed state-of-the-art is reviewed.

2.1 Resonant Antennas

2.1.1 Basic Characteristics

Resonant antennas have standing waves of total current on the antenna conductors. Typical resonant antennas are dipoles, microstrip antennas, and loop antennas. To explore the operating mechanism of the resonant antennas, the dipole antenna will be considered.

2.1.2 Dipole Antenna

The dipole antenna is one of the simplest resonant antennas. The most widely used dipole antenna is the half-wavelength dipole. The configuration of the half-wavelength dipole antenna is shown in Fig. 2.1. It consists of two symmetrical straight wires located along z-axis, and each wire has a length of L ($L = \lambda/4$). It is fed at the center with a source.

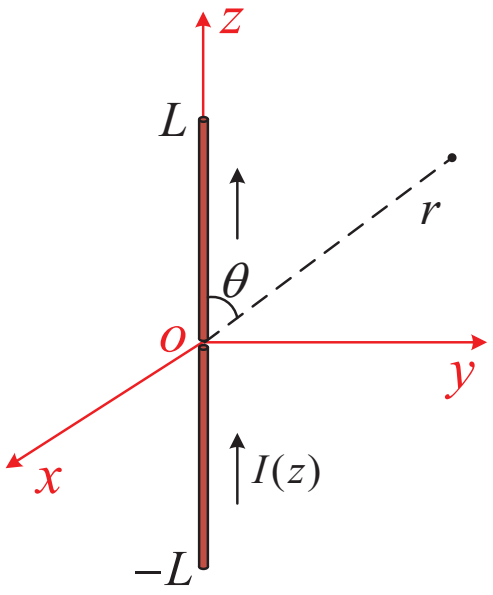

Figure 2.1: Configuration of the half-wavelength dipole antenna.

Take the origin of the coordinates at the center of the dipole, the current distribution on the half-wavelength dipole can be approximately expressed as:

$$I(z) = I_m \sin[k_0(L - |z|)], \quad -L \leq z \leq L \tag{2.1}$$

where I_m is the current at the feed point of the antenna, k_0 is the propagation constant in air. At a far-field region r ($r \gg L$), the magnetic vector potential is calculated as [7]:

$$A_z = \frac{I_m e^{-jk_0 r}}{4\pi r} \int_{-L}^{L} \sin[k_0(L - |z'|)] e^{jk_0 z' \cos\theta} dz' = \frac{I_m e^{-jk_0 r}}{2\pi r} \frac{\cos(\frac{\pi}{2}\cos\theta)}{k_0 \sin^2\theta} \tag{2.2}$$

where θ is the elevation angle measured from the broadside. Consequently, the far-field electric field and magnetic field responses are:

$$E_\theta = j\omega\mu_0 \sin\theta A_z = \frac{j\eta_0 I_m e^{-jk_0 r}}{2\pi r} \frac{\cos(\frac{\pi}{2}\cos\theta)}{\sin\theta} \tag{2.3}$$

$$H_\phi = \frac{E_\theta}{\eta_0} = \frac{jI_m e^{-jk_0 r}}{2\pi r} \frac{\cos(\frac{\pi}{2}\cos\theta)}{\sin\theta} \tag{2.4}$$

where μ_0 and η_0 are the permeability and wave impedance in air, respectively. It is concluded from the above field responses that the radiation patterns of the half-wavelength dipole are an 8-shaped pattern in ZX plane and an omnidirectional pattern in XY plane.

2.2 Non-Resonant Antennas

2.2.1 Basic Characteristics

Non-resonant antennas are those have the traveling wave patterns of the current. In general, they have progressive phase patterns associated with this current. Non-resonant antennas can be divided into two main categories: surface wave antennas and leaky-wave antennas (LWAs). LWAs are one of the most widely used types of non-resonant antennas, and are an important research topic in this dissertation. An investigation on the LWAs is carried out below.

2.2.2 Leaky-Wave Antenna

In general, an LWA is a wave-guiding structure that leaks and radiates power as a traveling wave propagates across open regions along its aperture. An LWA has inherent pattern reconfigurability that the main beam directions can be steered by varying their source frequencies [8, 9]. The pointing angle, $\theta(f)$, of the main beam radiated by a conventional frequency-based LWA at its source frequency f is determined by the relation: [10, 11]:

$$\theta(f) = \sin^{-1}[\beta(f)/k_0(f)] \tag{2.5}$$

where $\theta(f)$ is the pointing angle measured from broadside direction, and $\beta(f)$ is the phase constant within the guiding structure. Due to the dependency of $\beta(f)$ and $k_0(f)$ on the source frequency, one can sweep the frequency to scan the main beam angle $\theta(f)$. Generally, LWAs can bring significant benefits including a simple feed network, wide-angle beam scanning, a low profile and cost effectiveness [12–18]. These LWA features are critical since they reduce the cost and complexity of the antenna systems developed for many aircraft, missile, and satellite applications.

Depending on the geometry and operating principles, LWA can be classified into two main categories, i.e., uniform LWA and periodic LWA. A uniform LWA has uniform or quasi-uniform structure, and its period length is usually much smaller than the wavelength. Examples of the uniform LWA are SIW-based long slot LWA [13] and half-width microstrip LWA [19]. Whilst, periodic LWA uses a periodic guiding structure and the period length is generally comparable to the wavelength. Typical examples of the periodic LWA are partially reflective wall LWA [14] and the periodic slot-loaded SIW LWA as shown in Fig. 2.2 reported in [20].

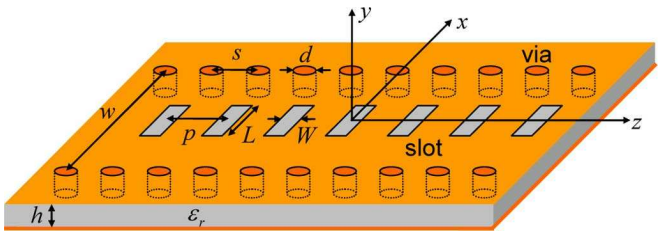

Figure 2.2: Configuration of the periodic slot-loaded SIW LWA reported in [20]. This is an example of the periodic LWA.

2.3 State-of-the-Art

Several challenging yet valuable research foci on both the reconfigurable resonant and leaky-wave antennas are considered. State-of-the-art on each research focus is thoroughly reviewed and stated in the following.

2.3.1 Multi-Linear Polarization-Reconfigurable Resonant Antenna

Polarization reconfigurable antennas have gained increasing attention due to their capabilities to improve the performance of communications systems such as increasing system's diversity and capacity [21–23].

By controlling the ON/OFF states of PIN diodes, many antennas have been developed to achieve polarization switching between linear-polarization (LP), right-handed circular polarization (RHCP), and left-handed circular polarization (LHCP) [24–38]. In [25], two meandered monopoles with a reconfigurable $-90°$ or $90°$ phase difference feed network are presented to realize two circular polarizations, while in [27] two linear polarizations are obtained by switching between the coplanar waveguide mode and slot-line mode. Although LP and CP modes are difficult to match simultaneously, it is possible to switch between LP and CP by reconfiguring the arm length of the U-slot patch antenna [28]. Furthermore, polarization switching between LP, RHCP and LHCP is realized by using a reconfigurable planar metasurface [26], annular slot antennas [32], or printed monopole antennas [33]. Full polarization reconfigurable antennas that can provide two orthogonal LPs and two orthogonal CPs in one topology are described in [34], [35].

Although there has been substantial research effort on polarization reconfigurable antennas, previous work has mainly focused on the reconfigurability between two CPs, between two orthogonal LPs, or among LPs and CPs. Very few antennas have been reported that can switch among multiple linear polarizations with an angle between two adjacent

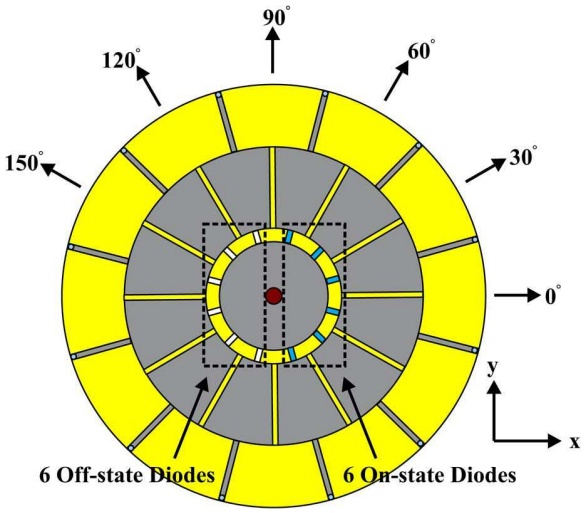

Figure 2.3: Top view of the six-linear polarization switching patch antenna reported in [36].

ones. Multi-linear polarization reconfigurability has some unique advantages. First, it can be employed to reduce multi-path fading losses in indoor wireless communications for applications such as bio-medical systems [37]. Second, for conformal arrays mounted on moving vehicles, antenna elements with multi-linear polarization reconfigurability can lead to higher gains by employing polarization rotation techniques [38]. In order to realize multi-linear reconfiguration, some interesting reconfigurable antennas have been reported.

A six-linear polarization switching patch antenna was developed in [36]. Top view of the antenna configuration is shown in Fig. 2.3. Twelve diodes are utilized to reconfigure the connection between an inner center-fed circular patch and twelve outer metal pieces. One needs to switch six diodes with ON state simultaneously for one specific polarization state. Hence, it uses a complex DC feed network to achieve these six polarization states, and the realized gains are only from 2.6 to 3.5 dBi.

In [37], a circular patch antenna with four bow-tie shaped slots was presented, and its configuration is shown in Fig. 2.4. It can achieve four linear polarizations at a 45° rotation by reconfiguring the slot radiators. The overlapped $|S_{11}| \leq -10$ dB fractional

bandwidth is 16% (2.25 to 2.65 GHz) with a maximum realized gain 6.7 dBi. However, the dimensions of the antenna are relatively large, i.e., $1.22\lambda \times 1.22\lambda \times 0.26\lambda$, which makes it hard to use in arrays.

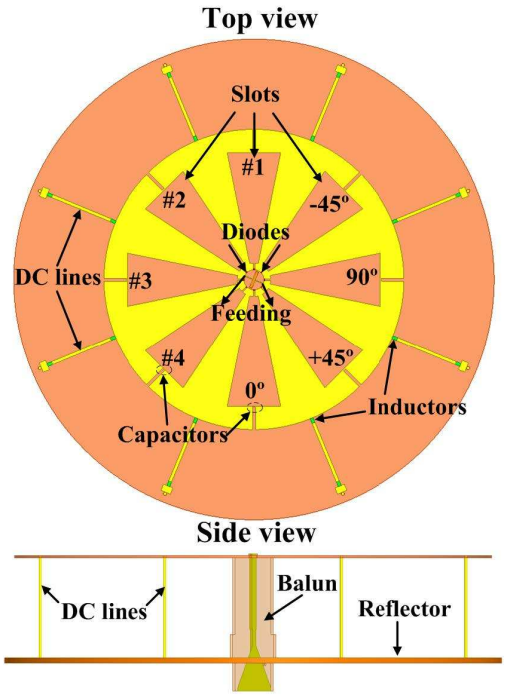

Figure 2.4: Configuration of the circular patch antenna with four bow-tie shaped slots reported in [37].

It is found that it remains difficult to realize a multi-linear polarization reconfigurable resonant antenna using a simple compact configuration.

2.3.2 Pattern-Reconfigurable Resonant Antenna with Switchable Beams

Over the past decade, pattern-reconfigurable antennas have been a topic of considerable research due to their capabilities of enhancing the performance of wireless communication systems [39], [40].

Basically, the research can be classified into three main categories by radiation patterns. The first one involves reconfiguring the main beam shape [41–44], for example by changing the patterns from conical to broadside, which can be exploited to increase the system capacity and/or link quality in MIMO systems. The second one is to change pattern null positions [45], [46], which can alleviate the interference in the radio environment. The third one is to scan the main beam in a certain angle range. The beam scanning ability can be employed to either improve signal-to-noise ratio by directing the signal toward intended users or provide larger coverage. A few novel designs have been developed that can scan the beam $\pm\alpha^{\circ}$ with respect to the broadside direction (α is usually less than 50) [47–49].

For many practical applications, a larger scanning range including endfire and broadside directions is desirable. For example, in order to increase the range of the communication link for unmanned aerial vehicle (UAV) as shown in Fig. 2.5, when UAV flies from far away to the top of the ground control station, end-fire, titled, and broadside beams in the elevation plane are needed for different positions.

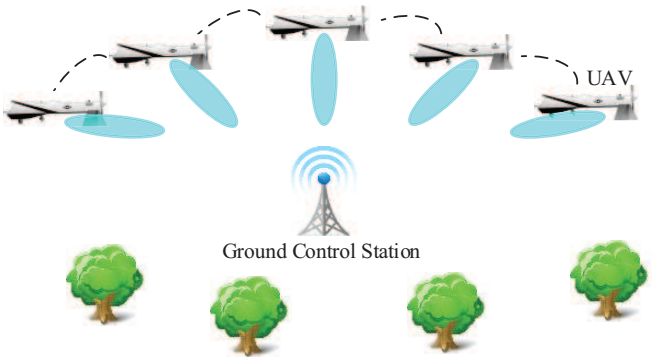

Figure 2.5: A schematic of unmanned aerial vehicle (UAV) communications.

A number of pattern-reconfigurable antennas have been reported to achieve this beam agility to some extent. In [50], by loading a high impedance surface under a closely spaced microstrip parasitic array, two symmetrical endfire patterns are reconfigured. In

[51], a reconfigurable broadside radiation pattern and two endfire radiation patterns in the elevation plane are achieved by placing parasitic strips around a driven monopole. Instead of using the parasitic strips, H-shaped resonator structures are developed to switch the main beam between broadside and endfire directions [52]. In [53], by employing varactor diode loaded parasitic elements, two endfire beams are realized with high front-to-back ratio. It is found that this configuration can achieve no more than three reconfigurable beams in the elevation plane including the broadside and endfire directions.

In [54], as shown in Fig. 2.6, an SIW etched with four slots and loaded with a perpendicular metal reflecting plane is used to achieve the pattern reconfiguration. By switching the four PIN diodes soldered across the slots, the main beam can be reconfigured between six discrete directions. However, the beam cannot be steered to the broadside direction, which is usually essential for wireless communications.

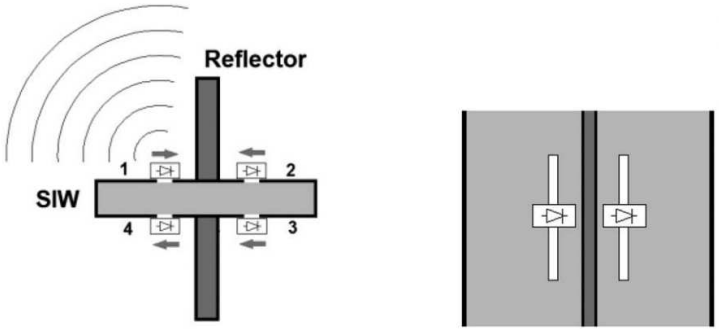

Figure 2.6: Antenna configuration loaded with PIN diodes reported in [54]. Left: transverse plane of waveguide with only vertical reflector and slot 1 radiating. Right: longitudinal plane of waveguide with only slots, diodes and reflector.

It remains a challenge to achieve the beam switching among endfire, titled, and broadside directions with a single compact antenna configuration.

2.3.3 Combined Polarization- and Pattern-Reconfigurable Resonant Antenna

Typical reconfigurable parameters of an antenna are frequency, polarization, radiation pattern, or a combination of the above [21,27,29,31,55–57]. For combined two-characteristic RAs, frequency-polarization, frequency-pattern, and polarization-pattern RAs have been realized [30,43,58]. Moreover, a three-characteristic reconfigurable antenna was achieved using a reconfigurable parasitic pixel surface [59]. Compared to single-parameter reconfigurable antennas, combined ones have the capacity to deliver more flexibility and diversity, which can bring significant benefits to many wireless communication systems [60,61]. As a scenario in conformal antenna arrays, as seen in Fig. 2.7, the antenna elements in the conformal array have different orientations due to the curved conformal surface and, hence, variations of the element pattern and polarization are observed. Reconfigurable antenna element that can simultaneously adjust their radiation patterns and polarizations would eliminate this orientation issue and significantly improve the overall array performance.

For this purpose, some innovative combined polarization and pattern reconfigurable antennas have been reported [62–65]. In [62], a combined RA was developed that can switch its operating modes between a monopole mode and a fundamental patch mode. By exciting the monopole mode, a conical pattern with a vertical polarization was obtained. For the patch mode, the antenna can achieve broadside patterns with dual orthogonal horizontal polarizations. In [63], a reconfigurable microstrip antenna was presented that can switch between a monopole mode with a vertical-linear-polarized conical pattern and a patch mode with a horizontal-circular-polarized broadside pattern. In [64], by switching between two orthogonal truncated monopoles, two orthogonal linear polarizations with omnidirectional patterns in different planes can be reconfigured. It should be noted that in the above reported designs, the pattern and the polarization cannot

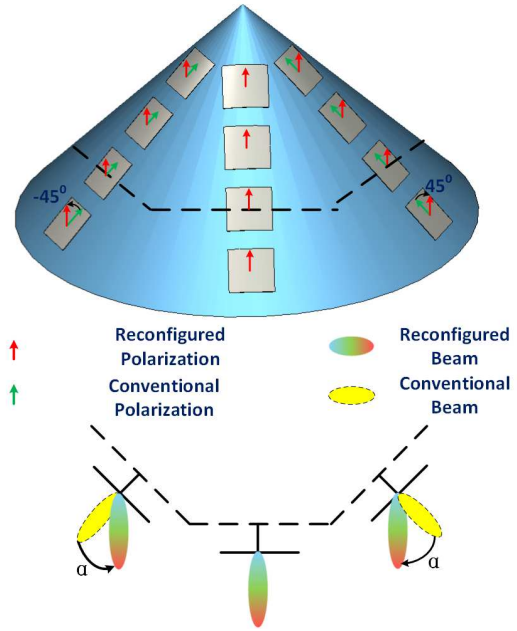

Figure 2.7: Reconfigurable conformal antenna array.

be independently reconfigured. In other words, the polarization/pattern changes with the pattern/polarization. This significantly limits the diversity provided by the combined RAs. Furthermore, the reported designs can only achieve pattern reconfiguration between different pattern shapes, e.g. the switch between broadside and conical patterns, rather than steering the main beam within a certain angle range. However, as beamforming technology is widely adopted in many future wireless systems, such as 5G systems, it is highly desirable that combined reconfigurable antennas are equipped with both the polarization agility and the beam scanning capability. To date, only a few reported designs can overcome the challenge, that is to achieve a beam scanning function with independent polarization reconfiguration in a compact antenna structure.

A good solution has been provided in [65], and the antenna prototype is shown in Fig. 2.8. It utilizes microstrip patch antenna as the main radiator, and reconfigures loaded parasitic dipoles to realize the beam steering. The final antenna system can change between two orthogonal linear polarizations and one diagonal linear polarization. For each

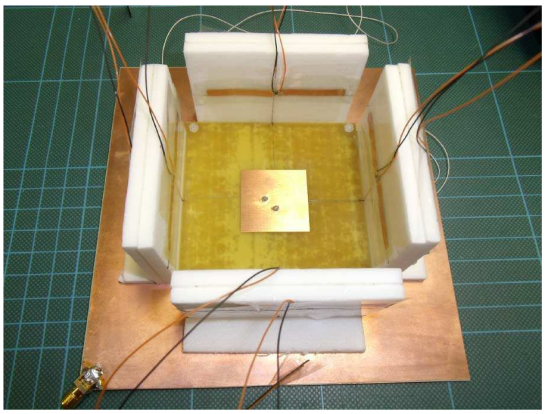

Figure 2.8: Prototype of the combined polarization and pattern reconfigurable reported in [65].

polarization, the main beam can be steered among $-45°$, $45°$, and a dual-direction beam with realized gains of 2.5-3.5 dBi at 2.45 GHz. For the antenna presented in [65], the parasitic elements and the radiating patch are printed in a vertical plane and a horizontal plane, respectively. The antenna beam cannot be steered to broadside. As mentioned, a broadside radiation is usually needed in wireless communication systems.

As indicated in the above discussion, it is quite difficult to realize the simultaneous polarization agility and beam scanning capability with stable radiation performance.

2.3.4 Frequency-Based Pattern-Reconfigurable Circularly Polarized Leaky-Wave Antenna

Leaky-wave antennas (LWAs) are highly promising candidates for future wireless systems based on emerging platforms such as drones and small satellites, where low-cost and low-profile antennas are required. It is known that for applications to radar and satellite systems, it is preferable to radiate a circular-polarization (CP) wave rather than a linear-polarization (LP) one, i.e., the CP LWAs are highly desirable for avoiding polarization mismatch and suppressing multi-path interference during beam scanning [29, 66, 67].

Some challenges exist in achieving frequency-dependent, continuous beam scanning from a CP LWA. First, as mentioned, in order for it to scan the main beam from the backward to the forward direction, a CP LWA must facilitate both positive and negative phase constants. Second, the radiated fields must have two perpendicular components with the same amplitude and a 90° phase difference to be CP waves. This feature must be maintained within the main beam direction as the frequency changes. Moreover, it is known that most periodic LWAs suffer from the open stopband (OSB) problem, i.e., when their beam points at the broadside direction, their realized gain drops significantly [68–70]. Furthermore, there are linkages between suppressing the OSB and the consequent CP performance [71]. On the other hand, even if one does suppress the OSB, it remains a challenge to maintain a consistent gain performance over the entire beam scanning range. Thus, a high performance CP LWA must also have solutions for all of these issues.

A planar-modulated surface-based CP LWA has been reported that suppresses the OSB. However, it is unable to scan its main beam [72]. There are some other interesting approaches that also accomplish continuous CP beam scanning through broadside. One technique is to introduce composite right/left-handed (CRLH) unit cells that satisfy their balanced condition. The OSB is suppressed, and the main beam can be scanned in its fundamental mode [73–75]. Moreover, by introducing a substrate-integrated-waveguide (SIW) or a microstrip line structure into these CRLH-based LWAs, continuous backward to forward CP beam scanning can be obtained [76–78]. In a recent work [78], CP beam scanning in a wide angle from $-19°$ to $+84°$ was obtained. However, the gain variation is large, between 1.0 and 8.95 dBic, within that scan range. Another technique is to use axial-asymmetrical microstrip lines [71, 77]. These series-fed microstrip LWAs introduce an asymmetry in the transversal axis to radiate and scan the CP beam as the source frequency is varied. Nevertheless, it is still very challenging to simultaneously achieve good axial ratio (AR) values and a suppressed OSB over a wide angle scan range.

A third technique is to employ spoof surface plasmon polaritons (SSPPs) [79, 80]. Circular patches located above a slow-wave SSPP line were reported in [79] to generate the CP wave, and the main beam was continuously scanned from $-32°$ to $+34°$ with gain variations between 12.8−14.2 dBic. Yet another popular approach is to use a periodic slot-loaded aperture in a SIW structure. These SIW LWAs have been widely investigated and used due to their easy integration and low loss [20, 81]. An H-shaped slot-loaded SIW reported in [82] realized beam scanning in the forward quadrant from $+20°$ to $+50°$ when the source frequency varied between 10.6 and 11.5 GHz. In a recent work in [83], a periodic SIW CP LWA etched with transverse slot pairs and longitudinal slots was reported as shown in Fig. 2.9. It can successfully realized continuous CP beam scanning from $-40°$ to $+25°$ through broadside by manipulating the etched slots on the SIW. Again, the realized gain had a large variation between 4.2 to 11 dBic within the scanning range.

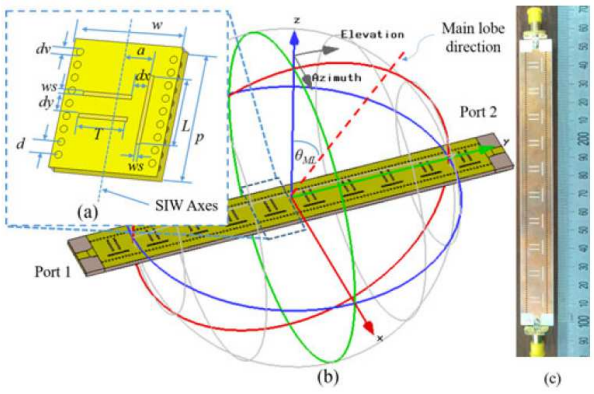

Figure 2.9: Configuration of slot-loaded periodic SIW CP LWA reported in [83]. (a) Unit cell. (b) Complete LWA. (c) Prototype.

As all of these examples illustrate, it is a very challenging problem to achieve a wide-angle continuous CP beam scan with consistent gain performance.

2.3.5 Frequency-Based Pattern-Reconfigurable Leaky-Wave Antenna with Polarization Flexibility

As mentioned in the previous section, LWAs have inherent frequency-based pattern-reconfigurable capability, i.e., they can scan the main beam by varying the source frequency. Various LWA frequency-based beam scanning properties have been reported. When the fundamental mode of a periodic leaky-wave structure is excited, the main beam can be scanned only in the forward quadrant by varying the frequency. Examples include a periodic half-mode microstrip-line LWA [14] and a transverse-slot loaded substrate integrated waveguide (SIW) [20]. On the other hand, when the $n = -1$ spatial harmonic of an one-dimensional (1-D) periodic LWA is excited, backward-to-forward beam steering can be realized [69, 70, 84]. Unfortunately, because they have an inherent stopband, these periodic LWAs cannot steer their main beam through broadside without significant gain loss. This Bragg resonance effect emerges from the coherent reflections arising from each periodic section which suppress the broadside radiation, as well as impair good impedance matching.

A variety of techniques have been developed to suppress the open stopband associated with LWAs. One can close the stopband in 1-D periodic structures simply by introducing additional radiating elements [81] or utilizing impedance matching techniques within their unit cells [85], [86]. One can also elect to employ composite right/left-handed (CRLH) transmission line-based designs [68, 73–75, 87–89]. These CRLH-based LWAs provide a solution for frequency-based continuous backward-to-forward beam scanning. They radiate in the fundamental mode and provide a continuous transition between the backward and forward leaky modes if their balanced condition is satisfied. Recently, backward, broadside, and forward beam scanning has also been obtained using other structures, e.g., groundless spoof plasmon (SP) LWAs [90] and dielectric image line-based LWAs [91].

Note that all of the aforementioned antennas are linearly polarized. Although continuous CP beam steering through broadside has been reported [79], [83], scanning-capable, polarization-reconfigurable antennas have not. While these multi-functionalities would enhance system capacity and avoid polarization mismatch [28, 29, 31, 92–94], it is nevertheless rather challenging to attain polarization reconfiguration in an LWA structure, especially when its main radiator and ground plane are inherently connected with numbers of shorting vias. This is particularly true if PIN diodes are used for the switches since their polarities are difficult to isolate and bias. On the other hand, switching between CP and LP is useful for various electromagnetic environments such as the ones in an RFID system, but it is difficult to realize this reconfigurability using a single antenna configuration [28, 95].

To date, very few 1-D LWAs have been reported to target this issue. In [96], an LWA was reported in which its unit cell is constructed with two microstip lines and two CRLH sections. Choosing the current path along one microstrip line and one CRLH section facilitates exciting one linear polarization (LP) state. The other is produced when the other microstrip line and CRLH section pair is selected. As reported in [97], two CRLH lines were located symmetrically to radiate the orthogonal $\pm 45^{\circ}$ LP states, as shown in Fig. 2.10. Both LP and CP states were then attained by introducing two different feed networks to separately excite the two CRLH lines with the appropriate amplitudes and phase differences.

It is noted that, the above LWA systems achieve the polarization reconfiguration using two independent configurations rather than one augmented with switching devices having realizable biasing circuits. The latter reconfigurable system is preferred to keep simple-feed LWA with low-profile and easy-integration properties.

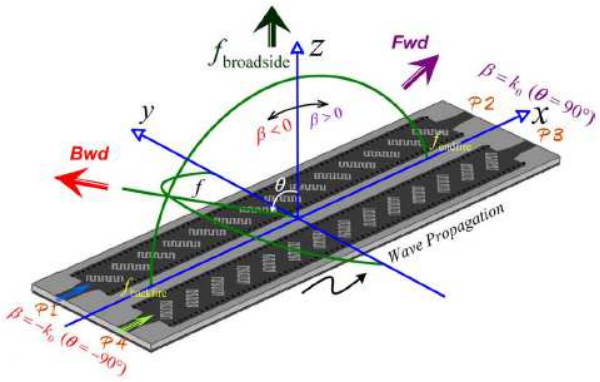

Figure 2.10: Configuration of polarization flexible SIW-based CRLH LWA reported in [97].

2.3.6 Fixed-Frequency Pattern-Reconfigurable Leaky-Wave Antenna

It is recognized that the beam scanning capability of most current LWAs is frequency-based rather than occurring at a fixed-frequency. Only a few fixed-frequency beam scanning LWAs have been realized. Prototypes have used microstrip, Fabry-Perot, and active metasurface structures [98–101]. However, these systems can only scan the beam in a quadrant (left or right quadrant) rather than across the full hemisphere from backward to forward through broadside. Many wireless communication systems prefer to transmit/receive data at a specific, operating frequency within an allocated band, as well as to have continuous beam scanning at all frequencies within it [102]. Nonetheless, it is difficult to achieve this valuable fixed-frequency continuous backward to forward beam scanning through broadside.

To the best of the authors' knowledge, only a few interesting solutions have been reported [103–108]. Continuous beam scanning from $-25°$ to $+25°$ was obtained in [103] by centrally feeding two independently controlled high impedance surfaces of a Fabry-Perot LWA. A 45° beam scan at a fixed operating frequency between 5.5 and 5.8 GHz

was achieved in [104] by using a modulated corrugated microstrip line. As shown in Fig. 2.11, a microstrip line LWA with a reconfigurable 2-bit phase unit was developed in [105] that radiates five switchable beams at 5.0 GHz and five prototypes were fabricated to validate these five working states.

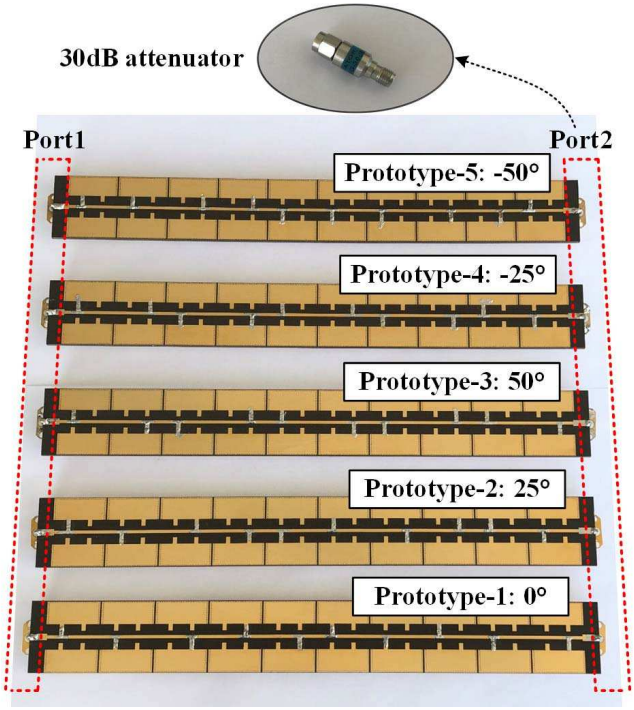

Figure 2.11: Configuration of reconfigurable 2-bit microstrip line LWA reported in [105].

Reconfigurable CRLH structures have realized fixed-frequency beam scanning [106–108]. They can exhibit an inherent continuous transition between their RH and LH dispersion curves when they are designed in their balanced condition. A reconfigurable CRLH LWA that continuously scanned its beam from $-13°$ to $+18°$ was realized in a recent work [108] by tuning the permittivity of a liquid crystal. Nevertheless, these reported fixed-frequency continuous beam scanning LWAs again have a limited scanning range, e.g., less than 60°. Moreover, only a few of them can realize fixed-frequency beam scanning over a band of frequencies and that band is narrow. Furthermore, if one would like to introduce switchable devices to achieve different phase constant states, it is

challenging to isolate the polarities of their DC sources as well as to integrate practical DC biasing lines into their overall structure [105, 107]. These difficulties arise because LWAs with a simple feed structure generally have their radiators connected to a ground plane through a number of shorting vias.

2.4 Summary

Basis on the resonant antennas and non-resonant antennas is given in this chapter. It raises and reviews six challenging yet valuable research foci, i.e., multi-linear polarization-reconfigurable resonant antenna, pattern-reconfigurable resonant antenna with switchable beams, combined polarization- and pattern-reconfigurable resonant antenna, frequency-based pattern-reconfigurable CP LWA, frequency-based pattern-reconfigurable LWA with polarization flexibility, and fixed-frequency pattern-reconfigurable LWA.

It is found that it remains challenging and difficult to realize those functionalities with an effective antenna design. Following chapters will concentrate on solving these limitations along with development of novel antenna systems.

Chapter 3

Multi-Linear Polarization-Reconfigurable Patch Antenna

In the previous chapter, the basis of resonant and non-resonant antennas has been introduced. The state-of-the-art of several research foci on the reconfigurable resonant antennas and leaky-wave antennas has been reviewed. One can recognize that it is challenging yet valuable to realize polarization switching among multi-linear polarization states using a compact configuration. In this chapter, a novel multi-linear polarization-reconfigurable unidirectional circular patch antenna is developed to switch among four linear polarizations (LPs) at every 45° rotation. The patch antenna is fed in the center and shorting posts are used to excite TM_{11} mode with LP. By controlling the connections between the four shorting posts and the ground plane using PIN diodes, four reconfigurable polarization states at $\phi = 0°$, $\phi = 45°$, $\phi = 90°$ or $\phi = 135°$ can be realized. The size of this antenna is about $0.57\lambda\times$

$0.57\lambda \times 0.07\lambda$ at 2.45 GHz. It can be easily fabricated and has a simple biasing network. The measured overlapping impedance bandwidth for different polarizations under the condition $|S_{11}| \leq -10$ dB is from 2.33 GHz to 2.50 GHz, which agrees well with the simulated one. Moreover, the antenna maintains stable radiation patterns and the measured realized gains range from 5.3 dBi to 5.9 dBi.

3.1 Center-Fed Circular Patch Antenna with a Shorting Post

3.1.1 Antenna Configuration

The geometry of the center-fed circular patch antenna with a shorting post is shown in Fig. 3.1. An annular-ring-slot patch is placed on a substrate backed with a thin ground plane. The patch has an outer ring patch with a radius of R, an inner circular patch with a radius of R_r, and a slot width of w_s. The substrate has a relative permittivity of $\varepsilon_r = 2.2$ and a loss tangent of 0.0009 with a thickness of h. The metal printed on the substrate is silver with the electric conductivity of 6.1×10^7 S/m. Both the substrate and the ground plane have the radii of R_g. The feeding pin has a radius of R_{pin}, which is placed at the center of the patch. A shorting post is drilled through the substrate to connect the inner circular patch to the ground plane. It has a radius of r with a distance of d along the x axis from the center.

3.1.2 Cavity Mode Analysis

The above circular patch antenna has a circular patch with a radius of R, a thin substrate with a height of h and a permittivity of ε_r, and a backed ground plane. Since the substrate

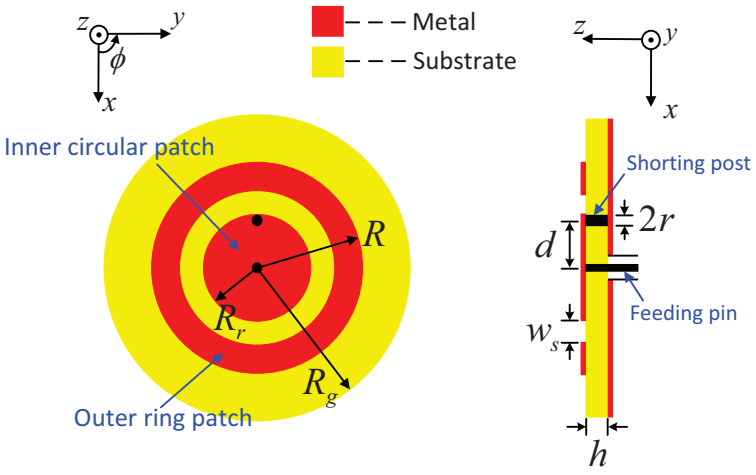

Figure 3.1: Geometry of the center-fed circular patch antenna with a shorting post.

height is very small in terms of the wavelength in the free space, the electric field only has a z component and the magnetic field only has R and ϕ components, where ϕ is defined as an azimuth angle with regards to x axis as shown in Fig. 3.1. Assuming that the surface current normal to the patch edge is close to zero, the circular patch can be equalled to a cylindrical cavity with electric walls on the top and bottom, and magnetic walls on the round edge [109]. Therefore, the fields in the cylinder region can be determined using the corresponding $\mathrm{TM}_{\mathrm{nm}}$ modes, and the resonant frequency can be calculated by:

$$f_{\mathrm{nm}} = \frac{\chi_{\mathrm{nm}} c}{2\pi R_{\mathrm{eff}} \sqrt{\varepsilon_r}} \tag{3.1}$$

where χ_{nm} is a corresponding zero of the derivative of the Bessel function, c is the velocity of light in the air, and R_{eff} is the effective radius considering the fringing effects on the edge, and it can be calculated by [109]:

$$R_{\mathrm{eff}} = R\{1 + \frac{2h}{\pi R \varepsilon_r}(\ln \frac{\pi R}{2h} + 1.7726)\}^{1/2} \tag{3.2}$$

As can be seen, the modes excited in the cylinder region are determined by the value of patch radius R.

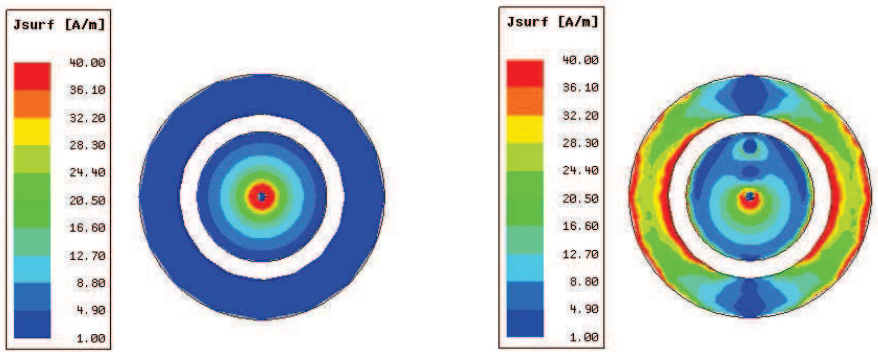

(a) (b)

Figure 3.2: Current distribution of the center-fed circular patch antenna at 2.45 GHz. (a) Without a shorting post. (b) With a shorting post along x axis.

As is known, for the conventional monopole-like center-fed circular patch antenna, its current on the patch is symmetrical along ϕ-direction shown in Fig. 3.2(a). As a result, only TM_{0m} modes can be obtained for the center-fed circular patch antenna [110]. With the added shorting post placed along the x axis in the center-fed circular patch antenna, as can be seen from Fig. 3.2(b), the surface current is concentrated on the inner and outer edges of the outer ring and is changed with a variation along ϕ direction. Thus, the fundamental TM_{11} mode is excited. The ring slot etched on the patch is used for the impedance match. For the fundamental TM_{11} mode of the proposed circular patch antenna, with the zero root χ_{11} equal to 1.84, using the parameters given in Table 3.1, the resonant frequency f_{11} is calculated at about 2.45 GHz.

3.1.3 Parameter Study and Discussions

Table 3.1 provides the antenna parameters and dimensions. To understand the effect of antenna dimensions on the resonant frequency and impedance matching, a parametric study is conducted on the outer patch radius of R, the inner patch radius of R_r, the ring slot width of w_s and the shorting post radius r. When one parameter is changed, the

Table 3.1: Dimensions of the Center-Fed Circular Patch Antenna with a Shorting Post

Parameters	R_g	R	R_r	d	w_s	r	h	R_{pin}
Values (mm)	35	18	9	8	2.5	1	7	0.65

others remain the same as shown in Table 3.1.

Fig. 3.3(a) shows the effect of the outer patch radius R on the antenna input reflection coefficients. As expected, the resonance shifts towards the lower frequency when the outer patch radius R is increased. The operating band of the antenna remains stable with a relative bandwidth of about 4% for $|S_{11}| \leq -10$ dB for different values of R.

Fig. 3.3(b) shows the effect of the inner patch radius R_r on the antenna input reflection coefficients. As can be seen, when the inner patch radius R_r increases, the resonant frequency decreases. This is because the equivalent path length of current flow on the inner edge of the outer ring patch becomes longer. Meanwhile, when the radius R_r equals 7.5 mm and 9 mm, the antenna achieves a good impedance matching with a stable bandwidth. However, when the radius value is greater than 9 mm, the impedance matching becomes worse.

Fig. 3.4(a) shows the effect of the ring slot width w_s on the antenna input reflection coefficients. As can be seen, the resonant frequency decreases when w_s is increased. This is because a greater value of w_s will lead to a longer current path on the inner edge of the outer ring patch, thereby reducing the resonant frequency.

Fig. 3.4(b) shows the effect of the shorting post radius r on the antenna reflection coefficients. When r increases, the resonant frequency moves to the lower band. When $r = 1$ mm, the antenna achieves the best impedance match.

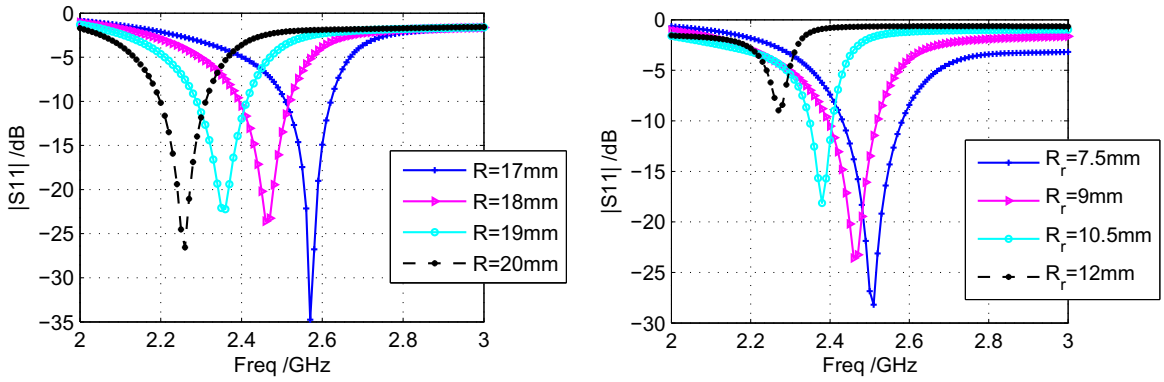

(a) (b)

Figure 3.3: Input reflection coefficients. (a) Varying with the outer patch radius R. (b) Varying with the inner patch radius R_r.

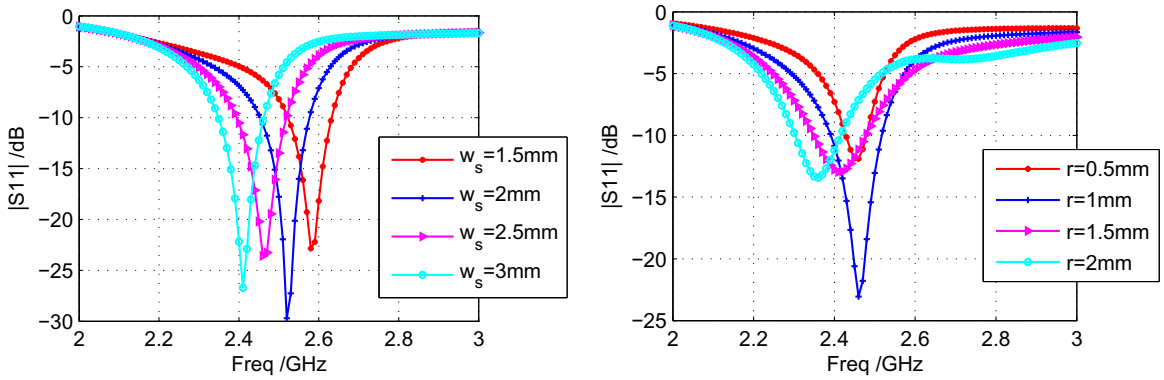

(a) (b)

Figure 3.4: Input reflection coefficients. (a) Varying with the ring slot width w_s. (b) Varying with the shorting post radius r.

3.1.4 Fabrication and Measurement

Based on the above parametric study, a prototype of the developed antenna has been fabricated and measured. Fig. 3.5 shows the simulated and measured input reflection coefficients. As seen from Fig. 3.5, the measured impedance band (2.37 GHz to 2.49 GHz) for $|S_{11}| \leq -10$ dB is well aligned with the simulated one (2.40 GHz to 2.52 GHz).

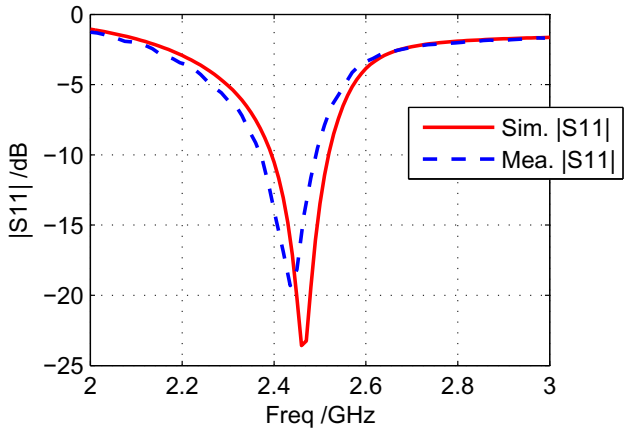

Figure 3.5: Simulated and measured input reflection coefficients of the center-fed circular patch antenna with a shorting post.

According to the configuration in Fig. 3.1, this antenna's polarization is along x axis. Fig. 3.6 shows the simulated and measured radiation patterns at 2.45 GHz in E plane and H plane. The measured realized gain is about 6.3 dBi, which is close to the simulated one of 6.5 dBi. As can be seen, the measured and simulated half-power beamwidths of

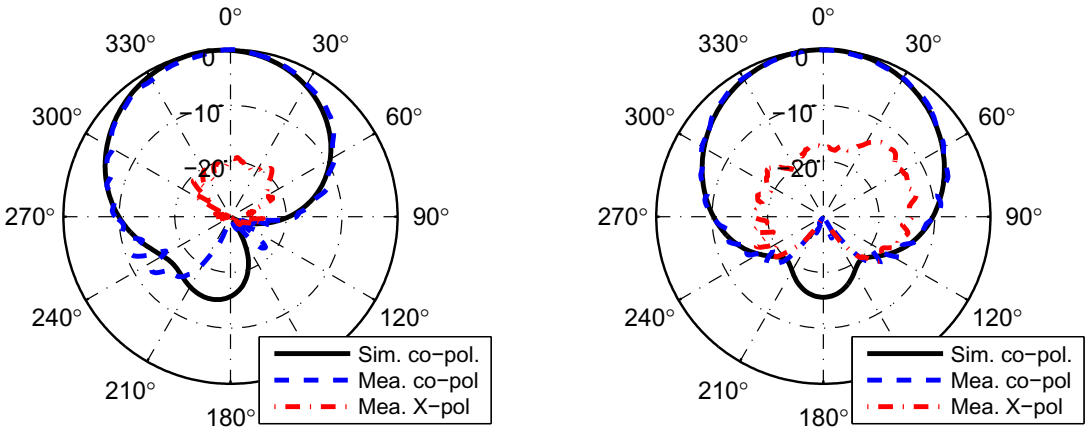

(a) (b)

Figure 3.6: Simulated and measured radiation patterns at 2.45 GHz. (a) E plane. (b) H plane.

the co-polarization pattern are both 81° in E plane, and 88° in H plane, respectively. In addition, the measured cross-polarization levels in both planes are below −13 dB.

3.2 Multi-Linear Polarization Reconfigurable Antenna with Shorting Posts

3.2.1 Antenna Configuration and Analysis

Based on the above study of the center-fed circular patch antenna with a shorting post, different linear polarizations with a specific angle can be obtained by rotating the position of the shorting post with the same radius in the x-y plane. The structure of the developed multi-linear polarization reconfigurable antenna is shown in Fig. 3.7. As can be seen from Fig. 3.7(a), the proposed antenna has an upper substrate, a lower substrate and an air gap between them. These two substrates have a relative permittivity of $\varepsilon_r = 2.2$ and a loss tangent of 0.0009. The heights of the two substrates and the air gap are h_1, h_2, and h_a, respectively. For the upper substrate, a patch layer is etched on the top and the bottom metal is removed. For the lower substrate, a biasing layer is printed on the top and the bottom is the ground plane of the antenna.

As seen in Fig. 3.7(b), on the patch layer, an annular-ring-slot patch is printed. It has an inner circular patch with a radius of R_r and an outer wheel-shaped ring with parameters R_1, R_2, R_3, and R_4. Rather than the regular ring patch shown in Section 3.1, the outer wheel-shaped ring is used to increase the impedance bandwidth by reducing the antenna's Q factor [111]. The center hole is drilled for the feeding pin and the other four holes at a 45° interval with a distance d_A from the center are drilled for inserting the shorting posts. The shorting posts have a radius of r_A and a height of h_A, as shown in Fig. 3.7(a) and (c).

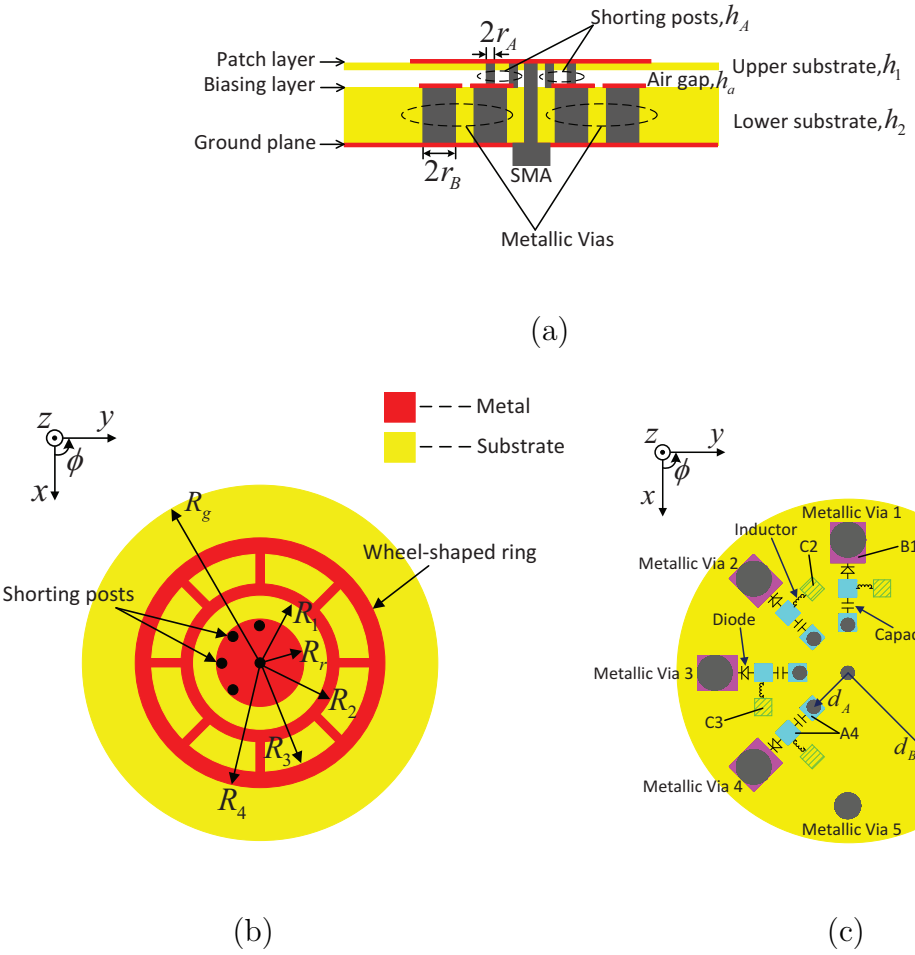

Figure 3.7: Geometry of the multi-linear polarization reconfigurable antenna with shorting posts. (a) $\phi = 67.5°$ side view. (b) Top view of the patch layer. (c) Top view of the biasing layer.

On the biasing layer, the biasing network and three pads groups (A, B and C) are printed as shown in Fig. 3.7(c). The shorting posts inserted through the four holes at the upper substrate are soldered onto the pad group A. Pad group B is connected to the antenna ground plane through the metallic vias (Via 1 to 4) with a radius r_B drilled through the lower substrate. The metallic vias have a distance d_B from the center. Four PIN diodes are soldered between pads group A and group B. For each PIN diode, one polarity is connected to the ground plane and the other is connected to the pad group A. This way, once a particular PIN diode is switched on, the corresponding shorting post attached to the inner circular patch on the patch layer is shorted to the ground. Pad group C is used for applying the DC biasing voltages. The inductors (47 nH) are located between the pads group A and group C, which choke the RF signal while maintaining the DC biasing voltage. It should be noted that thin slots are cut through pad group A and four surface-mount capacitors (27 pF) are placed across them to isolate the RF source from the DC signal while maintaining the RF signal paths. In addition, there are another four metallic vias (Via 5 to 8) with a radius r_C drilled on the lower substrate, which are used for impedance matching purpose only.

For each working state, only one pad of group C is loaded with positive voltage to switch on the specific diode. As a result, the antenna can switch among four polarization states along $\phi = 0°$, $\phi = 45°$, $\phi = 90°$, and $\phi = 135°$. As an example, to obtain $\phi = 90°$ polarization, the pad labeled C3 is connected to the positive output of the power supply, while the other three are grounded. Beam lead PIN diodes DSM8100-000 produced by the Skyworks Company are used. According to the datasheet, the diode is modeled as a resistance of 4 Ω for the ON state and as a parallel circuit with a capacitance of 0.03 pF and a resistance of 20 kΩ for the OFF state at 2.45 GHz.

3.2.2 Fabrication and Measurement

Table 3.2: Dimensions of the Reconfigurable Multi-Polarization Antenna with Shorting Posts.

Parameters	R_g	R_r	R_1	R_2	R_3	R_4	d_A
Values (mm)	35	5.5	8.5	10	17	19	4.4
Parameters	d_B	h_1	h_2	h_A	r_A	r_B	r_C
Values (mm)	11.2	0.508	7	1.3	0.5	1.5	1

The parameters and dimensions of the antenna are shown in Table 3.2. Based on this, an antenna prototype was fabricated as shown in Fig. 3.8. The overall size of the antenna is about $0.57\lambda\times\ 0.57\lambda\times 0.07\lambda$ at 2.45 GHz. A Keithley 2230 SourceMeter power supply is used to provide 10 mA biasing current for the PIN diodes. It should be noted that the input reflection coefficients for 0° and 135° polarizations are slightly different from those for 45° and 90° polarizations due to the structural asymmetry on the biasing layer. The simulated and measured reflection coefficients for 0° and 135° polarizations are shown in Fig. 3.9(a). The simulated -10 dB impedance bandwidth is from 2.38 GHz to 2.56 GHz, while the measured is from 2.33 GHz to 2.56 GHz. The simulated and measured reflection coefficients for 45° and 90° polarizations are shown in Fig. 3.9(b). The simulated -10 dB impedance bandwidth is from 2.36 GHz to 2.51 GHz, while the measured one is from 2.30 GHz to 2.50 GHz. The slight frequency shift can be attributed to the tolerance of the substrate dielectric constant and the inaccuracies in the fabrication process. The measured reflection coefficients for all four polarization states are overlapped from 2.33 GHz to 2.50 GHz.

Fig. 3.10 shows the simulated and measured E-plane and H-plane patterns at 2.45 GHz for $\phi = 0°$ polarization state. It is found from the measurement that for the E-

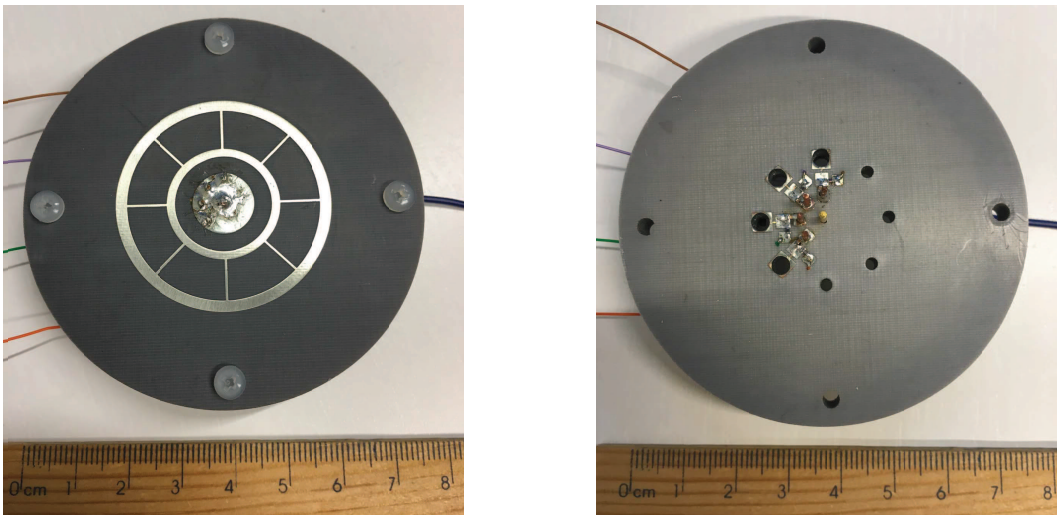

(a) (b)

Figure 3.8: Top view of the multi-linear polarization reconfigurable antenna prototype with shorting posts. (a) Patch layer. (b) Biasing layer.

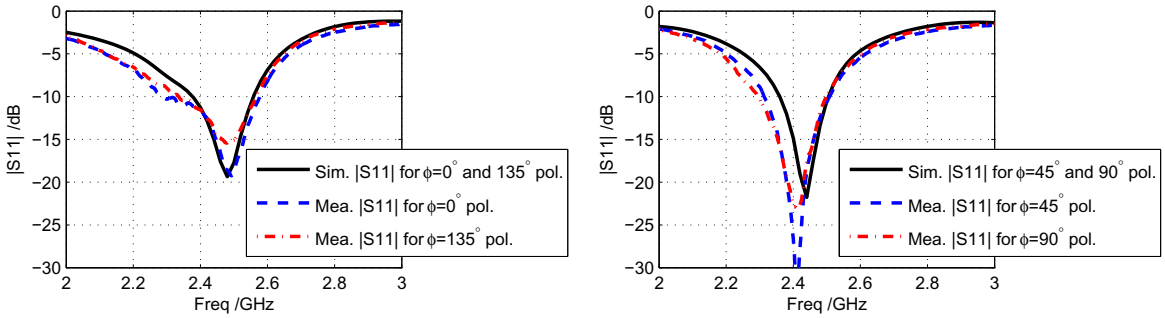

(a) (b)

Figure 3.9: Simulated and measured input reflection coefficients of the multi-linear polarization reconfigurable antenna with shorting posts. (a) $\phi = 0°$ and $\phi = 135°$. (b) $\phi = 45°$ and $\phi = 90°$ polarizations.

plane and H-plane co-polarization patterns of all four polarization states, the measured results agree well with the simulated ones. Besides, the measured and simulated cross-polarization levels are below -10 dB for all polarization states. Table 3.3 shows the comparison of the simulated and measured realized gains at 2.45 GHz. The measured

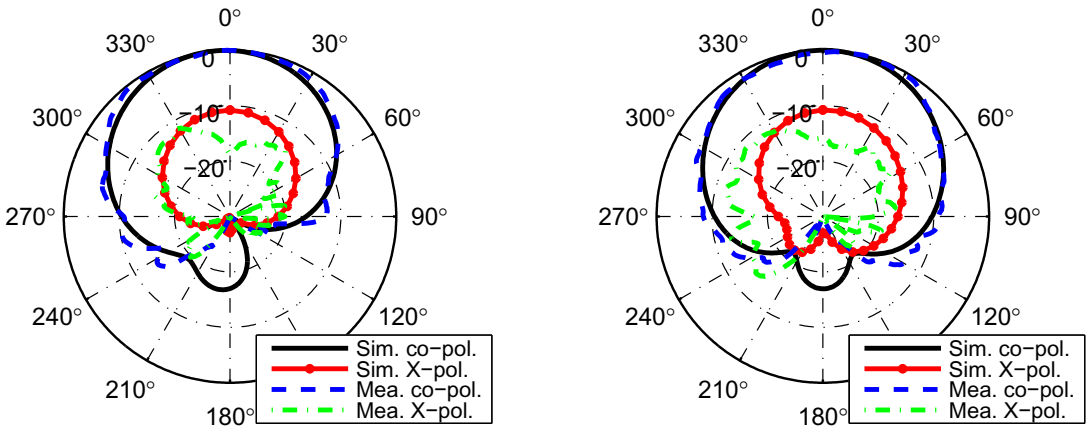

(a) (b)

Figure 3.10: Simulated and measured radiation patterns for $\phi = 0°$ polarization at 2.45 GHz. (a) E plane. (b) H plane.

realized gains are ranging from 5.3 dBi to 5.9 dBi, which agree reasonably well with the simulated 6.2 dBi. For 0° and 135° polarization states, the simulated antenna efficiency is 84.7% at 2.45 GHz, and for 45° and 90° polarization states, the efficiency is 82.9%. The loss of the PIN diode is about 0.5 dB in terms of the gain of the antenna.

Table 3.3: Simulated and Measured Gains for Four Polarization States

Polarization state	$\phi = 0°$	$\phi = 45°$	$\phi = 90°$	$\phi = 135°$
Sim. gain (dB)	6.2	6.2	6.2	6.2
Mea. gain (dB)	5.3	5.4	5.9	5.7

3.3 Conclusion

In this chapter, a center-fed circular patch antenna with shorting posts, which can be reconfigured to switch among four linear polarizations at a 45° rotation, is demonstrated. A non-reconfigurable center-fed circular patch antenna, which can excite the fundamental

TM_{11} mode with a broadside beam, is designed and studied for the first time. Based on the non-reconfigurable antenna, four PIN diodes and multiple shorting posts at a 45° interval are used to achieve the reconfigurable polarizations along $\phi = 0°$, $\phi = 45°$, $\phi = 90°$, and $\phi = 135°$. The measured input reflection coefficients for all these four states overlap from 2.33 GHz to 2.50 GHz, and the gains range from 5.3 dBi to 5.9 dBi. The cross-polarization levels of E and H planes for all operating states are below −10 dB.

Chapter 4

Pattern-Reconfigurable Dipole Antenna with Switchable Beams in the Elevation Plane

In the previous chapter, antennas have been investigated and developed to switch their polarization states. Polarization is an antenna's important characteristic as it can be used to select desired polarized signals. As another important characteristic, radiation pattern can be employed to direct signals towards intended users and, hence, pattern reconfigurable antennas that can alter their radiation patterns are promising for communications with fast-moving users. In this chapter, a novel pattern-reconfigurable antenna is presented that provides an efficient solution for the pattern-reconfigurable antennas with multiple switchable beams. By reconfiguring parasitic striplines placed around a radiating dipole and reflecting metal pieces under the dipole using PIN diodes, the antenna main beam can be switched to five directions in the elevation plane, approximately from $-90°$ (left endfire), $-45°$, $0°$ (broad-

side), +45°, to +90° (right endfire). The developed antenna operates at 2.45 GHz with dimensions of about $0.57\lambda \times 0.45\lambda \times 0.28\lambda$. An antenna prototype was fabricated and measured. For all five directional beams, The measured $|S_{11}|$ values are below -13 dB, and the measured realized gains range from 5.2 to 6.5 dBi. They agree reasonably well with the simulated ones.

4.1 Antenna Design and Analysis

4.1.1 Antenna Configuration

The geometry of the proposed pattern-reconfigurable antenna with different views is shown in Fig. 4.1 (a) and (b). It consists of two horizontally placed substrates, four supporting posts, and a vertically placed feed substrate. These three substrates are Rogers RT/Duroid 5880 laminate ($\varepsilon_r = 2.2$, $\tan\delta = 0.0009$). The dimensions of the two horizontal substrates are $L_s \times W_s \times h_s$. The height of the air gap between these two substrates is h_a. The T-shaped feed substrate is centrally located that is inserted from the lower substrate to reach the upper substrate.

For the upper substrate, the metal of the top is removed and a metal radiating layer is etched on the bottom, as shown in Fig. 4.2. On this radiating layer, there are a radiating dipole with a length L_1 and two identical parasitic strips with a length $L_2 + 2L_3$ placed at a distance d from the center. Four diodes D1-D4 are soldered across small thin slots cut on the two parasitic lines. The radiating dipole and the parasitic lines have a width W. As can be seen in Fig. 4.2, the whole structure of the radiating layer is symmetrical about the lines PP' and QQ'. Note that a rectangular hole is centrally drilled for inserting the feed substrate.

For the lower substrate, as shown in Fig. 4.3, six reflecting rectangular metal pieces are printed on the top, which is named as a reflecting layer, while the metal on the bottom of

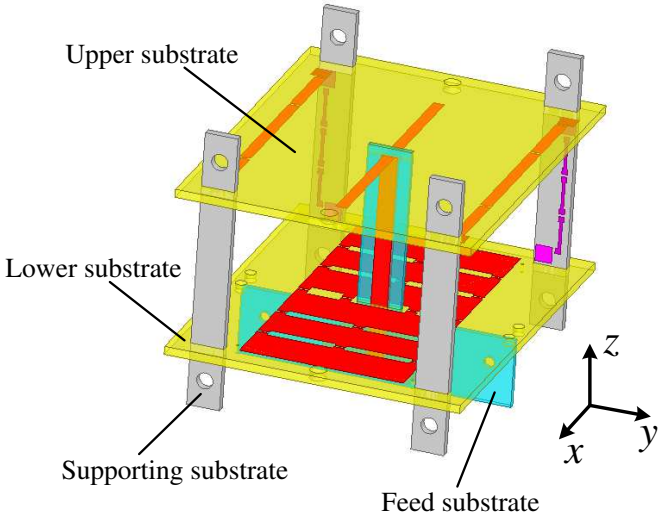

(a)

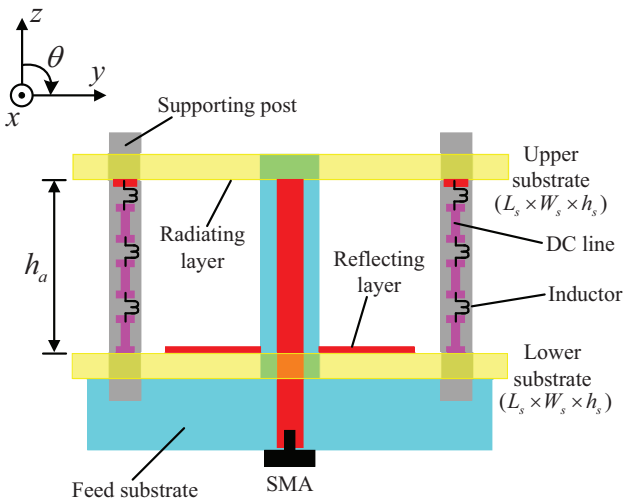

(b)

Figure 4.1: Geometry of the developed pattern reconfigurable antenna. (a) Overall view. (b) Front view.

this substrate is removed. These six metal pieces are connected by 16 PIN diodes D5-D20 with a gap L_d. Four diodes are used between Piece 3 and Piece 4 due to the central hole for the feed substrate to go though, while three diodes are employed for other two

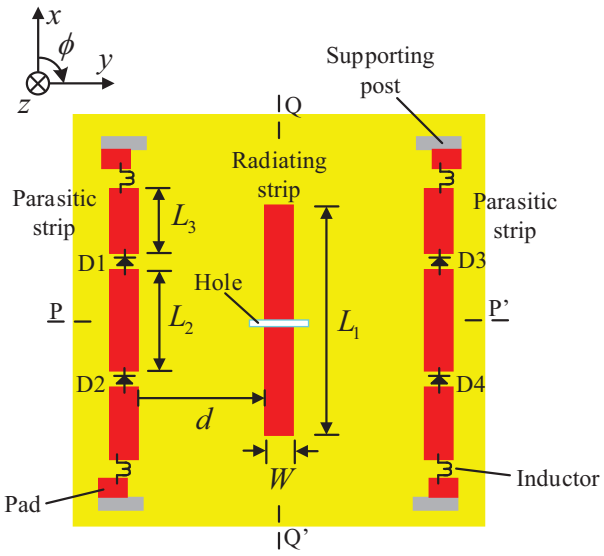

Figure 4.2: Bottom view of the radiating layer.

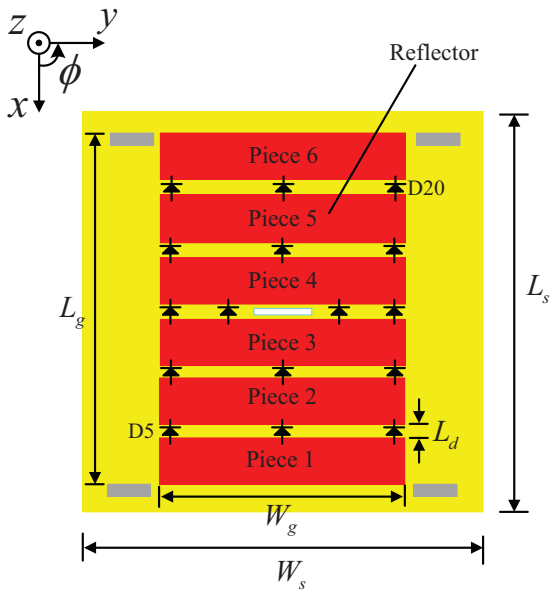

Figure 4.3: Top view of the reflecting layer.

adjacent pieces. All the diodes are oriented in the same direction along x-axis. Thus, all the 16 diodes can be switched ON/OFF simultaneously.

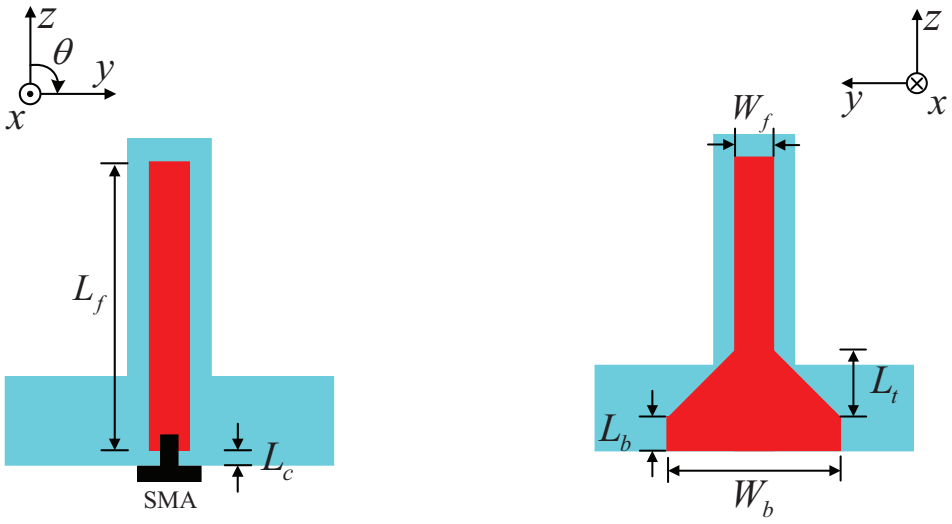

(a) (b)

Figure 4.4: Configuration of the feed substrate. (a) Front view. (b) Back view.

The feed substrate, as seen in Fig. 4.4, has a tapered microstrip line transferred to a coplanar stripline. With this transition, the unbalanced power from the SMA connector can be balanced at the output of the coplanar stripline, which serves as a balun feed for the radiating dipole [112]. The thickness of this feed substrate is 1 mm, and other parameters of the substrate dimensions are indicated in Fig. 4.4.

4.1.2 Pattern Reconfiguration Mechanism

The developed pattern-reconfigurable antenna can steer its main beam in elevation plane (zy plane) to five different elevational angles. As is well known, a half-wavelength dipole antenna with a balun feed can radiate an 8-shaped pattern in the E-plane and an omnidirectional pattern in the H-plane. The main strategy of the beam scanning is to reconfigure both the parasitic striplines around the dipole printed on the upper substrate

and the reflecting metal pieces printed on the lower substrate. As can be seen in Fig. 4.2, two diodes on either parasitic stripline are employed to reconfigure the line length. For example, when D1 and D2 are both switched ON, the length of the left parasitic line is $L_2 + 2L_3$. In this case, the parasitic line can act as the reflector for the radiating dipole. When D1 and D2 are both OFF, the length changes to be L_2. In this case, it serves as a director. The same mechanism applies for the right parasitic line. When the left one is electrically longer than the right one, the main beam will be steered to the right, and vice versa.

For the reflecting metal patches on the lower substrate, when D5-D20 are all switched ON, six pieces of the metal patches are connected with each other, thus acting as a reflector for the dipole. When D5-D20 are all OFF, the pieces are separated from each other and the operating frequency of each piece is far away from the radiating dipole. Therefore, they have little effect on the radiation pattern of the radiating dipole. Moreover, the location and number of these 16 diodes have been carefully studied to achieve good radiation performance of the antenna.

Table 4.1: Five Reconfigurable Working Modes

Working mode	Diode group switched ON	Pattern mode
Mode 1	D5-D20	Broadside
Mode 2	D1-D2 and D5-D20	Right tilted
Mode 3	D1-D2	Right endfire
Mode 4	D3-D4 and D5-D20	Left tilted
Mode 5	D3-D4	Left endfire

Based on the above analysis, five switchable beams can be obtained by switching the

states of 20 diodes D1-D20. The corresponding biasing states of all PIN diodes for each beam are shown in Table 4.1. For Mode 1, only PIN diodes D5-D20 are switched ON. In this case, the two parasitic lines are of the same length and there is a reflector on the lower substrate under the dipole. Therefore, the antenna radiates a broadside beam. For Mode 3, only D1 and D2 are switched ON. In this case, the left parasitic line is longer than the right one and there is no reflector under the radiating dipole, making the main beam in the H-plane be radiated to the right endfire direction ($\theta \approx 90°$). For Mode 2, D1,D2, and D5-D20 are switched ON. Compared to Mode 3, the reflector under the dipole is activated and it has an effect on the main beam direction. Therefore, the main beam is not along the right endfire direction, but steered to a right angle ($\theta \approx 45°$). The tilted angle of Mode 2 is co-determined by the reflection of the reflector on the reflecting layer and the parasitic line on the radiating layer. Specifically, one can optimize the distances of the parasitic lines d and the reflecting layer h_a to the radiating dipole to achieve the requisite phase delay for the desired tilted beam angles. Similarly, a left endfire beam ($\theta \approx -90°$) and a left tilted beam ($\theta \approx -45°$) can also be achieved by switching the diodes, as shown in Table 4.1.

4.1.3 DC Feed Network

As can be seen, D1 and D2 are switched ON and OFF simultaneously. To bias D1 and D2, one DC source is applied through DC lines printed on the left two supporting posts. In order to reduce the effects of DC biasing lines on the antenna radiation performance, the DC lines are broken down into small sections bridged with inductors, as can be seen in Fig. 4.1. To bias D3 and D4 on the right parasitic stripline, similar DC feed network is designed. Furthermore, PIN diodes D5-D20 are switched ON and OFF at the same time. One DC source is applied on Piece 1 and Piece 6 to bias D5-D20.

The developed antenna operates at 2.45 GHz. All the diodes employed in this design

are BAR50-02L with 0403 surface mount packaging from Infineon Technologies. According to the datasheet, the diode can be equivalent to a resistance of 4Ω for the ON state and a resistance of 5 kΩ paralleled with a capacitor of 0.07 pF for the OFF state. All the surface inductors are Coilcraft chip inductors 0402HP-47NX_LU with the value 47 nH. They can choke RF signal at 2.45 GHz while maintaining the DC continuity.

The DC power consumption of the antenna is contributed by switching ON diodes for different working modes. In the antenna measurement, all the diodes are powered by a constant current supply Keithley 2230 SourceMeter. According to the datasheet of PIN diode BAR50-02L, a 10 mA constant current is applied to switch on one diode with a voltage of 0.95 V. Thus, for all the five working modes (Mode 1 - Mode 5) as shown in Table 4.1, the power consumption is in the range of 0.019-0.148 W.

4.2 Results and Discussion

The final optimized values for the parameters of the proposed pattern-reconfigurable antenna are given in Table 4.2. Note that the antenna's operating frequency and impedance matching are determined by the parameters L_1, W, L_b, L_t, and W_f. The parameters d, h_a, L_2, and L_3 are mainly responsible for the radiation performance. One needs to tune appropriate parameters in the optimization process. An antenna prototype shown in Fig. 4.5 was fabricated and measured. Fig. 4.6 shows the simulated and measured $|S_{11}|$ values for Mode 1 - Mode 5. As can be seen, for all the working modes, the measured results agree reasonably well with the simulated ones. Some discrepancies can be found due to differences existing for 20 diodes and fabrication inaccuracies. At working frequency 2.45 GHz, measured and simulated $|S_{11}|$ values are lower than -13 dB for all five modes.

Far-field radiation patterns of the proposed antenna are measured using an NSI-700S-50 spherical near-field antenna measurement system located at the Commonwealth Sci-

Table 4.2: Optimized Values for the Parameters of the Proposed Pattern-Reconfigurable Antenna

Parameter	L_s	W_s	h_s	h_a	L_1	L_2
Value (mm)	70	55	1.5	28	50	25
Parameter	L_3	W	L_g	W_g	L_d	L_f
Value (mm)	12.9	2	60	30	2	39.5
Parameter	W_f	h_f	L_c	L_b	w_b	L_t
Value (mm)	3	1	2.5	6	20	7.6

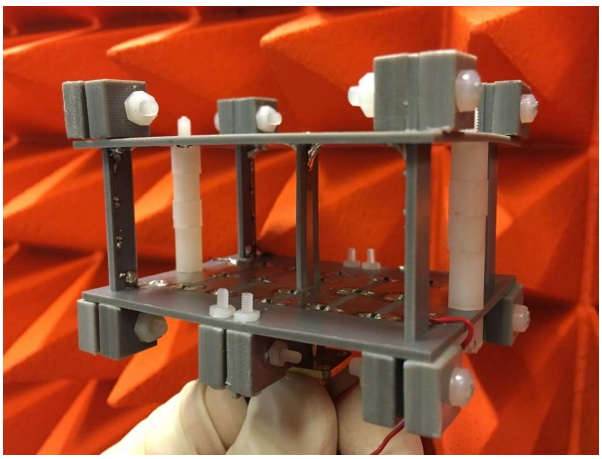

Figure 4.5: Photograph of the fabricated antenna prototype.

entific and Industrial Research Organization, Sydney, Australia. Fig. 4.7 shows the simulated and measured H-plane radiation patterns at 2.45 GHz for Mode 1 - Mode 5. It can be seen that the measured results agree well with the simulated ones. Table 4.3 shows the simulated and measured gains and the measured 3 dB beamwidth. As the beamwidth for the developed antenna is very wide, the main beam direction is calculated as the center of the 3 dB beamwidth. For example, for Mode 3, the main beam direction is at 98° for a 3 dB beamwidth from 46° to 150°. Therefore, the main beam of the developed antenna can be steered to approximate −3° (broadside), 52°, 98° (right endfire), −57°, and −94° (left

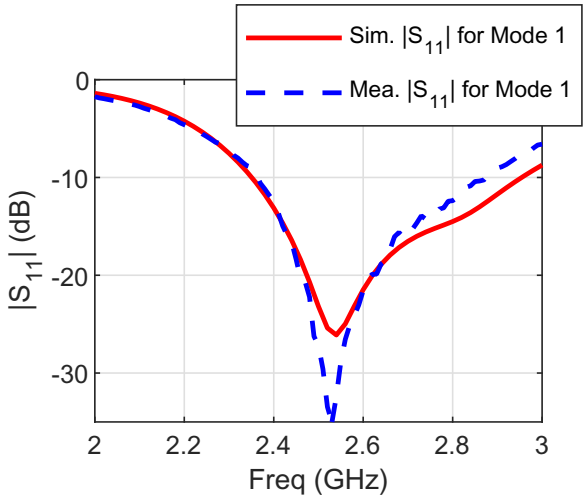

(a)

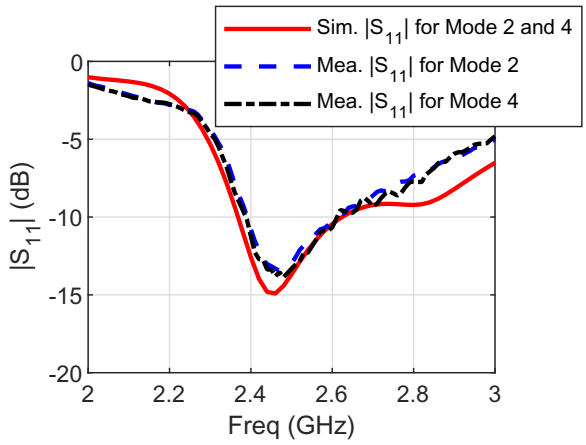

(b)

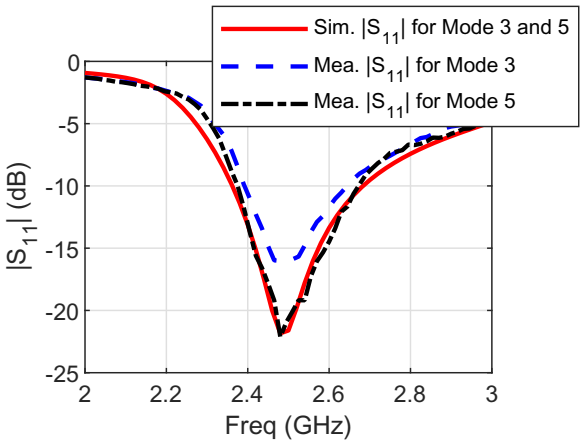

(c)

Figure 4.6: Simulated and measured reflection coefficients. (a) Mode 1. (b) Mode 2 and Mode 4. (c) Mode 3 and Mode 5.

endfire), for Mode 1 to Mode 5, respectively, with realized gains around 5.2–6.5 dBi. The simulated antenna efficiencies are 93.6%, 90.0%, and 92.1% for Mode 1, Mode 2 (Mode 4), and Mode 3 (Mode 5), respectively. The losses on the diodes are in the range of 0.1-0.3 dB with regards to the realized gain of the antenna. The cross-polarization levels for all the five modes are below −10 dB.

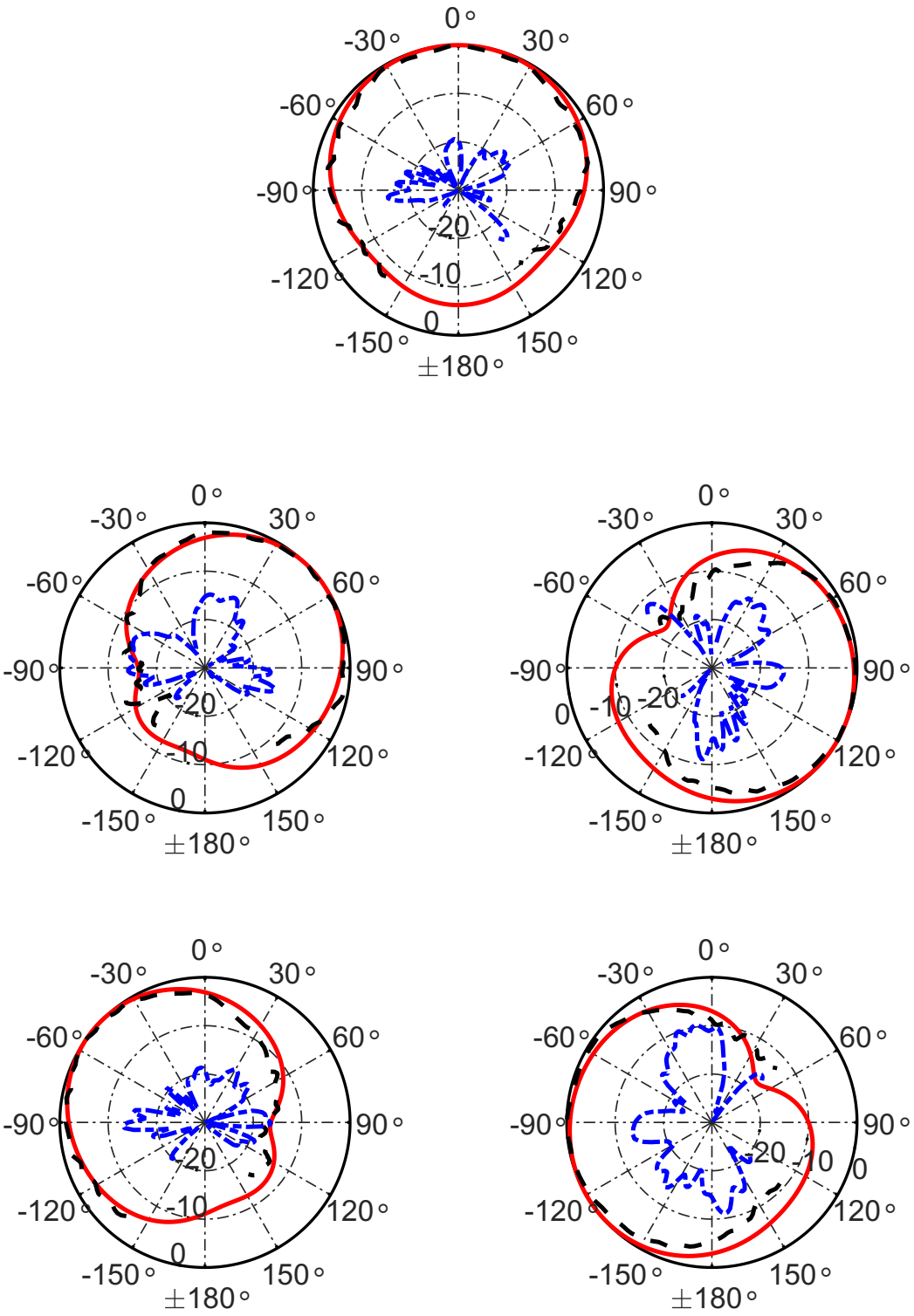

Figure 4.7: Simulated and measured in the H-plane radiation patterns at 2.45 GHz for Mode 1 to Mode 5. (Red solid line: simulated co-pol.; Black dash line: measured co-pol.; Blue dash–dotted line: measured X-pol.)

Table 4.3: Simulated Gains, Measured Gains and Half-Power Beamwidth for Five Pattern Modes

Working Mode	Sim. gain (dBi)	Mea. gain (dBi)	Mea. HPBW
Mode 1	5.0	5.3	$-48^\circ \sim 42^\circ$
Mode 2	6.7	6.5	$-10^\circ \sim 114^\circ$
Mode 3	4.9	5.6	$46^\circ \sim 150^\circ$
Mode 4	6.7	6.2	$-114^\circ \sim 0^\circ$
Mode 5	4.9	5.2	$-144^\circ \sim -44^\circ$

4.3 Conclusion

In this chapter, a pattern-reconfigurable antenna with five switchable beams in elevation plane is developed. The beam switching ability is achieved by reconfiguring parasitic striplines placed around the radiating dipole and reflecting metal pieces under the dipole. Five pattern modes, which are left endfire, left tilted, broadside, right tilted, and right endfire, can be obtained. The measured realized gains for all these five working modes range from 5.2 to 6.5 dBi. This antenna employs a simple structure and exhibits stable radiations, which can serve in many wireless communications systems requiring beam agilities.

Chapter 5

Combined Polarization- and Pattern-Reconfigurable Proximity-Coupled Patch Antenna

Polarization-reconfigurable and pattern-reconfigurable antennas have been examined in Chapter 3 and 4, respectively. These antennas can alter only one characteristic, i.e., either polarization or pattern. Nevertheless, combined two-characteristic reconfigurable antennas are preferable to deliver more diversity and flexibility. In this chapter, a cavity-backed proximity-coupled reconfigurable microstrip antenna is developed to realize both polarization switching and beam steering. Beam lead PIN diodes DSM8100-000 are employed as switching elements to achieve the reconfiguration. Three different linear polarizations (0°, 45°, 90°) are realized by switching the diodes on a proximity-coupled feed network. For each polarization state, the main beam can be steered to three directions by using a reconfigurable parasitic-element network. The parasitic-element network is printed on the same plane of the

radiating patch, thereby making the antenna compact. This antenna has nine different working modes and for all the working modes, the reflection coefficients are below −10 dB with the measured realized gains ranging between 7.2 and 8.1 dBi.

5.1 Reconfigurable Antenna Design and Analysis

5.1.1 Antenna Configuration

The geometry of the developed cavity-backed reconfigurable microstrip antenna is shown in Fig. 5.1. This antenna consists of an upper substrate, a lower substrate and a cavity-backed ground plane. An air gap with a height h_a is introduced between the upper and lower substrates. Both of these two substrates are Rogers RT/Duroid 5880 laminate ($\varepsilon_r = 2.2, \tan\delta = 0.0009$) with the dimensions of $L_s \times L_s \times h_s$.

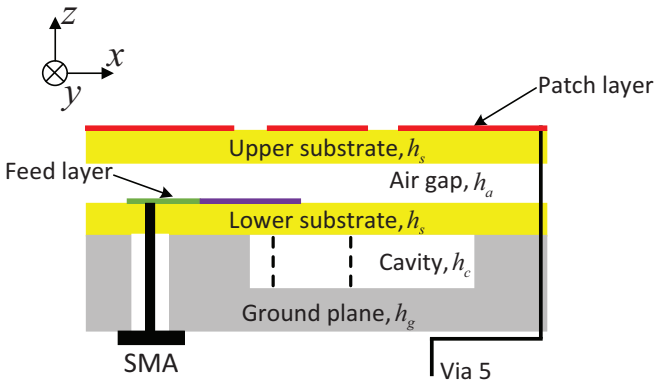

Figure 5.1: Configuration of the developed cavity-backed reconfigurable microstrip antenna.

For the upper substrate, a metal patch layer is etched on the top, whilst the bottom metal is removed. Fig. 5.2 shows the top view of the patch layer. The patch layer consists of a centrally-located square radiating patch with dimensions of $L_p \times L_p$ and a

reconfigurable parasitic-element network. The network is composed of three groups (A, B and C) of parasitic lines and thin biasing strips. As can be seen, the whole structure of the patch layer is symmetrical with regards to diagonal lines PP′ and QQ′.

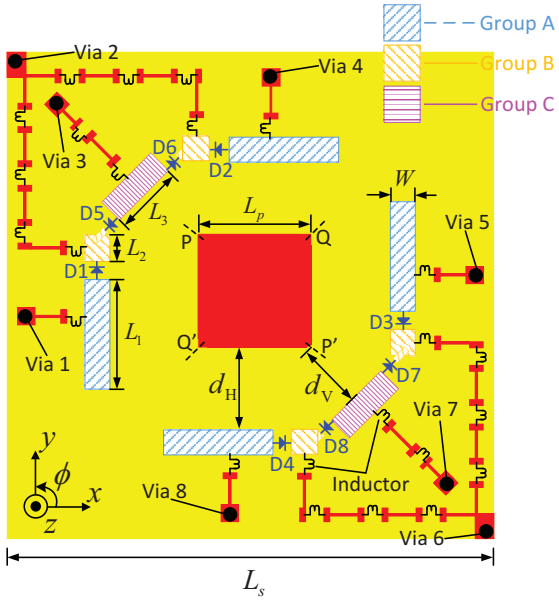

Figure 5.2: Top view of the patch layer.

The three groups of parasitic lines are placed around the radiating patch to achieve pattern reconfiguration. The parasitic line group A and group B have the lengths of L_1 and L_2, respectively. Both of them have a distance of d_{H} to the radiating patch. The parasitic line group C has a length of L_3 with a distance of d_{V} to the radiating patch. All these parasitic lines have a width of W. Four diodes D1 $\sim$ D4 are soldered between group A and group B, and another four diodes D5 $\sim$ D8 are soldered between group B and group C. The DC biasing powers are applied through eight metallic vias (Via 1 $\sim$ Via 8) and thin strips. All the eight metallic vias are drilled from the upper substrate to the bottom ground plane and the DC biasing lines are located behind the ground plane to reduce their effects on the antenna performance. In order to choke RF signals while maintaining the DC continuity, the thin strips are broken down into small sections and

gaps between the sections are bridged with inductors. Here, only the detailed structure of Via 5 with its biasing line is shown in Fig. 5.1 for simplicity.

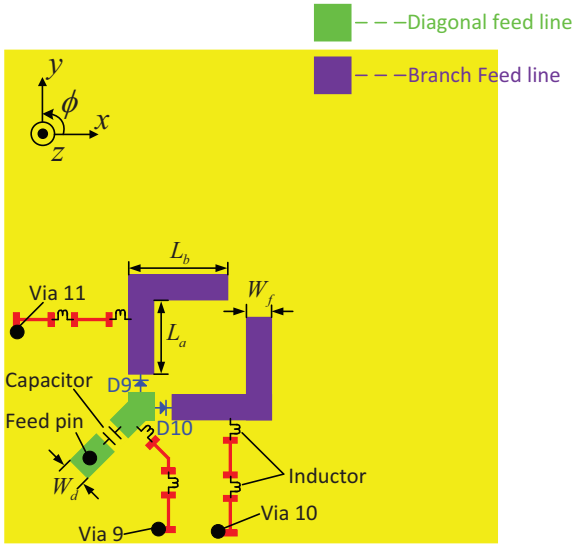

Figure 5.3: Top view of the feed layer.

For the lower substrate, a metal feed layer is printed on the top, whilst the bottom metal is removed. Fig. 5.3 shows the details of the top view of the feed layer. A diagonal feed line with a width of W_d is connected to an SMA feed pin and a thin slot is cut for soldering a capacitor to choke the DC signal while maintaining the RF continuity. Two diodes D9 and D10 are soldered between the diagonal feed line and two symmetrical branch feed lines to achieve the polarization reconfiguration. Both of the two branch feed lines have a length of $L_a + L_b$ and a width of W_f. The DC biasing voltages are applied through three metallic vias (Via 9 $\sim$ Via 11) and thin strips to control the diodes D9 and D10. Under the lower substrate, it is an L-shape cavity-backed ground plane with a thickness of h_g. Top view of the cavity-backed ground plane is shown in Fig. 5.4, and the dimensions of the air cavity are $L_c \times W_c \times h_c$. This cavity-backed ground plane is employed for the impedance match [113]-[114].

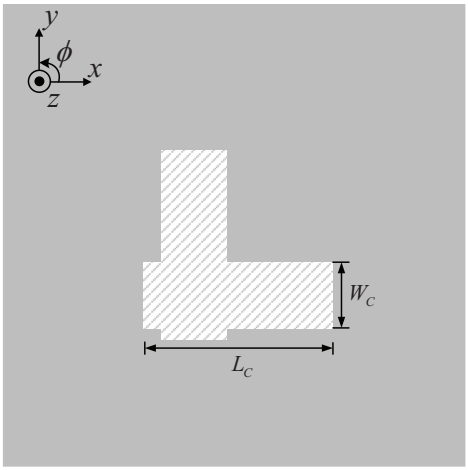

Figure 5.4: Top view of the cavity-backed ground plane.

5.1.2 Polarization Reconfiguration and Beam Steering Mechanism

The antenna is able to reconfigure the polarization states and steer its main beam independently. As can be seen, the antenna uses a proximity-coupled feed network with an air gap introduced between the feed lines and the radiating patch. Thus, polarization reconfiguration can be realized by reconfiguring the feed lines. Meanwhile, the air gap provides enough space to place the reconfigurable feed network on the feed layer. Once the polarization state is selected, the beam steering can be conducted by switching diodes D1 $\sim$ D8 between the three-group parasitic lines.

For the polarization reconfiguration, as shown in Fig. 5.3, two PIN diodes D9 and D10 are used to connect or disconnect the diagonal feed line and two branch feed lines. Three different polarizations can be reconfigured by controlling the states of these two diodes. When D9 is ON and D10 is OFF, $\phi = 0°$ polarization which is aligned with x axis can be obtained. Similarly, $\phi = 90°$ polarization along y axis can be obtained when D9 is OFF and D10 is ON. When both D9 and D10 are ON, $\phi = 45°$ polarization along the diagonal

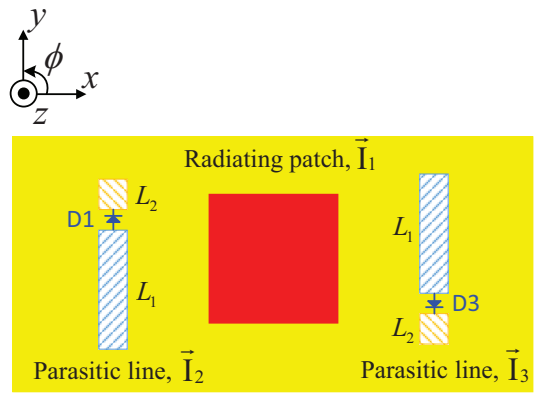

(a)

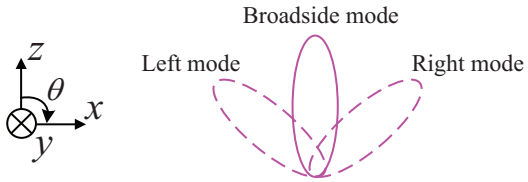

(b)

Figure 5.5: Demonstration of beam steering mechanism. (a) Three-element array. (b) Pattern modes.

line can be obtained by equally combining the x-axis current and y-axis current.

For each of these three polarization states, beam steering can be obtained by using the reconfigurable parasitic-element network as shown in Fig. 5.2. The basic mechanism of the beam steering is to consider the radiating patch with two parasitic lines as a three-element array. The beam can be steered by changing the phase of the parasitic lines. Take the y-polarized ($\phi = 90°$) state as an example as shown in Fig. 5.5(a), the center radiating patch has a current $\vec{I}_1 = I_1 e^{j\psi_1}\vec{y}$, where $\vec{y}$ represents unit current vector along y axis. Two different parasitic lines have coupled currents $\vec{I}_2 = I_2 e^{j\psi_2}\vec{y}$ and $\vec{I}_3 = I_3 e^{j\psi_3}\vec{y}$. The phases of coupled currents are determined by lengths and positions of the parasitic lines. In this work, the positions of the parasitic lines are fixed and only their lengths are

changeable. More specifically, when both the diodes D1 and D3 are OFF, the two active parasitic lines are of the same lengths (L_1). In this case, the main beam is towards the broadside direction which is defined as Broadside mode, as shown in Fig. 5.5(b). When D1 is ON and D3 is OFF, the left active parasitic line ($L_1 + L_2$) is longer than the right one (L_1). In this case, the main beam steers to $+x$ axis direction, which is defined as Right mode. On the contrary, when D1 is OFF and D3 is ON, the pattern is steered to $-x$ axis direction, which is defined as Left mode.

Based on this working mechanism, the pattern reconfiguration for $\phi = 0°$ polarization state can be achieved using the parasitic lines group A and group B with the switching diodes D2 and D4, as can be seen in Fig. 5.2. Parasitic lines group B and group C with diodes D5 $\sim$ D8 are utilized to switch the beam for the $\phi = 45°$ polarization state. Thus, for each of these three polarization states, three modes that are Broadside mode, Left mode, and Right mode can be achieved by controlling the diodes. Overall, the antenna has nine working modes. Table 5.1 shows the working states of the PIN diodes for each mode.

5.1.3 DC Feed Network Design

The developed antenna operates at 11 GHz. Usually, for relative low working frequencies such as 2.4 GHz, the DC lines are very thin in terms of the wavelength. Thus, the DC biasing lines can be treated as high impedance lines, and little currents will be coupled on the feed lines. However, at 11 GHz, DC lines could have much more effects on the antenna performance as the electric sizes of the DC lines have largely increased. Therefore, the DC feed network should be carefully optimized. The biasing network in this work consists of metallic feed vias and thin strips. In order to reduce the power coupled on the feed vias (Via 1 $\sim$ Via 11), the positions of the vias have been carefully chosen where little effects have been found on the antenna's S-parameters and radiation patterns. Furthermore,

Table 5.1: Nine Reconfigurable Working Modes

Working mode	Diodes switched ON	Polarization	Pattern mode
Mode 1	D9	0°	Broadside
Mode 2	D9 D2	0°	Left ($-y$)
Mode 3	D9 D4	0°	Right ($+y$)
Mode 4	D10	90°	Broadside
Mode 5	D10 D3	90°	Left ($-x$)
Mode 6	D10 D1	90°	Right ($+x$)
Mode 7	D9 D10	45°	Broadside
Mode 8	D9 D10 D7 D8	45°	Left($-x$,$+y$)
Mode 9	D9 D10 D5 D6	45°	Right($+x$,$-y$)

in order to reduce the effects of the biasing strip lines on the antenna, the strip lines are broken down into small sections and the gaps between the sections are bridged with inductors, as shown in Figs. 5.2 and 5.3.

Diodes used in this design are beam lead PIN diodes DSM8100-000, which can work up to 25 GHz. According to the datasheet, the diode can be modeled as a resistance of 4 Ω for the ON state and as a parallel circuit with a capacitance of 0.03 pF and a resistance of 20kΩ for the OFF state. Ten diodes will be used as the switching elements. All the surface-mount inductors are Coilcraft chip inductors 0402HP-3N6X_LU (3.6 nH) with a self-resonant frequency at 11.7 GHz. They can choke the RF signal while maintaining DC signals at 11 GHz. In order to avoid the DC signal flowing into the coaxial feed, a capacitor with 2 pF is used on the diagonal feed line, as shown in Fig. 5.3.

Table 5.2: Optimized Parameters for Cavity-Backed Proximity-Coupled Reconfigurable Microstrip Antenna

Parameter	h_s	h_a	L_s	h_g	L_p	W_f	L_c	W_c
Value (mm)	0.508	2	32	4	6.5	1.5	12.5	5
Parameter	h_c	L_1	L_2	L_3	L_a	L_b	d_{H}	d_{V}
Value (mm)	3	7.1	2.25	5.6	6.2	7	5	3.8

5.2 Parameter Study and Discussion

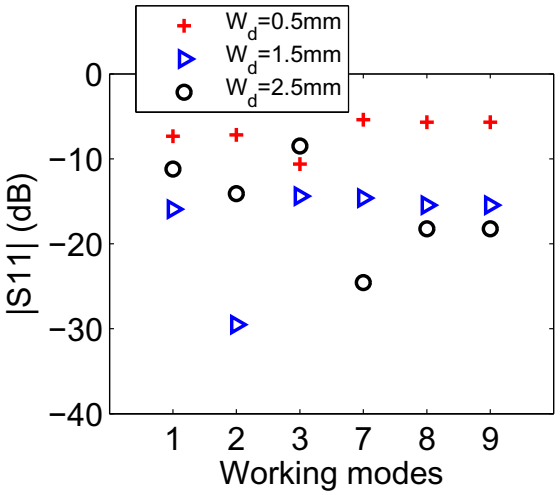

Figure 5.6: Input reflection coefficients versus feed line width of W_d for different working modes.

The antenna is studied and simulated using full-wave simulation tool ANSYS HFSS. The final parameters of the antenna are given in Table 5.2. For the proposed polarization and pattern reconfigurable antenna, one challenge is to realize acceptable impedance matches for the three polarization states. The input impedances of the 0° and 90° polarization states are the same, while they are different from that of the 45° polarization

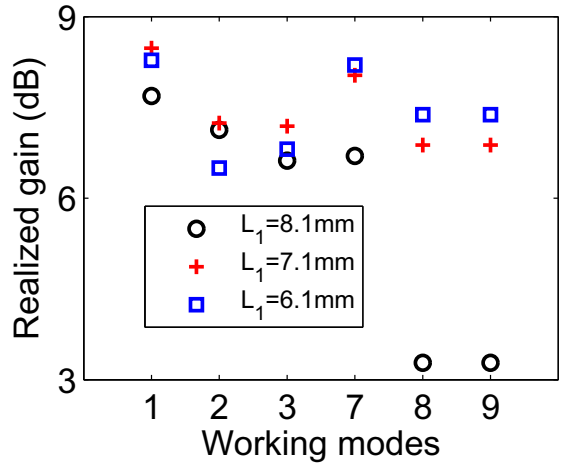

(a)

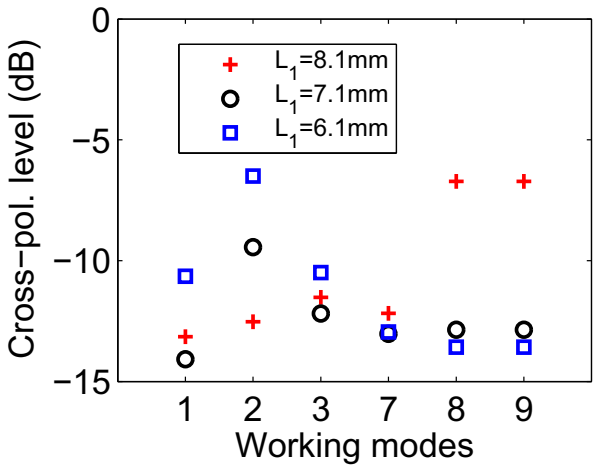

(b)

Figure 5.7: Realized gains and cross-polarization levels versus parasitic line length of L_1 for different working modes. (a) Realized gains. (b) Cross-polarization levels.

state. In order to achieve acceptable reflection coefficients for all these three states, the diagonal feed line width W_d is optimized. A parametric study of W_d was conducted and the results are shown in Fig. 5.6. As can be seen, when $W_d = 0.5$ mm, the antenna has a high reflection for all working modes. For $W_d = 2.5$ mm, the antenna has a relative high

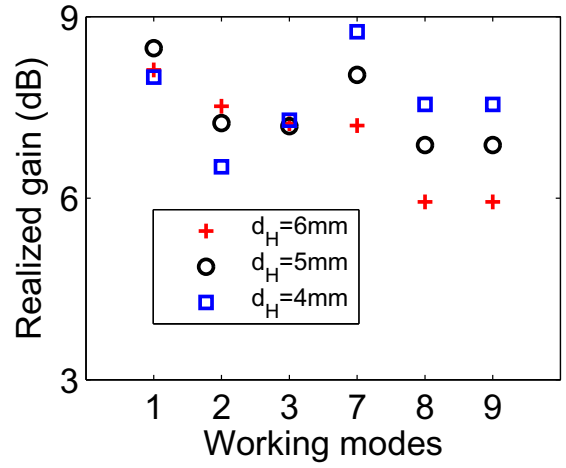

(a)

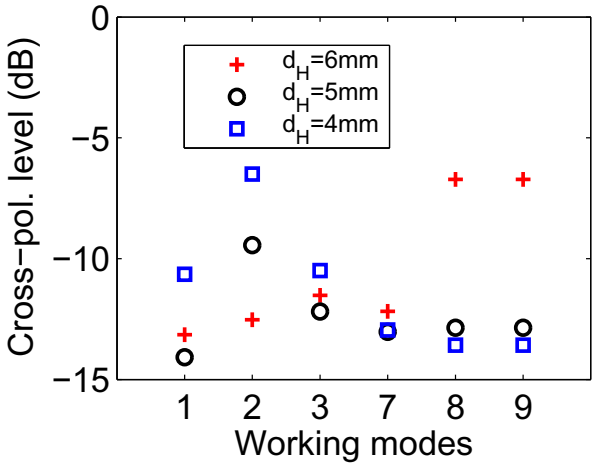

(b)

Figure 5.8: Realized gains and cross-polarization levels versus distance of d_{H} for different working modes. (a) Realized gains. (b) Cross-polarization levels.

reflection at working Mode 3. Thus, to achieve an acceptable $|S_{11}|$ for all the working modes, $W_d = 1.5$ mm is selected.

As discussed in Section 5.1, the coupling between the radiating patch and the parasitic lines is crucial for the pattern reconfiguration. The lengths of parasitic lines affect

radiation patterns. Furthermore, the distance between radiating patch and parasitic lines plays an important role in titling the pattern. Here, parameter studies on the length of L_1 and distance of d_{H} are shown in Fig. 5.7 and Fig. 5.8, respectively.

Fig. 5.7 shows the realized gains and cross-polarization levels versus the length L_1 for each working mode. As can be seen from Fig. 5.7, when $L_1 = 8.1$ mm, the realized gains reduce to about 3 dBi for working modes 8 and 9. When $L_1 = 7.1$ mm and $L_1 = 6.1$ mm, the realized gains are relatively more stable for all the working modes. In addition, the cross-polarization levels for $L_1 = 6.1$ mm are higher than the ones for $L_1 = 7.1$ mm. Therefore, $L_1 = 7.1$ mm is selected. Fig. 5.8 shows the realized gains and cross-polarization levels versus the length d_H for each working mode. When $d_H = 5$ mm, the antenna can achieve more stable gains than the ones with $d_H = 6$ mm and $d_H = 4$ mm. Moreover, when $d_H = 5$ mm, the cross-polarization levels for all working modes are relative lower. Therefore, $d_H = 5$ mm is selected.

5.3 Results and Discussion

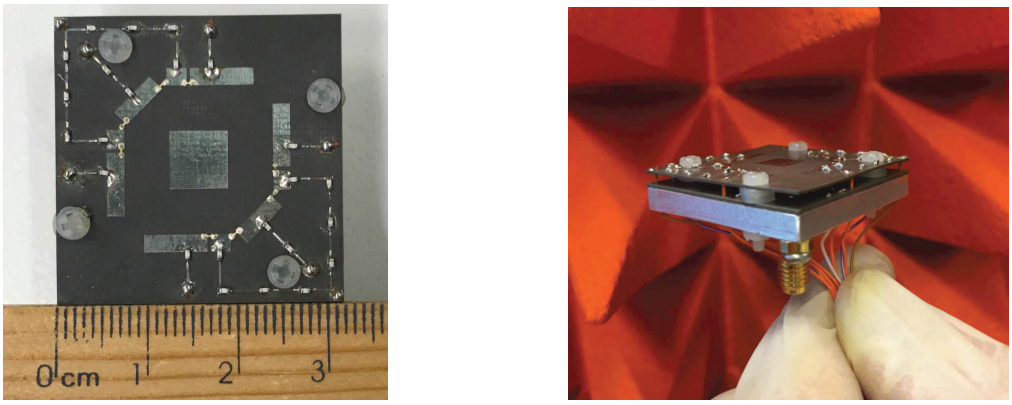

(a) (b)

Figure 5.9: Prototype of the developed cavity-backed reconfigurable microstrip antenna. (a)Top view. (b) Overall view.

Based on the above analysis, an antenna prototype was fabricated as shown in Fig. 5.9. The PIN diodes are attached to the antenna using electrically conductive silver epoxy (EPO-TEK H70E-1LB Kit from Epoxy Technology). A Keithley 2230 SourceMeter power supply is employed to provide constant currents for biasing the diodes. According to the datasheet of PIN diode DSM8100-000, a typical power to turn on one diode is a 10 mA current with a voltage of 0.95 V. For all the nine working modes of the developed polarization and pattern reconfigurable antenna, the power consumption is in the range of 0.095 W (One PIN diode is ON) to 0.38 W (Four diodes are ON). By switching the ten diodes, nine working modes with different radiation performance can be achieved. Fig. 5.10 shows the simulated and measured S-parameters at 11 GHz for each mode. As can be seen, the measured S-parameters agree reasonably well with the simulated ones. All the values of the measured $|S_{11}|$ are below -10 dB at 11 GHz except that the one is -9.0 dB for Mode 7. Some discrepancies can be found, which could be mostly attributed to the individual differences of the PIN didoes. Furthermore, the inaccuracies of the fabrication process, such as the biasing network, may affect the antenna performance.

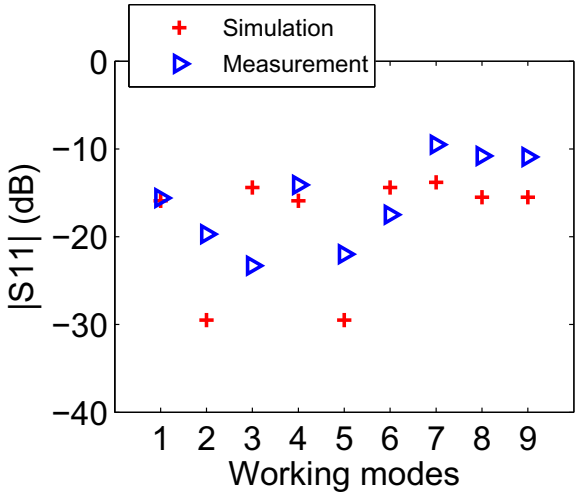

Figure 5.10: Simulated and measured $|S_{11}|$ at 11 GHz for all the nine working modes.

Far-field radiation patterns were measured for different modes of the developed an-

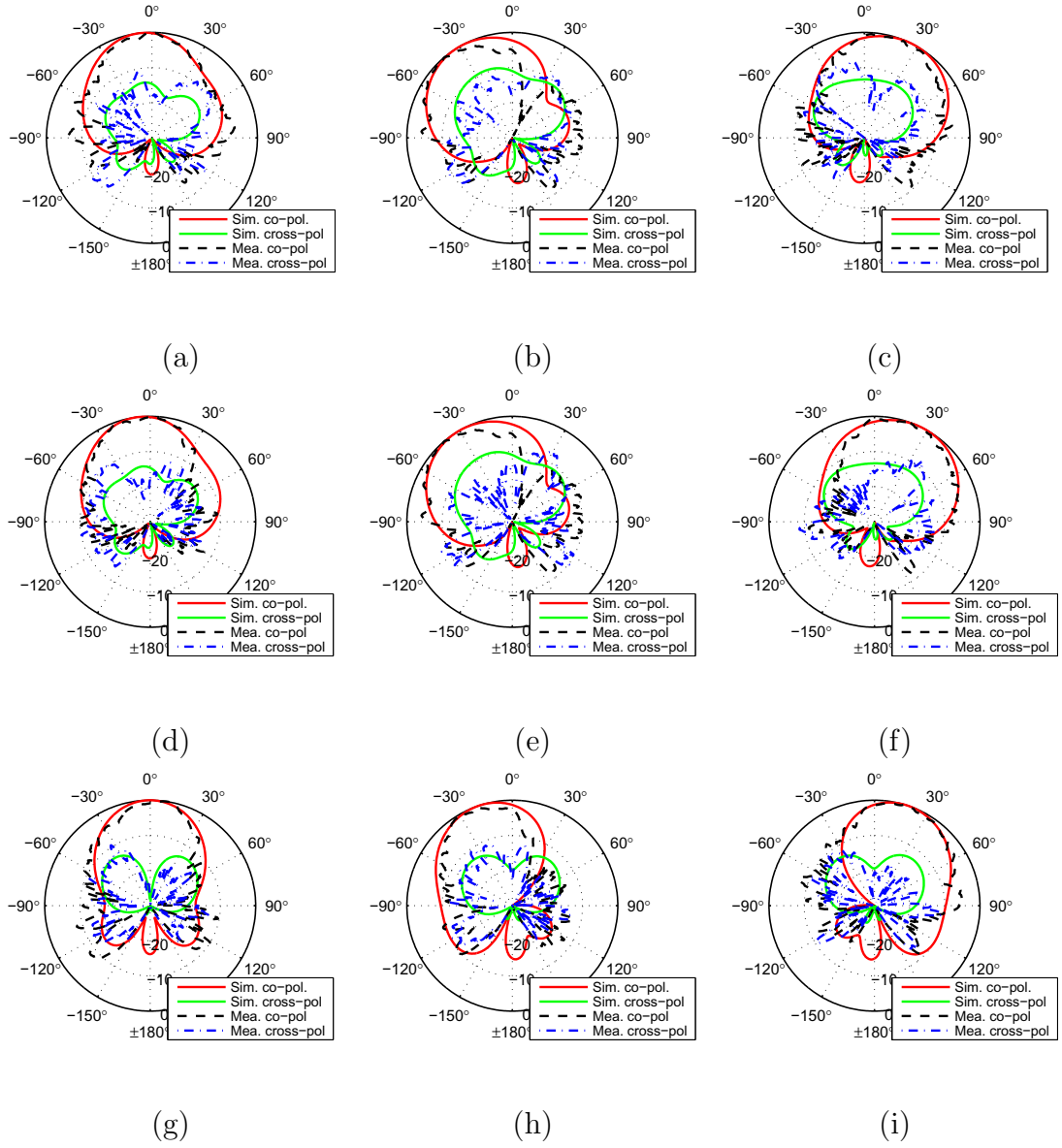

Figure 5.11: Simulated and measured H-plane radiation patterns at 11 GHz for all the nine working modes. (a) Mode 1. (b) Mode 2. (c) Mode 3. (d) Mode 4. (e) Mode 5. (f) Mode 6. (g) Mode 7. (h) Mode 8. (i) Mode 9.

Table 5.3: Simulated and Measured Realized Gains for All the Nine Working Modes

Realized gain	0° polarization		
	Mode 1	Mode 2	Mode 3
Simulation (dBi)	8.48	7.24	7.19
Measurement (dBi)	8.04	7.22	7.38
Realized gain	90° polarization		
	Mode 4	Mode 5	Mode 6
Simulation (dBi)	8.48	7.24	7.19
Measurement (dBi)	7.83	7.62	7.81
Realized gain	45° polarization		
	Mode 7	Mode 8	Mode 9
Simulation (dBi)	8.04	6.88	6.88
Measurement (dBi)	8.12	7.42	7.25

tenna using a spherical near-field (SNF) antenna measurement system NSI-700S-50 located at CSIRO, Australia. For H-plane radiation patterns, as can be seen from Fig. 5.11, the measured results agree reasonably well with the simulated ones. Table 5.3 shows the simulated and measured realized gains at all the nine working modes. At $\phi = 0°$ polarization state, the measured gains can achieve 8.04, 7.22, and 7.38 dBi for Mode 1 $\sim$ Mode 3. Moreover, the measured half-power beamwidth (HPBW) can cover from $-24° \sim 21°$, $-68° \sim -17°$, and $-7° \sim 48°$, respectively. It means that the HPBW for 0° polarization can reach a wide angle from $-68° \sim 48°$ with a gain around 7.2 dBi. Similarly, at $\phi = 90°$ polarization state, for Mode 4 $\sim$ Mode 6, the measured gains can reach 7.83, 7.62, and 7.81 dBi. Meanwhile, the HPBW can cover from $-68° \sim 50°$. At $\phi = 45°$ polarization state, the measured gains for the three modes are 8.12, 7.42, and 7.25 dBi respectively.

The HPBW patterns can cover from $-49^\circ \sim 49^\circ$.

5.4 Conclusion

In this chapter, the technology for combined pattern and polarization reconfigurable antennas has been advanced by developing a novel cavity-backed proximity-coupled reconfigurable microstrip antenna. It can switch between three linear polarization states $\phi = 0^\circ$, $\phi = 45^\circ$, $\phi = 90^\circ$. For each polarization state, the main beam in H plane can be steered to about 20°, 0°, -20° with a relative stable gain performance by reconfiguring the feed network and the parasitic-element network. The realized gains range from 7.2 to 8.1 dBi for all these working modes. The pattern and polarization diversities provided by the antenna can be exploited to improve the performance of various wireless systems including MIMO systems, cognitive radio systems, and multifunction consumer wireless devices.

Chapter 6

Frequency-Based Pattern-Reconfigurable Circularly Polarized Leaky-Wave Antenna

In the previous chapters, a variation of resonant antennas that can reconfigure one or more characteristics has been investigated and discussed thoroughly. As another widely used antenna type, non-resonant antennas that can realize the reconfigurable characteristics are attractive. Leaky-wave antennas are good candidates due to their inherent frequency-based pattern-reconfigurable capability, i.e., they can scan the main beam by varying the source frequency. In this chapter, a novel benzene-ring-shaped slot-loaded substrate-integrated-waveguide (SIW) LWA with partially reflecting wall (PRW) vias is developed and verified to realize wide-angle continuous circular-polarization (CP) beam scanning with consistent gain. The dispersion feature of slot-loaded SIW LWAs with PRW vias is theoretically explored using an equivalent circuit model. The CP radiation feature is investigated numerically utilizing the E-

and H-field distributions of an initial design and its equivalent magnetic currents. The results of these studies are used to demonstrate that improved CP performance over a wide-angle scan range can be attained with a change from a standard slot shape to a benzene-ring-shaped slot. The resulting benzene-ring-shaped slot-loaded CP SIW LWA was optimized, fabricated, and measured. The measured results verify that a continuously scanned CP beam through a wide angle from backward to forward directions with a consistent gain is achieved. The prototype exhibits a continuous 97.1° CP beam scan with a gain variation between 8 and 11.3 dBic when the source frequency is swept from 9.35 to 11.75 GHz.

6.1 Unit Cell Requirements to Achieve Continuous Beam Scanning

Initially, a non-slotted SIW unit cell with partially reflecting wall (PRW) vias was investigated. It is labelled as Unit A in Fig. 6.1. It is designed on a two-layer copper-clad substrate. The substrate is chosen as F4BM-2 produced by Wangling Company, and the permittivity (ε_r), loss tangent (tanδ), width (w_{sub}) and thickness are 3.02, 0.001, 30 mm and 1 mm, respectively. A main patch with a width of w_p is printed on top of the substrate, and a solid ground plane is placed at the bottom. Two rows of shorting vias are used for connecting the patch to the ground plane. The shorting vias in the upper row have a diameter d_1 and a center-to-center distance S. They act as a electric wall of the SIW LWA. The shorting vias in the lower row have a diameter d_2 and are separated by a larger distance P and serve as the PRW. The length of unit cell is also P.

The analysis of the unit cell is conducted using transmission line theory [115]. The corresponding Unit A equivalent circuit is depicted as shown in Fig. 6.1. For clearer

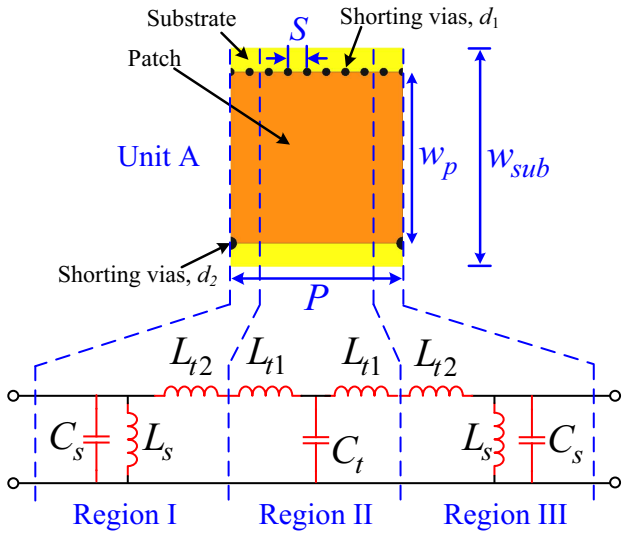

Figure 6.1: Top view of the unit cell, Unit A, and its corresponding equivalent circuit.

explanations, the entire unit cell is divided into three regions, marked as Regions I, II and III. The series inductances L_{t1} and L_{t2} are introduced by the indicated regions of the main patch, and the shunt capacitances C_t and C_S are caused by the the capacitive effects between the corresponding regions and the ground plane. The shunt inductance L_s is introduced by the PRW vias. Due to the placement of the series inductances L_{t1} and L_{t2}, a total inductance of L_t is used for simplicity in the analysis.

The transmission (ABCD) matrix of Unit A is then calculated as:

$$\begin{bmatrix} A & B \\ C & D \end{bmatrix} = \begin{bmatrix} 1 & 0 \\ 1/(j\omega L_s) & 1 \end{bmatrix} \times \begin{bmatrix} 1 & 0 \\ j\omega C_s & 1 \end{bmatrix} \times \begin{bmatrix} 1 & j\omega L_t \\ 0 & 1 \end{bmatrix} \times \begin{bmatrix} 1 & 0 \\ j\omega C_t & 1 \end{bmatrix} \times \begin{bmatrix} 1 & j\omega L_t \\ 0 & 1 \end{bmatrix} \times \begin{bmatrix} 1 & 0 \\ j\omega C_s & 1 \end{bmatrix} \times \begin{bmatrix} 1 & 0 \\ 1/(j\omega L_s) & 1 \end{bmatrix} \tag{6.1}$$

where, ω is the angular frequency $\omega = 2\pi f$, and $L_t = L_{t1} + L_{t2}$. The dispersion characteristic is expressed in terms of the transmission line parameters as [86]:

$$\beta = \frac{1}{P}\cos^{-1}(\frac{A+D}{2}) \tag{6.2}$$

By solving (6.1) and (6.2), the wave number β can be represented as:

$$\beta = \frac{1}{P}\cos^{-1}[-C_t L_t^2 C_s \omega^4 - (2L_t C_s + L_t C_t + \frac{C_t L_t^2}{L_s})\omega^2 + 2L_t L_s + 1] \tag{6.3}$$

To obtain the circuit parameter values, one can extract the approximate total patch inductance L and total capacitance C of Unit A using the following equations [116]:

$$L \approx \mu_r \mu_0 P h / w_p, \quad \text{and} \quad C \approx \varepsilon_r \varepsilon_0 w_p P / h \tag{6.4}$$

where μ_r is the relative permeability of the substrate, μ_0 is the permeability of free space, ε_r is the relative permittivity of the substrate, ε_0 is the permittivity of free space, and h is the thickness of the substrate. The values (in millimeters) of the Unit A parameters are: $w_p = 10.7$, $P = 10.8$, $S = 1.2$, $d_1 = 0.5$, $d_2 = 1$, $h = 1$. Substituting these parameter values into (6.4), the resultant inductance $L \approx 1$ nH and capacitance $C \approx 3.3$ pF are obtained. As $L = 2L_t$ and $C = 2C_s + C_t$, the values for L_t, C_s and C_t become: $C_s = 1$ pF, $L_t = 0.5$ nH, $C_t = 1.3$ pF. Furthermore, the inductance L_s of the shorting vias can be approximately calculated as [117]:

$$L_s \approx 2h(\ln \frac{4h}{d_2} + 1) \times 10^{-6} \tag{6.5}$$

Then by substituting the values of h and d_2 into it and considering the parallel inductive effects of the shorting vias in the upper row, the inductance L_s of the shorting vias is approximately obtained as: $L_s \approx 0.3$ nH.

Applying these calculated circuit parameter values to (6.3), one can calculate its dispersion feature. The results are labeled as *Equivalent circuit* in Fig. 6.2. As a comparison, Unit A is also simulated using the eigenmode solver in the full-wave finite element (FEM) simulator ANSYS High Frequency Structure Simulator (HFSS). The resultant dispersion

diagram is labeled as *Eigenmode simulation* in Fig. 6.2. It is seen that the dispersion diagram obtained from the equivalent circuit reasonably agrees with the one from the eigenmode simulation. Referring to Fig. 6.2, it is known that the left region of the air line is the leaky wave region, i.e., $\beta \leq k_0$. Thus, the LWAs employing Unit A can only radiate forward beams at its fundamental ($n = 0$) mode.

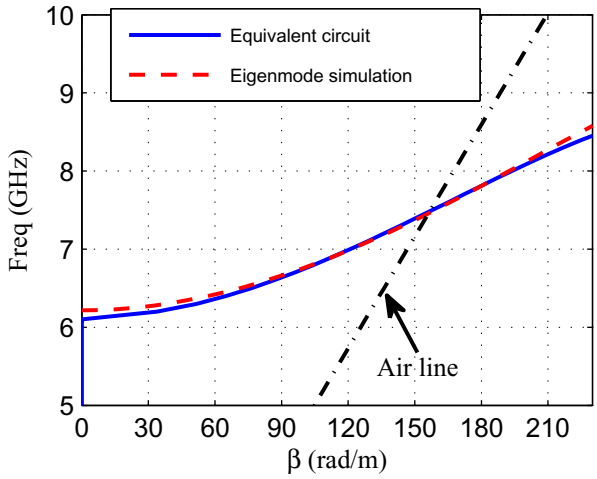

Figure 6.2: Dispersion diagrams of the Unit A model obtained with equivalent circuit and eigenmode simulations.

In the previous work [118], a slot-loaded SIW LWA with PRW vias was reported that produced a continuously scanned LP beam. To achieve a continuous backward-to-forward scanned CP beam, a new unit cell (referred as Unit B) is developed; it is depicted in Fig. 6.3. Unit B has an I-shaped slot centered on the main patch. As indicated, the dimensions of the slot are w_s, l_h, and l_v. Based on the Unit A analysis, the Unit B equivalent circuit is given in Fig. 6.3. The equivalent circuits corresponding to Regions I and III are the same as those of Unit A. In contrast, it is different in Region II. The shunt inductance L_h and shunt capacitance C_h are introduced by the horizontal part of the I-shaped slot; the series capacitance C_v is caused by its vertical part. For simplicity, the capacitance introduced between the patch and the ground plane is included in the

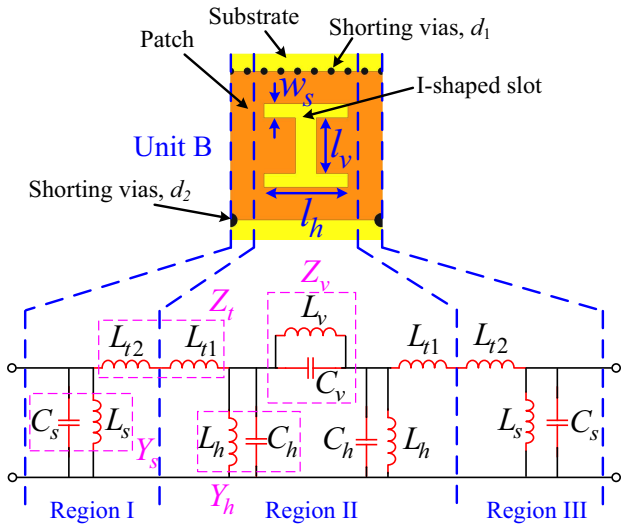

Figure 6.3: Unit B model and its corresponding equivalent circuit.

shunt capacitance C_h. Again, the series inductances L_{t1}, L_{t2}, and L_v are introduced by the main patch.

With these additional elements, the transmission (ABCD) matrix of Unit B becomes:

$$\begin{bmatrix} A & B \\ C & D \end{bmatrix} = \begin{bmatrix} 1 & 0 \\ Y_s & 1 \end{bmatrix} \times \begin{bmatrix} 1 & Z_t \\ 0 & 1 \end{bmatrix} \times \begin{bmatrix} 1 & 0 \\ Y_h & 1 \end{bmatrix} \times \begin{bmatrix} 1 & Z_v \\ 0 & 1 \end{bmatrix} \times \begin{bmatrix} 1 & 0 \\ Y_h & 1 \end{bmatrix} \times \begin{bmatrix} 1 & Z_t \\ 0 & 1 \end{bmatrix} \times \begin{bmatrix} 1 & 0 \\ Y_s & 1 \end{bmatrix} \tag{6.6}$$

where element admittances and impedances are

$$\begin{aligned} Y_s &= j\omega C_s + \frac{1}{j\omega L_s}, \quad Z_t = j\omega L_t \\ Y_h &= j\omega C_h + \frac{1}{j\omega L_h}, \quad Z_v = 1/(j\omega C_v + \frac{1}{j\omega L_v}) \end{aligned} \tag{6.7}$$

By solving (6.2) and (6.6), the dispersion relation can be expressed in terms of the wave number as:

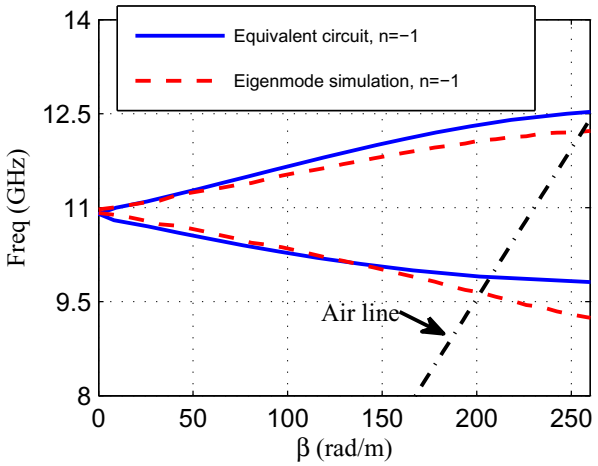

Figure 6.4: Unit B dispersion diagrams obtained from its equivalent circuit and eigenmode simulation.

$$\beta = \frac{1}{P}\cos^{-1}[Z_t Z_v Y_s Y_h (Z_t Y_h + 2) + Z_t Y_h (2Z_t Y_s + Z_v Y_h) + (2Z_t + Z_v)(Y_s + Y_h) + 1] \tag{6.8}$$

To realize continuous beam scanning, the operating mode of any periodic SIW LWA should be a higher harmonic, such as $n = -1$ harmonic. The optimized dimensions for the I-shaped slot (in millimeters) are: $l_h = 6$, $l_v = 4$, $w_s = 1$. The corresponding updated circuit parameters are: $L_t = 0.52$ nH, $L_h = 0.15$ nH, $C_h = 0.6$ pF, $L_v = 0.53$ pF, and $C_v = 1$ pF, while L_s and C_s remain the same ($L_s = 0.3$ nH, $C_s = 1$ pF). Substituting these circuit parameter values into (6.7) and (6.8), the resulting dispersion relation of the $n = -1$ mode dispersion of Unit B is shown in Fig. 6.4 and labeled as *Equivalent circuit*. The corresponding dispersion curve obtained from the eigenmode solver is also shown in Fig. 6.4 and labeled as *Eigenmode simulation*. Both curves agree reasonably well in Unit B's leaky wave region. One observes that there is a continuous transition between the negative and positive regions of the dispersion curves at 10.9 GHz, i.e., the matched condition has been satisfied. Consequently, Unit B has no open stopband (OSB). This

feature appears in contrast to Unit A because the etched I-shaped slot and the PRW vias co-excite the higher harmonic $n = -1$ mode. Therefore, the Unit B-based SIW LWA can realize continuous beam scanning through broadside.

6.2 I-Shaped Slot-Loaded SIW LWA with PRW Vias

The continuous beam scanning and CP performance of the I-shaped slot-loaded SIW LWA with PRW vias is analyzed. Details of the antenna configuration are given. The resulting continuous beam scanning and CP features are simulated.

6.2.1 Antenna Configuration

An I-shaped slot-loaded SIW LWA with PRW vias is developed with six Unit B cells to illustrate its performance characteristics. Fig. 6.5 shows the top view of the entire antenna configuration. Its optimized dimensions (in millimeters) are summarized in Table 6.1. It is also constructed with the aforementioned two-layer copper-clad F4BM-2 substrate. Two tapered pads, tapering from a width of w_a to a width of w_b over the length of l_t, are used to connect the 50 Ω feed line to the main patch over a wide bandwidth. The antenna is fed from the left end and terminated on the right end with a matching 50 Ω load.

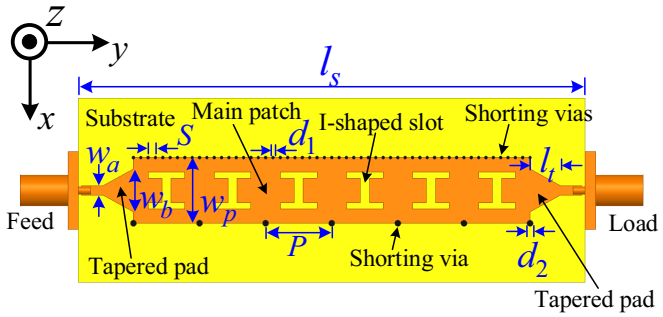

Figure 6.5: I-shaped slot-loaded SIW LWA with PRW vias configuration.

Table 6.1: Optimized Design Parameters of the I-shaped Slot-loaded SIW CP LWA with PRW Vias

Parameter	l_s	w_a	w_b	l_t	S	d_1	d_2	P
Value (mm)	82.8	1.5	7	5	1.2	0.5	0.8	10.8

6.2.2 Beam Scanning

The main beam angle accomplished through the above complete six-cell system simulation is shown in Fig. 6.6, and the results are labeled as *Complete structure simulation*. Based on the dispersion properties obtained from the eigenmode simulation shown in Fig. 6.4, the main beam angles can be calculated, and the corresponding results are labeled as *Unit eigenmode simulation* in Fig. 6.6 for comparison. It is seen that both results agree very well. The minor discrepancies arise from the difference between the finite length of the complete structure and the infinite length of the eigenmode-based results. Note that when the source frequency is swept from 9.75 to 12.0 GHz, the main beam of the finite structure is continuously scanned from $-56°$ to $+54°$, through $110°$.

The simulated directivity and AR values of the six-cell system are presented in Fig. 6.7. The directivity values vary between 6.8 and 11.5 dBic. The AR values are greater than 3 dB across the operating band except for a very narrow frequency range around 11.1 GHz where the AR is $\leq$ 3 dB.

6.2.3 Circular Polarization Analysis

To analyze the CP performance of the six-cell system, one can introduce its equivalent electric and magnetic current sources. According to Huygens' principle [119], the antenna's far-field radiation can be determined from these equivalent sources. Fig. 6.8 shows the simulated electric and magnetic fields just above one Unit B in the system in

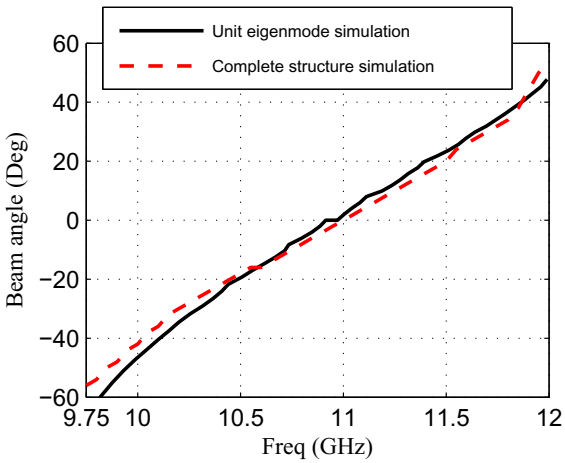

Figure 6.6: Main beam angle when the source frequency is varied as calculated from the simulations of the eigenmode (infinite) and complete (finite) structure.

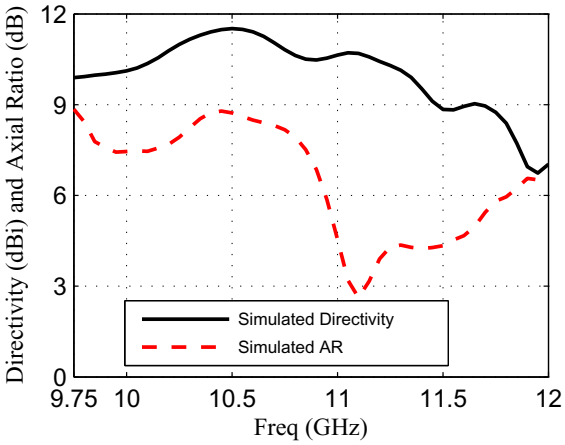

Figure 6.7: Simulated directivity and axial ratio values of the six-cell I-shaped slot-loaded SIW LWA with PRW vias.

Fig. 6.3 at $t = 0$ and $\pi/4$ for 10.5 GHz. It is seen that the magnetic fields are very small and negligible. Consequently, only these near-field electric fields are considered for the analysis of the far-field radiation performance. They are mainly distributed above the etched I-shaped slot and the PRW vias.

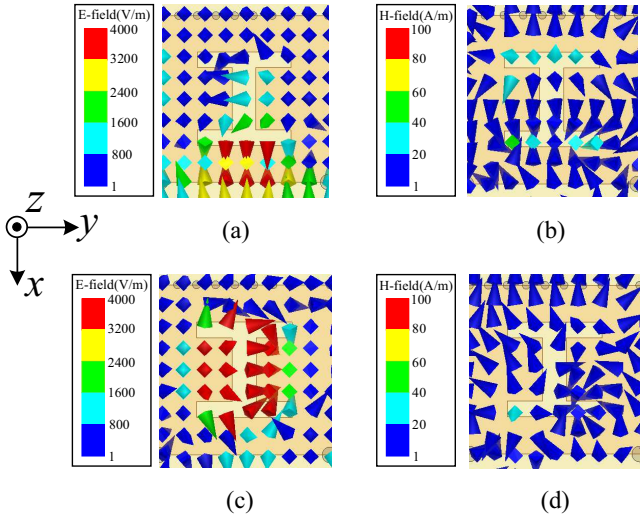

Figure 6.8: Top view of the field distribution on the Unit B at 10.5 GHz. (a) E-fields distribution ($t = 0$). (b) H-field distribution ($t = 0$). (c) E-fields distribution ($t = \pi/4$). (d) H-fields distribution ($t = \pi/4$).

To emphasize this distribution more clearly, Fig. 6.9(a) shows the simulated E-field components $\mathbf{E}_t$, $\mathbf{E}_m$, $\mathbf{E}_b$, and $\mathbf{E}_{prw}$ above one Unit B cell. As shown in Fig. 6.9 (b), the corresponding equivalent magnetic currents are calculated as:

$$\begin{aligned} \mathbf{M}_t = \mathbf{E}_t \times \hat{\mathbf{n}}_z; \quad \mathbf{M}_m = \mathbf{E}_m \times \hat{\mathbf{n}}_z; \\ \mathbf{M}_b = \mathbf{E}_b \times \hat{\mathbf{n}}_z; \quad \mathbf{M}_{prw} = \mathbf{E}_{prw} \times \hat{\mathbf{n}}_x \end{aligned} \tag{6.9}$$

where $\hat{\mathbf{n}}_x$, and $\hat{\mathbf{n}}_z$ are the unit vectors along the $+x$ axis and $+z$ axis, respectively. Note that the two horizontal magnetic currents $\mathbf{M}_t$ and $\mathbf{M}_b$ along the y-axis direction are introduced by the two horizontal parts of the etched I-shaped slot. Similarly, the horizontal magnetic current $\mathbf{M}_{prw}$ along the y-axis direction is produced by the PRW vias. The

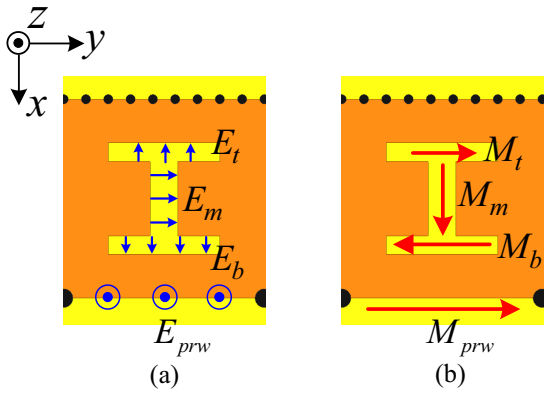

Figure 6.9: Unit B radiation mechanism analysis. (a) E-fields distribution. (b) Equivalent magnetic current sources.

vertical current $\mathbf{M}_m$ along the x-axis direction is introduced by the vertical part of the etched I-shaped slot. Then, the total equivalent magnetic source $\mathbf{M_{tot}}$ is:

$$\mathbf{M_{tot}} = \mathbf{M_x} + \mathbf{M_y} \tag{6.10}$$

where

$$\mathbf{M_x} = \mathbf{M}_m \quad \text{and} \quad \mathbf{M_y} = \mathbf{M}_t + \mathbf{M}_b + \mathbf{M}_{prw} \tag{6.11}$$

It is obvious that to form a circularly polarized wave, the two magnetic current components, i.e. $\mathbf{M_x}$ along the x-axis direction and $\mathbf{M_y}$ along the y-axis direction, need to have the same amplitude and a 90° phase difference. It is found for this six-cell I-shaped slot-loaded system that $\mathbf{M}_{prw}$ is approximately out of phase with $\mathbf{M}_b$, and $\mathbf{M}_t$ is relatively small. As a consequence, $\mathbf{M_y}$ is much smaller than $\mathbf{M_x}$. Therefore, the noted poor AR values are observed. To improve the AR performance, a different unit cell had to be developed.

6.3 Benzene-Ring-Shaped Slot-Loaded SIW CP LWA with PRW Vias

The benzene-ring-shaped slot-loaded SIW CP LWA with PRW vias is introduced to achieve much improved AR values. Its continuous beam scanning and CP performance is demonstrated. Details of the antenna configuration are given. The resulting continuous beam scanning and CP features are analyzed and simulated.

6.3.1 Antenna Configuration

Guided by the field distribution analysis of the I-slots, it was found that one can manipulate the etched slots and optimize the PRW vias to improve the AR values. In particular, a new slot-loaded unit cell was developed. It is labelled as Unit C in the top right inset of Fig. 6.10(a). Its evolution from Unit B with the I-slot is depicted in the three subplots of Fig. 6.10(a). The top and bottom horizontal parts of the I-shaped slot were first rotated

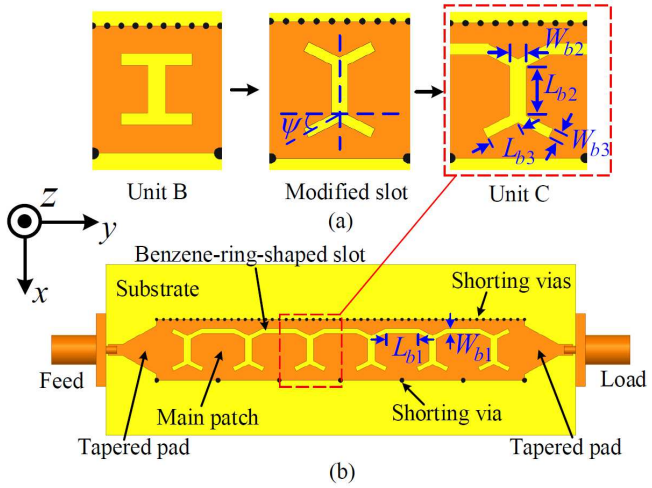

Figure 6.10: Benzene-ring-shaped slot-loaded SIW CP LWA with PRW vias. (a) Evolution of Unit C from Unit B. (b) Complete six-cell based structure.

to an angle of ψ ($\psi = 45°$). This modification reduced the magnetic current contribution $\mathbf{M}_b$ found in Fig. 6.9. These modified slots were then connected to the counterparts in the adjacent cells using additional horizontal slots on the upper side of the patch. These additional horizontal slots add another y-axis magnetic current component to balance $\mathbf{M}_x$ and $\mathbf{M}_y$. The final shape is reminiscent of a benzene ring. Furthermore, by cascading these benzene-ring-shaped slot unit cells, it was found that their longer length slots enhance the guiding characteristics of the traveling wave in the SIW structure in comparison to their resonant I-shaped parent. Six benzene-ring-shaped slot-loaded Unit C cells were then combined with the tapered feed and termination segments to form the SIW LWA with PRW vias shown in Fig. 6.10(b). The dimensions of the benzene-ring-shaped slots are represented by the parameters L_{b1}, W_{b1}, L_{b2}, W_{b2}, L_{b3}, and W_{b3} in Fig. 6.10.

6.3.2 Design Parameter Study

With the knowledge that the CP performance of a slot-loaded SIW LWA with PRW vias is dependent on the precise shape of its etched slots and the PRW vias, the design parameters of the benzene-ring-shaped slot and PRW vias combination were carefully investigated and optimized. In particular, parameter studies of the slot widths W_{b1}, W_{b2}, and the PRW via radius D_2 were performed. When the value of the studied parameter was changed, the values for the other parameters were fixed.

Fig. 6.11 shows the AR values as a function of the source frequency for different values of W_{b1}. It is seen that when $W_{b1} = 0.7$ mm, the AR values exceed 3 dB between 10.1 and 11.4 GHz. However, when the value of W_{b1} increases to 0.85 mm, good CP performance below 3.1 dB is obtained within the whole operating band from 9 to 11.5 GHz. With a further increase of W_{b1} to 1.0 mm, the overall CP performance again deteriorates, the values of AR being more than 3 dB. Consequently, it is seen that W_{b1} has a high impact on the antenna's CP performance.

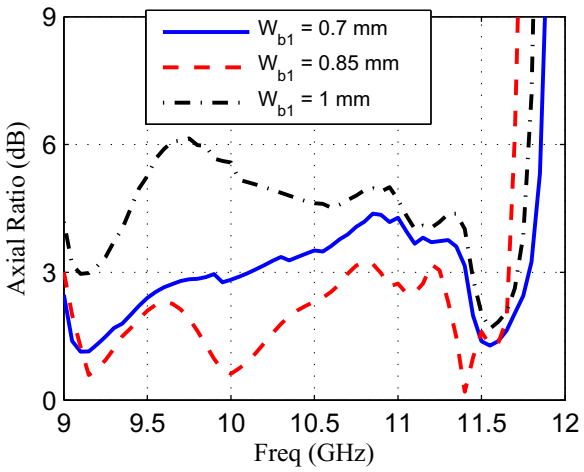

Figure 6.11: The axial ratio (AR) values as a function of the source frequency for different values of W_{b1}.

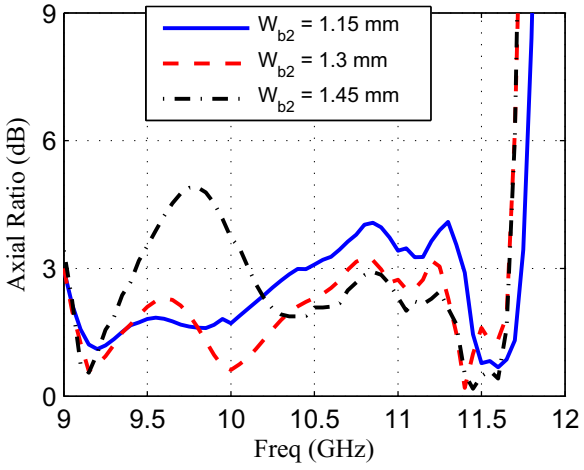

Figure 6.12: The axial ratio (AR) values as a function of the source frequency for different values of W_{b2}.

Fig. 6.12 shows the AR values as a function of the source frequency for different values of W_{b2}. Good CP performance is obtained for $W_{b2} = 1.3$ mm. In contrast, the AR values in the higher frequency band from 10.5 to 11.4 GHz become worse when the value of W_{b2} reduces to 1.15 mm. Similarly, the AR values in the lower frequency band from 9.45 to 10.1 GHz deteriorate when the value of W_{b2} increases to 1.45 mm. Thus, $W_{b2} = 1.3$ mm was chosen to balance the CP performance in both the lower and higher frequency bands and yielded good CP performance over the entire operating band from 9 to 11.5 GHz.

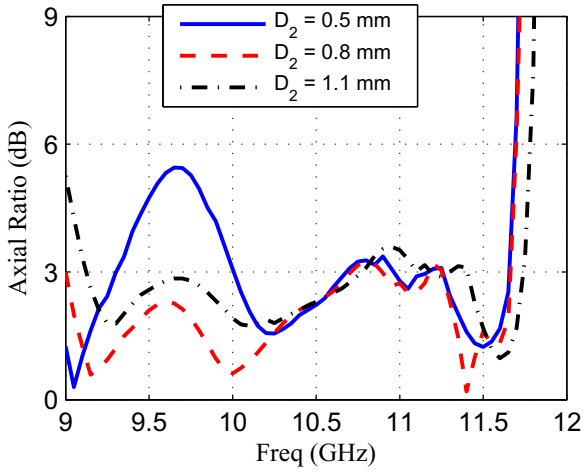

Figure 6.13: The axial ratio (AR) as a function of the source frequency for different values of D_2.

Finally, Fig. 6.13 shows the AR values as a function of the source frequency for different values of D_2. It is seen that when $D_2 = 0.5$ mm, the AR values remain below 3.2 dB except in the lower frequency band from 9.3 to 10 GHz. When D_2 increases to 0.8 mm, the AR performance is improved and the AR values are all below 3.1 dB. When D_2 further increases to 1.1 mm, the AR performance remains similar, but the operating band blue shifts to higher frequencies.

The final optimized parameter values are listed in Table 6.2.

Table 6.2: Optimized Values of the Design Parameters of the Benzene-Ring-Shaped Slot-Loaded SIW CP LWA with PRW Vias

Parameter	l_s	W_a	W_b	L_t	S	D_1	D_2
Value (mm)	82.8	2	8.5	6	1.2	0.5	0.8
Parameter	P	L_{b1}	W_{b1}	L_{b2}	W_{b2}	L_{b3}	W_{b3}
Value (mm)	10.8	5.75	0.85	3.9	1.3	2.7	0.8

6.3.3 Simulated and Measured Results

Based on the optimum design parameter values, the benzene-ring-shaped slot-loaded CP SIW LWA with PRW vias was fabricated and measured. Fig. 6.14 shows a photograph of the fabricated prototype.

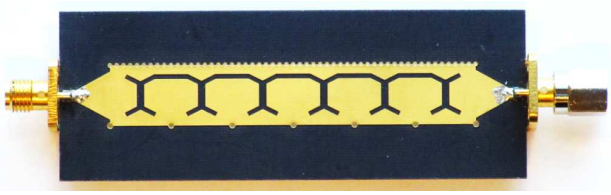

Figure 6.14: Photograph of the fabricated benzene-ring-shaped slot-loaded CP SIW LWA with PRW vias prototype.

The simulated and measured S-parameters are compared in Fig. 6.15. It is seen that the simulated $|S_{11}| \leq -10$ dB operating bandwidth is from 9.2 to 11.65 GHz. When the source frequency is reduced from 9.3 down to 9.0 GHz, the simulated $|S_{11}|$ value remains below -6.4 dB. The measured $|S_{11}| \leq -10$ operating bandwidth is from 9.7 to 11.94 GHz. For frequencies between 9.35 and 9.7 GHz, the measured $|S_{11}|$ is ≤ -6.6 dB. Noted that the measured $|S_{11}|$ values show a blue shift to higher operating frequencies. Simulations indicate that this is caused by fabrication inaccuracies. The simulated $|S_{21}|$ values are below -10 dB for frequencies lower than 11.45 GHz. They peak at 11.6 GHz

with the value of −8.23 dB. The measured $|S_{21}|$ values are always below −13.6 dB. The simultaneously measured low $|S_{11}|$ and $|S_{21}|$ values indicate that the system has good radiation performance.

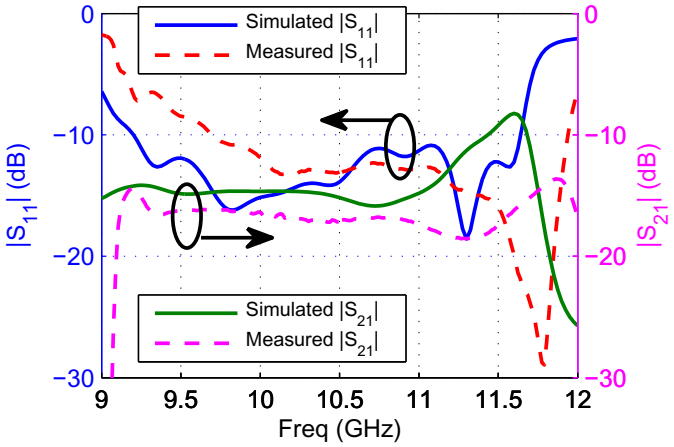

Figure 6.15: Simulated and measured S-parameters of the benzene-ring-shaped slot-loaded CP SIW LWA with PRW vias.

Fig. 6.16 displays the simulated gain patterns at five different frequencies. It illustrates that the main beam can be continuously scanned from backward to forward directions through broadside. The main beam points in the backward direction at 9 GHz with the leftmost angle of −46°. With the increase in the source frequency, the beam moves towards the broadside. For instance, the main beam angle is −26° at 9.25 GHz. The main beam points in the broadside direction at 9.8 GHz. Fig. 6.17 shows the simulated 3-D gain pattern at 9.8 GHz. It is seen that the antenna radiates a fan beam that has a narrow beamwidth with respect to the yz-plane and a wide beamwidth with respect to the zx-plane. When the source frequency is further increased, the main beam moves into the forward directions, e.g., the main beam angle is +32° at 10.75 GHz. The main beam points at the rightmost angle (+64°) at 11.5 GHz. Thus, the simulated beam scanning range is 110° as the source frequency is swept from 9 to 11.5 GHz.

The far-field radiation patterns of the prototype were measured using the Satimo

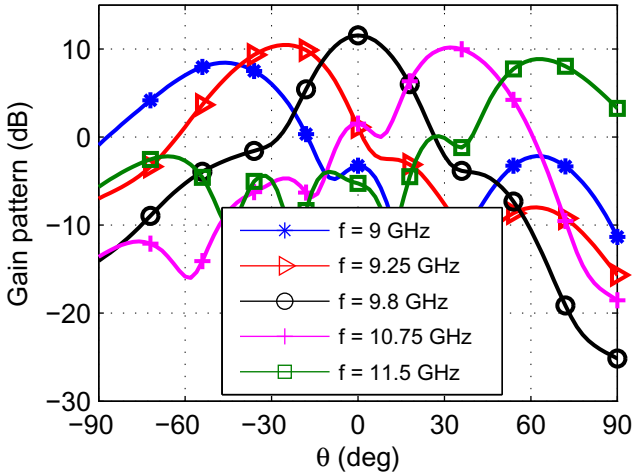

Figure 6.16: Simulated gain patterns of the optimized design at five different frequencies.

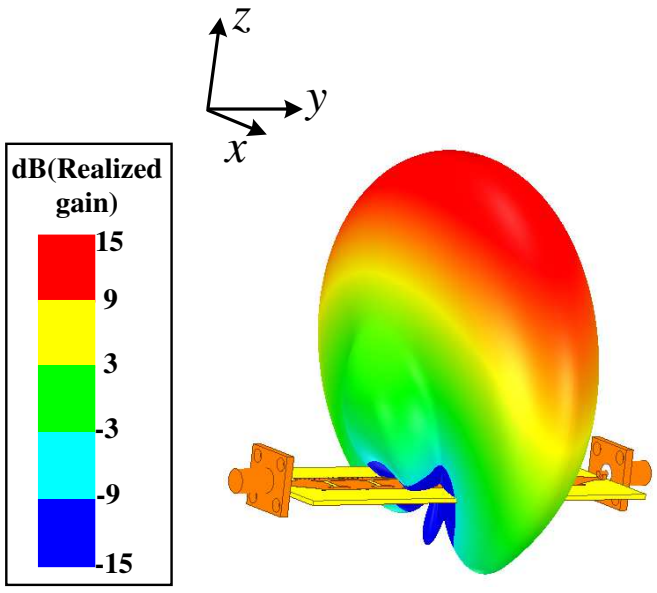

Figure 6.17: Simulated 3-D gain pattern of the optimized design at 9.8 GHz.

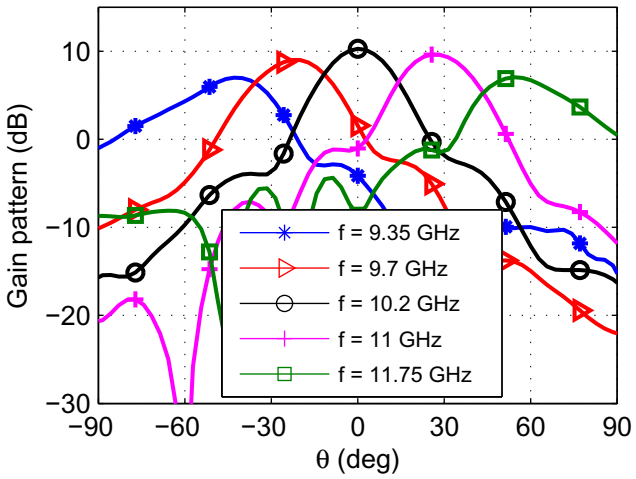

Figure 6.18: Measured gain patterns of the prototype at five different frequencies.

multi-probe spherical near-field system StarLab-18 located at Xiamen University, China. The measured gain patterns at five different frequencies are shown in Fig. 6.18. When the operating frequency is 9.35, 9.7, 10.2, 11, 11.75 GHz, the main beam angle is $-42.8°$, $-22.8°$, $0°$, $+25.7°$, and $+54.3°$, respectively. The measured beam scanning range is $97.1°$ as the source frequency varies from 9.35 to 11.75 GHz.

Fig. 6.19 compares the simulated and measured AR values along with the realized gain values as functions of the source frequency. As noted previously, the simulated AR values are below 3.1 dB within the operational frequency range from 9 to 11.5 GHz. The corresponding realized gain values vary between 8.44 and 11.56 dBic. Due to the shift of the measured results to higher frequencies, the AR values below 3 dB occur in the band from 9.45 to 11.75 GHz. The AR value below this band at 9.35 GHz, for example, is 4.1 dB. From 9.35 to 11.75 GHz, the measured realized gain is stable with only a 3.3 dB gain variation between 8 and 11.3 dBic.

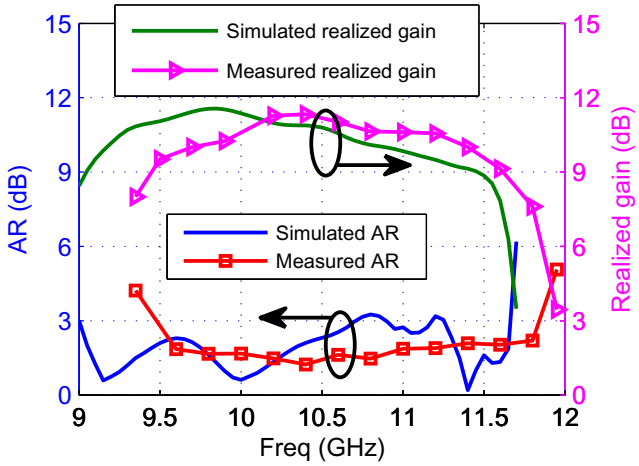

Figure 6.19: Simulated and measured axial ratio (AR) values together with the corresponding realized gain values as functions of the source frequency.

6.4 Discussion

Considering its potential applications, the current study was focused on achieving a LWA system that realizes wide-angle CP beam scanning with a consistent gain. While there are examples of systems that can scan a CP beam over a large angular range, it generally remains a very challenging problem. The goal was achieved by introducing a novel unit cell with a benzene-ring-shaped slot and using it to construct a six-cell SIW LWA with PRW vias. Continuous beam scanning in a wide angular range with consistent gain was realized with an optimized design. When compared to previously reported CP LWAs [76–79,83], it is found that the antenna system developed in this chapter exhibits superior performance in terms of its beam scanning range and its realized gain consistency.

6.5 Conclusion

A benzene-ring-shaped slot-loaded CP SIW LWA with PRW vias was presented. It was demonstrated that it realizes continuous beam scanning from its backward to forward directions through a wide angular range with consistent realized gain. It was shown that an I-shaped slot-loaded LWA with PRW vias supports continuous beam scanning, but the AR values in the main beam directions are very high. To achieve the CP beam scanning in a wide angle range with consistent gain, a novel benzene-ring-shaped slot-loaded SIW LWA with PRW vias was developed and optimized. A prototype system was fabricated and tested. The measured results demonstrate that the beam radiated by this system can be scanned from $-42.8°$ to $+54.3°$, i.e., continuous beam scanning through $97.1°$, was realized, and it has a commensurate gain variation of 3.3 dBic between 8 and 11.3 dBic. The reported CP LWA is a highly promising candidate for future wireless systems for which there exists a prominent demand for high performance antennas that are low cost and exhibit multiple functionality.

Chapter 7

Frequency-Based Pattern-Reconfigurable Leaky-Wave Antenna with Polarization Flexibility

Frequency-based continuous beam scanning LWA has been explored and discussed in the previous chapter. It has been acknowledged that combined two-characteristic reconfigurable antennas are promising for increasing the diversity and capacity for future wireless systems. In this chapter, a simple single-layer reconfigurable leaky-wave antenna (LWA) is presented that achieves both beam-scanning functionality and polarization agility. This LWA system realizes a scanned beam that can be switched between all of its linear polarization (LP) and circular polarization (CP) states using only one DC biasing source. A slot-loaded SIW-based LWA is first explored to attain CP performance with frequency-based continuous beam scanning through broadside. This CP LWA realizes a measured CP performance with a 3 dB gain variance within 2.75−3.35 GHz for scan angles ranging from −28.6° to

+31.5°. A row of shorted stubs is then incorporated into the CP LWA to obtain similar LP performance. Finally, by introducing PIN diodes into this LP LWA configuration to facilitate reconfigurable connections between the main patch and the shorted stubs, the radiated fields can be switched between all of its CP and LP states. Measured results of all three antennas confirm their simulated performance. It is demonstrated that the main beam of the polarization-reconfigurable LWA can be scanned from −31.5° to +17.1° with gain variations between 9.5 and 12.8 dBic in its CP state, and from −34.3° to +20° with them between 7.8 and 11.7 dBi in its LP state.

7.1 Frequency-Based Beam Steerable CP LWA

The design, simulation, fabrication, and measurement of this antenna are presented. The measured and simulated performance characteristics are in good agreement.

7.1.1 Antenna Configuration

The CP LWA configuration is shown in Fig. 7.1. It employs a two-layer copper-clad substrate. The permittivity (ε_r), loss tangent (tanδ), and height of the substrate were selected to be 3.02, 0.001, and 3.175 mm, respectively. The width of the substrate is W_s. The main patch is etched on the top layer and centered on the substrate. It has the width W_m, where $W_m < W_s$. The bottom layer is a solid metallic ground plane. The main patch is terminated with two symmetrical, centrally printed tapered matching pads, one at each end. The tapering of each end pad occurs over the length L_t. Their widths vary from W_b (the wide width, connected to the main patch and with $W_b < W_m$) to W_a (the narrow width connected to the terminations). These tapered structures are a simple and effective method to attain a wide band impedance matching.

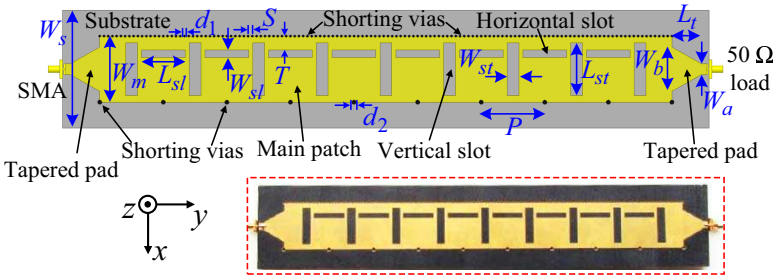

Figure 7.1: Top view of the CP LWA. Photograph of the prototype antenna is shown in the bottom inset.

The LWA is fed from the left side with a SMA and is terminated with a 50 Ω load on the right side. The 50 Ω load is used to absorb any power of the traveling wave remaining in the guiding structure to prevent it from being reflected back towards the SMA. The coaxial SMA's inner conductor has a diameter of 1.28 mm. It is connected directly to the narrow width of the left tapered pad. Its outer conductor has the diameter 4.1 mm and is connected directly to the ground plane.

A row of closely spaced vias with a center-to-center distance S short the upper edge of the main patch to the bottom ground plane. The diameter of these vias is d_1, where $2d_1 > S$. A second row of vias short the lower edge of the main patch to the bottom ground plane. They are separated by a much larger center-to-center distance P and have the diameter d_2. These two rows of vias form a substrate-integrated-waveguide (SIW) structure.

Two groups of slots, i.e., a set of vertical slots and a set of horizontal slots, are etched on the main patch. The width and length of each vertical slot are W_{st} and L_{st}, respectively. They are W_{sl} and L_{sl}, respectively, for each horizontal slot. The vertical slots are centrally etched on the main patch. The horizontal slots are etched at a distance T from the upper row of shorting vias. The partially open edge formed by the bottom row of shorting vias (with large separation) leads to some power leakage into the far field in the horizontal xy-plane. The antenna radiates primarily in the transverse yz-plane.

The slot-loaded, partially open-edge, SIW unit cell of the CP LWA is shown in the inset of Fig. 7.2. The length and width of this unit cell are P (the period) and W_s, respectively. The horizontal and vertical slots are clearly displayed. Half of each horizontal slot is shared with the neighboring unit cells. The upper side of the unit cell is completely shorted with the narrowly-spaced vias; the other is shorted with two half-vias, the other halves being shared with the neighboring unit cells. The finite LWA shown in Fig. 7.1 is composed of nine such unit cells.

7.1.2 Working Mechanisms

Compared to a conventional open-edge SIW based antenna that radiates through its fundamental $n = 0$ mode [14], the antenna in Fig. 7.1 can radiate through its $n = -1$ spatial harmonic. This radiation mechanism is facilitated by the periodic structure formed with both the horizontal slots and vertical slots.

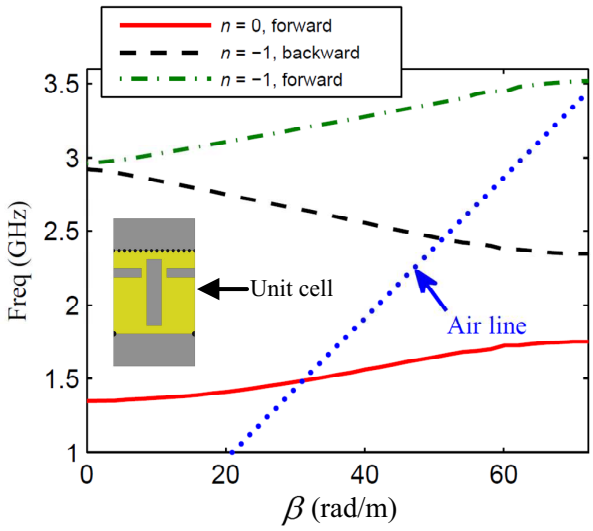

Figure 7.2: Dispersion diagrams of the $n = -1$ and 0 spatial harmonics and the unit cell configuration of the CP LWA.

Fig. 7.2 shows the dispersion diagrams of the unit cell for the $n = -1$ and $n = 0$

harmonics. They were obtained using the Eigenmode solver in the HFSS. It is known that the leaky wave region is on the left side of the air line, and the main beam direction is determined approximately by the following equation [9]:

$$\theta(f) \approx \sin^{-1}\left[\frac{\beta_n(f)}{k_0(f)}\right] \tag{7.1}$$

where for a specific frequency, θ is the main beam direction of the radiation pattern measured from the broadside. The term k_0 is the wave number in free space, and β_n is the phase constant of the n-th leaky mode, e.g., the $n = -1, 0$ modes. The dispersion diagrams for the $n = -1$ harmonic indicate that it can be used to scan the antenna continuously from the backward to the forward direction because there is no band gap between its backward and forward modes.

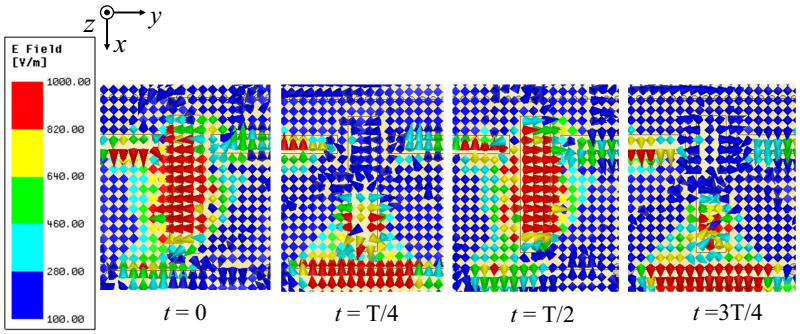

Figure 7.3: Top view of E-field distribution on the surface just above one unit cell of the main patch of the optimized CP LWA at 2.8 GHz for four time snapshots separated by a quarter period.

The CP beam scanning feature is realized by optimizing the dimensions of the horizontal and vertical slots that are etched on the main patch with HFSS Optimetrics, i.e., the HFSS parameter analysis. For a clear illustration of the CP properties, top views of the electric field just above one unit cell for four time snapshots with a quarter period separation are given in Fig. 7.3 at 2.8 GHz. It is seen that the tangential electrical field at $t = 0$ is distributed mainly across the vertical slot, and is along the $-y$ direction. Analogously,

at $t = \mathrm{T}/4$, the tangential electrical field is mainly distributed normal to the open-edge of the patch along the $-x$ direction. The E-field distributions at $t = \mathrm{T}/2$ and $t = 3\mathrm{T}/4$ are along the $+y$ and $+x$ directions, respectively. It is clear that the tangential electrical field exhibits a sequential delay in a clockwise direction in one period. Consequently, the antenna radiates a left-handed circular polarization (LHCP) beam. On the other hand, note that when the antenna is fed from the right side and terminated on the left side, a right-handed circular polarization (RHCP) beam is radiated.

7.1.3 Simulated and Measured Results

Table 7.1: Optimized Values for the CP LWA Design Parameters

Parameter	W_s	W_m	L_{st}	W_{st}	L_{sl}	W_{sl}	P
Value (mm)	80	45	36	8	30	5	43.5
Parameter	S	T	d_1	d_2	L_t	W_a	W_b
Value (mm)	2.9	9.5	1.6	3	20	7.5	30

The optimized design parameters of the CP LWA are listed in Table 7.1. Note that the parameters W_a, W_b, W_m, and L_t are mainly responsible for the antenna's impedance matching, and the parameters L_{st}, W_{st}, L_{sl}, W_{sl} and d_2 determine its AR performance. One needs to tune appropriate parameters in the optimization process. This design was fabricated, and the resulting prototype is shown in the bottom inset of Fig. 7.1. The measured and simulated S-parameters are compared in Fig. 7.4. The simulated $|S_{11}| \leq -10$dB frequency bandwidth ranges from 2.54 to 3.37 GHz, while the measured one is from 2.47 to 3.39 GHz. While they are in good agreement, the small discrepancies between the measured and simulated values are associated with small fabrication inaccuracies. Within the measured bandwidth, 3.025 GHz is the broadside radiation frequency. The

observed peak in the $|S_{11}|$, -10.7 dB, occurs at 3.02 GHz, near this transition frequency. The measured and simulated $|S_{21}|$ values also agree very well. Within the measured bandwidth, the measured $|S_{21}|$ values decrease as the frequency increases, ranging from -7.5 to -24.0 dB.

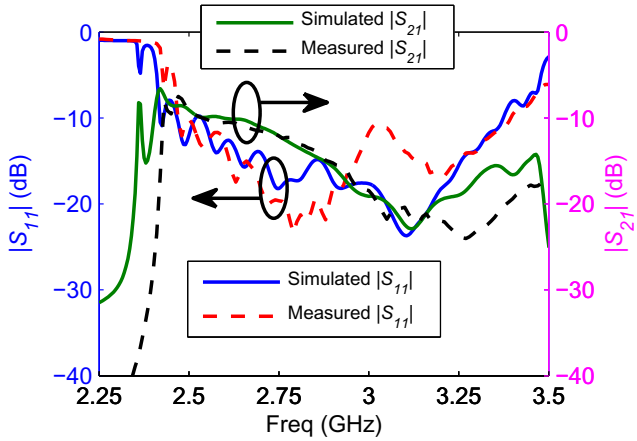

Figure 7.4: Measured and simulated S-parameters of the optimized CP LWA.

Fig. 7.5 shows the simulated co-polarization (LHCP) and cross-polarization (RHCP) radiation patterns at five frequencies within the simulated -10 dB impedance bandwidth. As the dispersion diagram in Fig. 7.2 indicates, the CP LWA radiates a backward beam at lower frequencies. At 2.65 GHz the beam points into the $-34°$ direction and then into the $-18°$ direction at 2.8 GHz. The main beam points at the broadside direction at 2.955 GHz. With a further increase in the frequency, the main beam direction moves towards the forward quadrant, e.g., it points into $+14°$ and $+32°$ at 3.1 and 3.25 GHz, respectively. Fig. 7.6(a), (b), and (c) show, respectively, the 3-D realized gain patterns at 2.65, 2.955, and 3.25 GHz. It is clearly seen that the CP LWA radiates a fan beam at each frequency that has a narrow beamwidth with respect to the yz-plane and a wide beamwidth with respect to the zx-plane.

The antenna far-field radiation patterns were measured using the Satimo multi-probe spherical near-field system StarLab-18 located at Xiamen University, China. The mea-

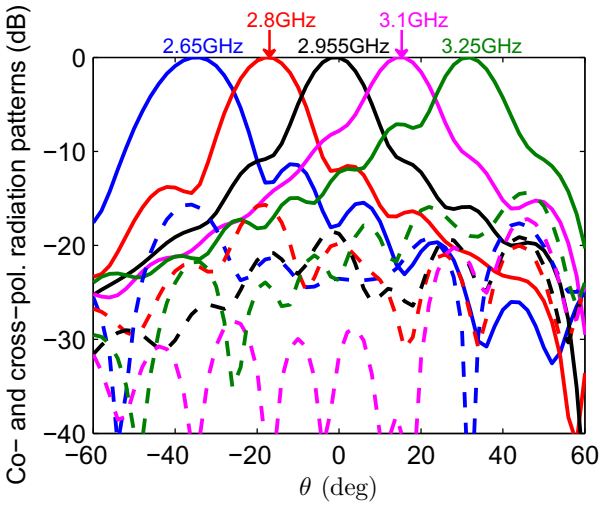

Figure 7.5: Simulated radiation patterns of the CP LWA at five frequencies within its bandwidth. Solid line: Co-polarization (LHCP); Dash line: Cross-polarization (RHCP).

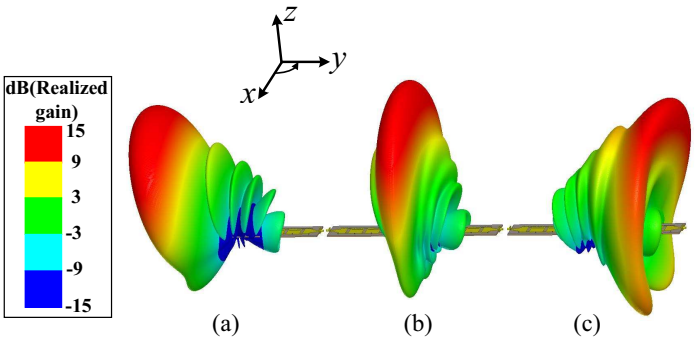

Figure 7.6: Simulated 3-D realized gain patterns of the CP LWA at three frequencies within its operating bandwidth: (a) 2.65, (b) 2.955, and (c) 3.25 GHz.

sured radiation patterns are depicted in Fig. 7.7 at five frequencies within the measured −10 dB impedance bandwidth. The measured LHCP beam points into the −34.3°, −17.2°, 0°, +17.2°, and +31.5° directions at 2.7, 2.85, 3.025, 3.2, and 3.35 GHz, respectively. Note that for a given beam direction the measured frequency is slightly higher than its simulated value. This blue shift is consistent for all of the measured patterns. As a consequence, the frequencies at which the measured patterns are reported were selected

to be higher than those simulated in order that the beam directions are nearly the same. In summary, the measured prototype verifies the continuous scanning of the main beam of the CP LWA antenna from the backward to forward directions through broadside.

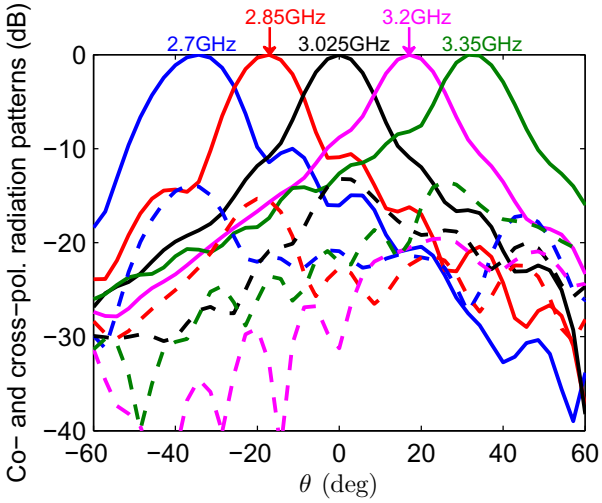

Figure 7.7: Measured radiation patterns of the CP LWA at five frequencies within its bandwidth. Solid line: Co-polarization (LHCP); Dash line: Cross-polarization (RHCP).

Fig. 7.8 shows the simulated and measured realized gain values and the axial ratio (AR) values as functions of the source frequency. The AR values were obtained at the main beam angle for the corresponding frequency. The simulated AR $\leq$ 3 dB bandwidth is from 2.65 to 3.25 GHz (600 MHz), and the realized gain varies between 11.3 and 13.6 dBic over the same range. The measured frequency band was from 2.75 to 3.35 GHz (600 MHz). The measured realized gain variance is between 10 and 13 dBi, i.e., only a 3 dB gain variance. The measured AR values are below 3 dB except when the frequency is around 3.025 GHz, the transition frequency. The maximum measured AR value was 4.1 dB at 3.0 GHz. It is believed that the already noted $|S_{11}|$ issues associated with the fabrication errors also impacted the AR values. Simulations indicate that the variations in the AR values near the transition frequency are exacerbated by the small power reflections associated with those fabrication inaccuracies. In particular, recall that

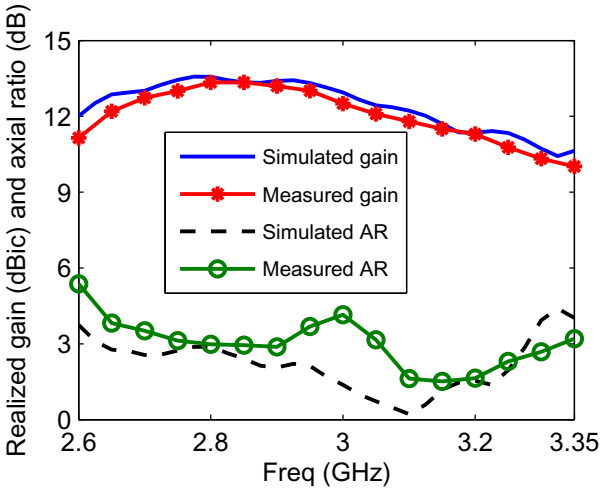

Figure 7.8: Measured and simulated realized gain and axial ratio values of the CP LWA as functions of the source frequency.

realized gain is proportional to the term (1-$|S_{11}|^2$). The differences between the simulated and measured $|S_{11}|$ values at the transition frequency, 3.025 GHz, in Fig. 7.8 lead to negligible changes in this factor. On the other hand, the fabrication errors introduce differences between the corresponding two orthogonal field components that create the CP fields. This perturbation more significantly impacts their balance and, hence, the AR values near the critical transition frequency.

7.2 Frequency-Based Beam Steerable LP LWA

While a CP LWA is a good candidate for the satellite communications, many applications simply require LP performance. It was found that the CP LWA could be modified to obtain just LP fields. A shorted-stub loaded version facilitated the realization of a LP LWA with continuous beam scanning through broadside. The design, simulation, fabrication, and measurement of this antenna are presented. The measured and simulated performance characteristics are in good agreement.

7.2.1 Antenna Configuration and Analysis

Fig. 7.9 shows the developed LP LWA configuration. Since our final goal is to achieve a polarization reconfigurable LWA, the CP LWA was converted to a LP LWA by incorporating a row of shorted stubs. The desired co-polarized component of the electrical field in the YZ plane is E_θ, and its cross-polarized component is E_ϕ. As illustrated, each stub extends directly from the lower edge of the patch towards the lower side of the substrate. Each one is centered with respect to the vertical slot and is shorted to the ground with the indicated shorting via B. Because of the position of the stub, these additional shorting vias are centered with respect to two of the original shorting vias A. The shorting via B has a diameter d_3 and is connected to the lower end of the stub and to the bottom ground plane. The length and width of each stub are L and W, respectively. The entire patch and stub configuration is centered on the top of the substrate. The bottom copper surface of the substrate again acts as the ground plane.

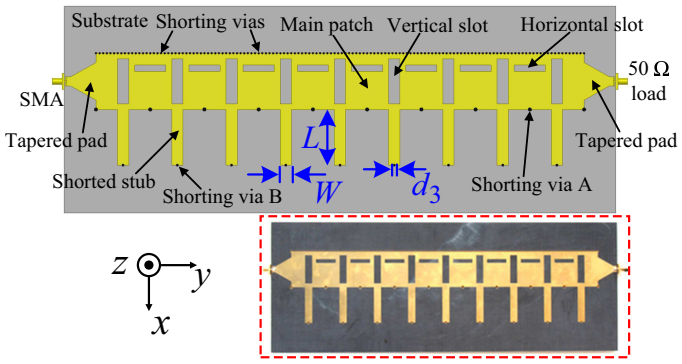

Figure 7.9: Top view of the shorted-stub loaded LP LWA. Photograph of the prototype antenna is shown in the bottom inset.

To explain the LP operating mechanisms of the shorted-stub loaded LP LWA, top views of the electric field just above one unit cell for four time snapshots with a quarter period separation are given in Fig. 7.10 at 2.8 GHz. It is observed that the tangential

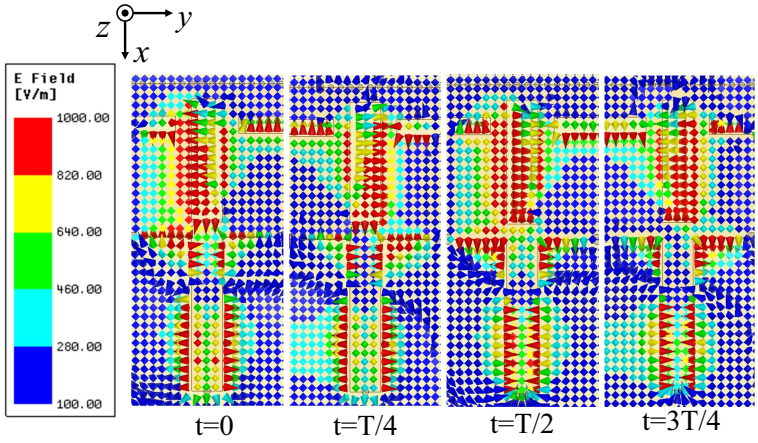

Figure 7.10: Top view of E-field distribution on the surface just above one unit cell of the main patch of the optimized LP LWA at 2.8 GHz for four time snapshots separated by a quarter period.

E-fields are mainly distributed across the vertical and horizontal slots and normal to both edges of the shorted stubs and the bottom edge of the patches. The E-fields on the vertical slots are oriented along the y-direction and again lead to strong magnetic currents along the x-direction [120, 121]. The tangential E-fields are oriented normal to the edges of the shorted stubs introduced in this case, but in opposite directions on opposite sides. Similarly, the electric fields across the horizontal slots are oriented in opposite directions on opposite sides of the vertical ones. Their combination produces two main effects. First, the shorted stubs reduce the strengths of the E-fields along the bottom open-edges of the patches and, thus, the associated y-directed magnetic currents. Second, the horizontal slots again provide fine tuning of the overall y-directed magnetic currents. By optimizing the dimensions of the shorted stubs and the horizontal slots, their contributions to the far-field cross-pol radiation are reduced significantly. Thus, LP far-fields are realized by the effective magnetic currents oriented along the x-directions produced by the vertical slots.

7.2.2 Simulated and Measured Results

The antenna model shown in Fig. 7.9 was simulated and optimized with HFSS. The optimized design parameter values (in millimeters) are the same as those listed in Table 7.1 except: $W_s = 165$, $W_{st} = 9$, and $L_{sl} = 25$. The shorted stub and shorting via B dimensions (in millimeters) are: $L = 45$, $W = 9$, and $d_3 = 2$, respectively. A prototype of this LP LWA was fabricated. A photo of it is also included at the bottom inset of Fig. 7.9.

Fig. 7.11 shows the measured and simulated S-parameters of the optimized LP LWA. The simulated $|S_{11}| \leq -10$ dB bandwidth is from 2.78 to 3.22 GHz (440 MHz). The corresponding measured bandwidth is from 2.77 and 3.3 GHz (530 MHz). The peak $|S_{11}|$ value is -9.5 dB at 3.07 GHz. The measured $|S_{21}|$ values are below -12.6 dB from 2.77 to 3.3 GHz, and they agree well with their simulated values within the -10 dB impedance bandwidth.

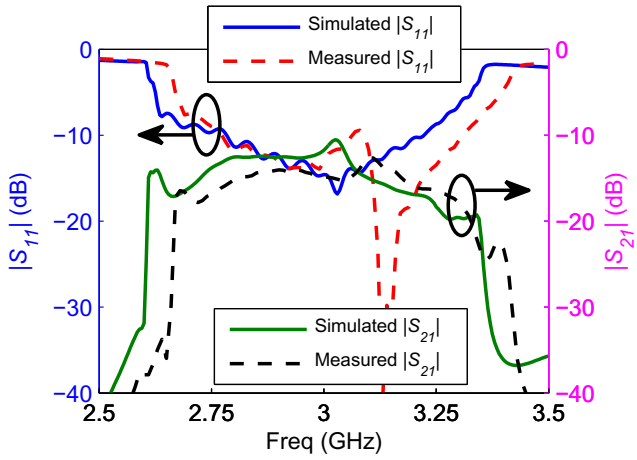

Figure 7.11: Measured and simulated S-parameters of the optimized LP LWA.

Fig. 7.12 shows the simulated co-polarization and cross-polarization radiation patterns for the shorted-stub loaded LP LWA at five frequencies within its impedance bandwidth, and Fig. 7.13 displays the measured ones. Again, a slight blue shift of the frequency-dependent pattern occurs, i.e, the measured co-polarization main beam points into the

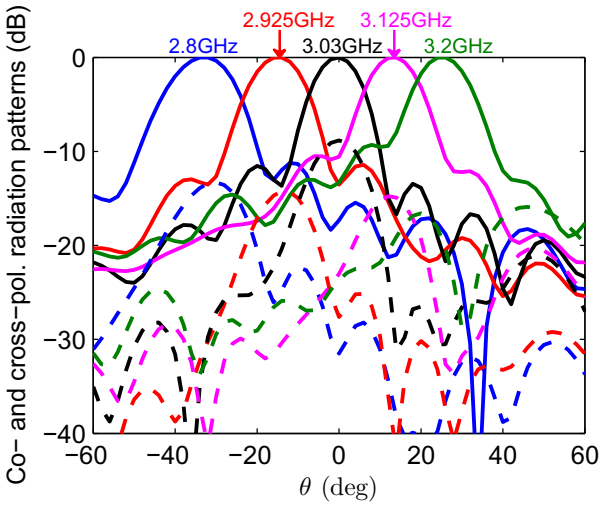

Figure 7.12: Simulated radiation patterns of the LP LWA at five frequencies within its bandwidth. Solid line: Co-polarization; Dash line: Cross-polarization.

$-34.3°$, $-14.3°$, $0°$, $+14.3°$, and $+25.7°$ directions at 2.85, 3.0, 3.1, 3.2, and 3.275 GHz, respectively. On the other hand, the simulated beam angle is $-32°$, $-14°$, $0°$, $+14°$ and $+26°$ at 2.8, 2.925, 3.03, 3.125, and 3.2 GHz, respectively.

Fig. 7.14 shows the simulated and measured peak realized gain and cross polarization values of the LP LWA as functions of the source frequency. It is clear that the measured peak realized gain curve is similar to the simulated one. The measured peak realized gain increases from 12.7 dBi at 2.85 GHz to 13.0 dBi at 3 GHz, and then decreases to 9.55 dBi at 3.25 GHz. It is noted that there is a droop in the measured value at 3.1 GHz, the transition frequency, to 10.6 dBi. From 2.85 to 3.275 GHz, the measured realized gain variance is 3.45 dB. The measured cross polarization level (obtained at the main beam angle at the corresponding frequency) is stable across the operating frequency band and peaks at 3.1 GHz with the value -7.9 dB.

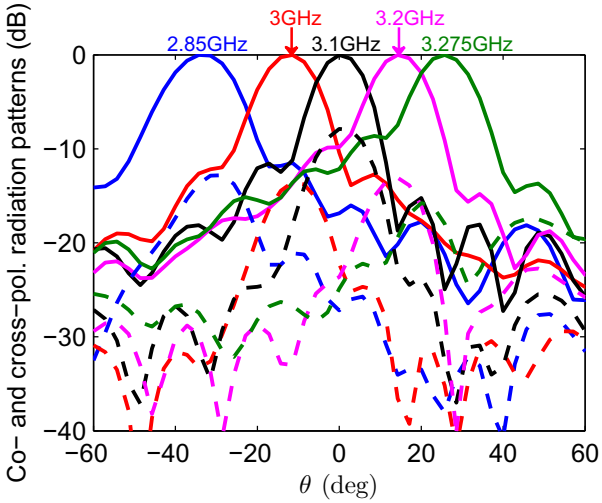

Figure 7.13: Measured radiation patterns of the LP LWA at five frequencies within its bandwidth. Solid line: Co-polarization; Dash line: Cross-polarization.

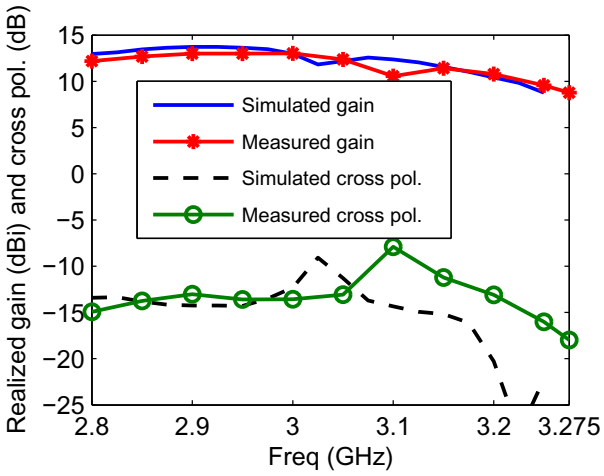

Figure 7.14: Measured and simulated realized gain and cross polarization (cross pol.) values of the LP LWA as functions of the source frequency.

7.3 Polarization-Reconfigurable Frequency-Based Continuous Beam Scanning LWA

To facilitate the development of the desired polarization agile LWA, reconfigurable technology is implemented into the shorted-stub loaded LP LWA structure to switch the polarization between the available CP and LP states. Because the LP LWA was derived from the CP version by introducing the shorted-stubs, switches are introduced between the original main patch and the shorted stubs to obtain the desired polarization reconfigurability. PIN diodes were selected for those switches; the associated biasing arrangements were developed. The ON-OFF states of the PIN diodes connect or disconnect the shorted stubs to the main patch, yielding the desired selectivity between the LP or CP states.

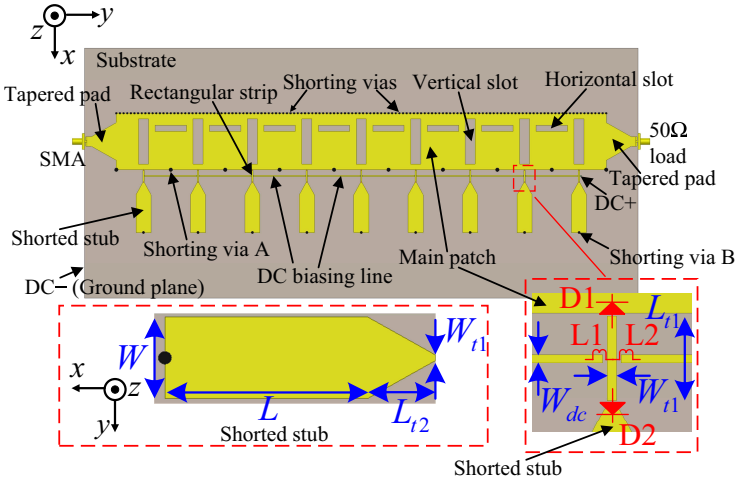

Figure 7.15: Top view of the polarization-reconfigurable LWA. The bottom left inset shows the shorted stubs and the right inset shows the diode placements and biasing arrangements.

The configuration of the polarization-reconfigurable LWA is illustrated in Fig. 7.15. Details of the modified shorted stub design and the diode placements and biasing arrangements are given in the insets. The stubs were modified to accommodate the presence of

the PIN diodes. To connect them to the main patch, the end of the stub nearest to the main patch was tapered to match it to a small rectangular strip whose width matched the much smaller dimensions of the diode. PIN diodes were then introduced to connect the stub to the strip and the strip to the main patch. The PIN-loaded small rectangular strips have the length L_{t1} and the width W_{t1}. The trapezoidal-shaped taper has its bottom width equal to the shorted stub width W and its top width equal to the strip width W_{t1}. Its height is the length of the taper L_{t2}. When the diodes are switched OFF, the CP LWA configuration is attained. It is noted that if the rectangular-shaped stubs were used, a coupling issue between the rectangular-shaped stubs and the main radiating patch arises that will deteriorate the CP state of the polarization-reconfigurable antenna. The trapezoidal-shaped taper structure and the small connecting strips between the main patch and the shorted stubs overcome this coupling issue. In particular, the dimensions of the taper structure and the small strips must be carefully optimized to achieve good performance for both the CP and LP states.

As shown in Fig. 7.15, the two diodes D1 and D2 are aligned in reverse along the x-axis, i.e., the positive polarities of the two diodes are soldered to the two ends of the rectangular strip. One negative polarity end is soldered to the main patch; the other one is soldered to a shorted stub and, hence, is connected to the ground plane through its via B. The DC biasing lines are printed along the y-axis parallel to the patch edge. They are oriented orthogonal to and are centered in the middle between two of the thin rectangular strips. One can prevent the RF signals from coupling to the DC bias lines and still maintain DC continuity with various approaches. For example, one could utilize meander lines, i.e., distributed inductors, between each end of the DC biasing lines and one of the rectangular strips [122]. However, it was found that they significantly deteriorate the radiation performance. On the other hand, a popular and widely used method is to incorporate chip inductors to block the RF signals. These lumped elements introduce

insignificant effects on the antenna's radiation performance [123]. As depicted in the bottom right inset of Fig. 7.15, inductors L1 and L2 were introduced into the design. They connect the adjacent ends of the DC lines present on both sides of each thin rectangular strip to it. Consequently, only one DC source voltage is needed to bias all of the diodes; and, hence, all the diodes can be switched ON and OFF simultaneously. The DC+ in the upper half of Fig. 7.15 represents the positive polarity of the DC voltage. It is applied to the right most bias line through a small pad that is connected directly to it and to the positive pole of the DC source by a wire passing through a small hole drilled through the substrate and the ground plane. The DC− is the negative polarity of DC voltage, which is connected directly to the ground plane. Thus, the DC circuit for biasing the diodes incorporated into this polarization-reconfigurable LWA is simple and effective.

The dimensions of the biasing circuits, including the tapered shorted stubs, were optimized to achieve good radiation and matching performance in both the LP and CP states. The parameter values (in millimeters) of the LP LWA design that had to be modified are: $W_s = 200$, $W_{st} = 8$, $L = 30$, and $W = 12$. The values for the design parameters (in millimeters) of the thin rectangular lines connecting the main patch and the shorted stubs are: $L_{t1} = 9.2$, $W_{t1} = 1$, $L_{t2} = 10$, $W_{dc} = 0.8$.

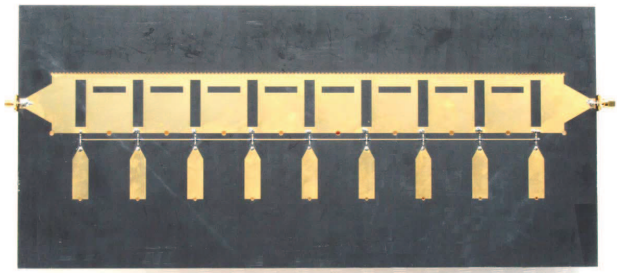

Figure 7.16: Photograph of the fabricated polarization-reconfigurable LWA prototype.

This optimized design was fabricated and the prototype polarization-reconfigurable LWA is shown in Fig. 7.16. All of the diodes used for this prototype were the Bar50-

02L PIN diodes produced by Infineon Technologies with a 0403 surface mount packaging. According to its datasheet, this diode is equivalent to a resistance of 4 Ω in its ON state and to a parallel circuit with a capacitance of 0.07 pF and a resistance of 5 KΩ in its OFF state. Coilcraft chip inductors 0402HP-30NX_EU (30 nH) with a self-resonant frequency at 2.9 GHz were also used. The biasing voltage was provided by a 1.5V dry battery.

7.3.1 Polarization-Reconfigurable LWA Working in Its CP State

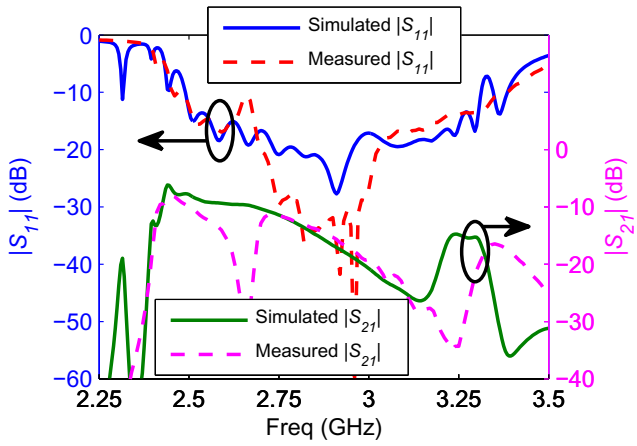

Figure 7.17: Measured and simulated S-parameters of the optimized polarization reconfigurable LWA operating in its CP state.

When all of the diodes are switched OFF, i.e., there is no voltage applied between DC+ and DC−, the shorted stubs are disconnected from the main patch; and, hence, CP beams are radiated. The measured and simulated S-parameters are shown in Fig. 7.17. The simulated $|S_{11}| \leq -10$ dB frequency bandwidth is from 2.5 to 3.3 GHz (800 MHz), while the measured one is from 2.48 to 3.38 GHz (900 MHz). Note that a higher than predicted $|S_{11}|$ value occurs at 2.66 GHz. Additional simulations and measurements have determined that it is caused by either component tolerances or soldering effects associated with the PIN diodes and inductors. Furthermore, the measured $|S_{21}|$ is below −9.2 dB

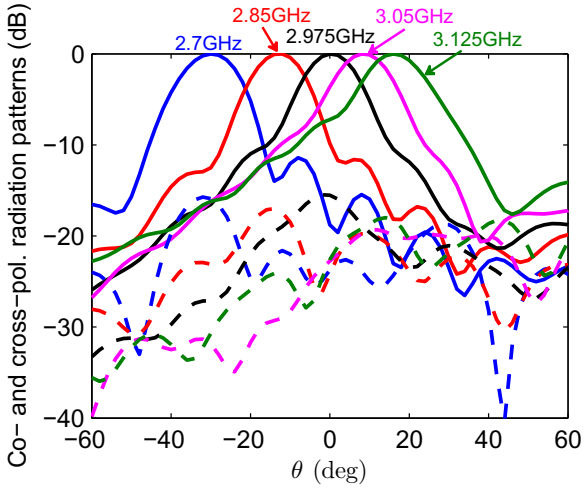

Figure 7.18: Simulated radiation patterns of the optimized polarization-reconfigurable LWA at five frequencies within its CP bandwidth. Solid line: Co-polarization (LHCP); Dash line: Cross-polarization (RHCP).

throughout this measured bandwidth.

Figs. 7.18 and 7.19 show the simulated and measured radiation patterns of the optimized polarization-reconfigurable LWA at five frequencies within its CP bandwidth, respectively. The simulated LHCP beam scanning angle is $-30°$, $-12°$, $0°$, $+8°$, and $+16°$ at 2.7, 2.85, 2.975, 3.05, and 3.125 GHz, respectively. The measured result is $-31.5°$, $-14.3°$, $0°$, $+11.4°$, and $+17.1°$ at at 2.75, 2.9, 3.05, 3.15, and 3.2 GHz, respectively. Figs. 7.20 and 7.21 show, respectively, the simulated and measured AR values as functions of the observation angle at five operating frequencies. One finds in Fig. 7.20 that at the transition frequency (2.975 GHz), the simulated AR ≤ 3 beamwidth is from $-2°$ to $+8°$, i.e., $10°$. For other frequencies, it is much wider, i.e., more than $25°$. On the other hand, the beamwidths for the measured AR ≤ 3 values in Fig. 7.21 are wider than $20°$ at those five operating frequencies. Fig. 7.22 shows the simulated and measured realized gain and AR values as functions of the source frequency from 2.7 to 3.2 GHz. The measured AR values are all below 3.0 dB within this entire frequency band (500 MHz), while the

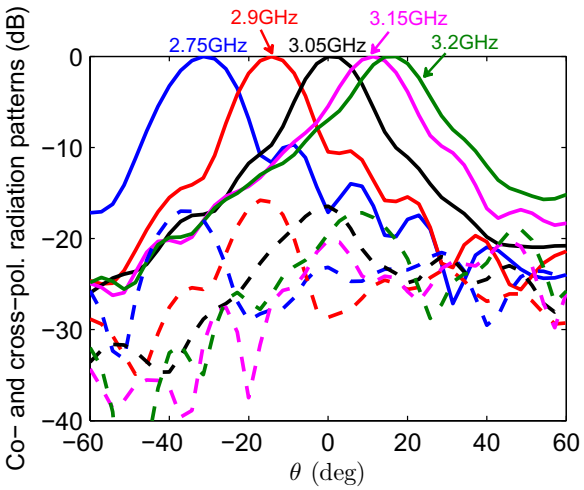

Figure 7.19: Measured radiation patterns of the optimized polarization-reconfigurable LWA at five frequencies within its CP bandwidth. Solid line: Co-polarization (LHCP); Dash line: Cross-polarization (RHCP).

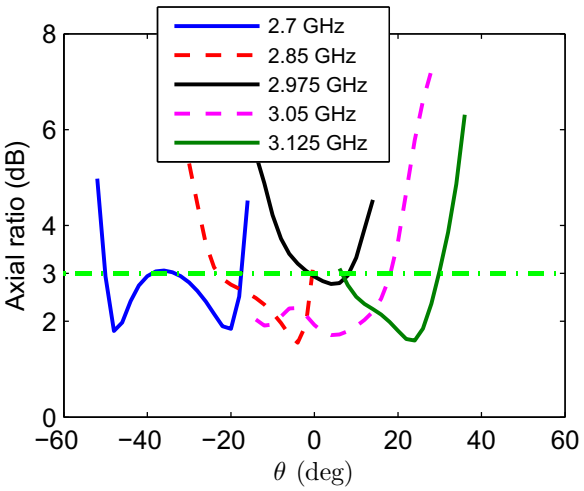

Figure 7.20: Simulated AR values as functions of the observation angle at five operating frequencies for the optimized polarization-reconfigurable LWA in its CP state.

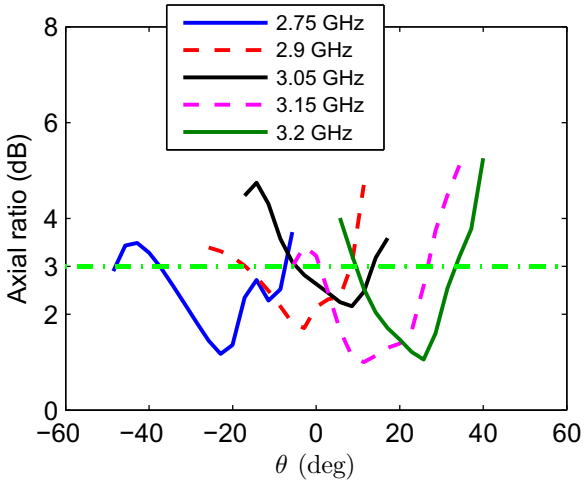

Figure 7.21: Measured AR values as functions of the observation angle at five operating frequencies for the optimized polarization-reconfigurable LWA in its CP state.

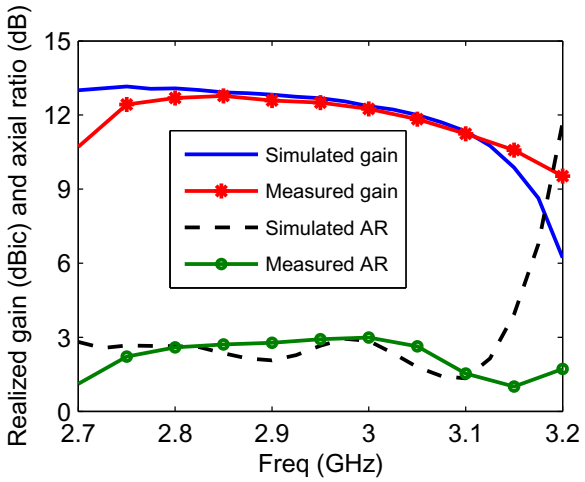

Figure 7.22: Measured and simulated realized gain and axial ratio values of the optimized polarization-reconfigurable LWA operating in its CP state as functions of the source frequency.

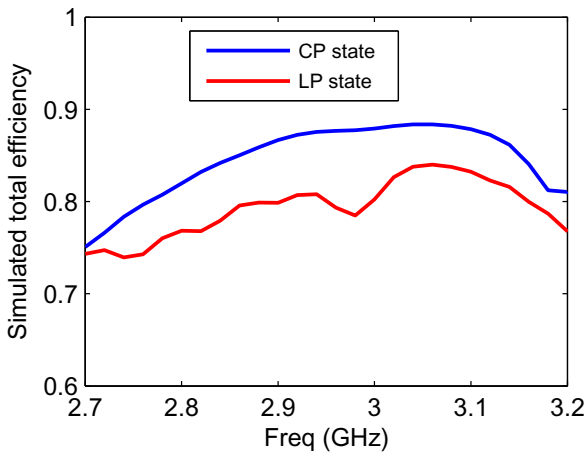

Figure 7.23: Simulated total efficiency of the optimized polarization-reconfigurable LWA operating in its CP and LP states.

simulated AR $\leq$ 3 dB bandwidth is from 2.7 to 3.13 GHz (430 MHz). The measured AR values are slightly higher than their simulated ones. This difference is again correlated with the fabrication inaccuracies. They lead to small changes in the power radiated by the orthogonal field components and, hence, impact the AR outcomes. The measured gain values are within the range 9.5 (at 3.2 GHz) to 12.8 (at 2.85 GHz) dBic. The simulated realized gain values vary between 10.7 and 13.15 dBic over the CP bandwidth. The measured and simulated results are observed to be in reasonable agreement from 2.75 to 3.15 GHz (400 MHz). The simulated total efficiency of the polarization-reconfigurable LWA in its CP state is shown in Fig. 7.23. It varies from 75% and 88% within the frequency band between 2.7 and 3.2 GHz.

7.3.2 Polarization-Reconfigurable LWA Working in Its LP State

When the DC voltage is applied to the bias lines, all of the diodes are switched ON. The polarization-reconfigurable LWA is then in its LP state. Fig. 7.24 shows the measured and simulated S-parameters versus the source frequency for the polarization-reconfigurable

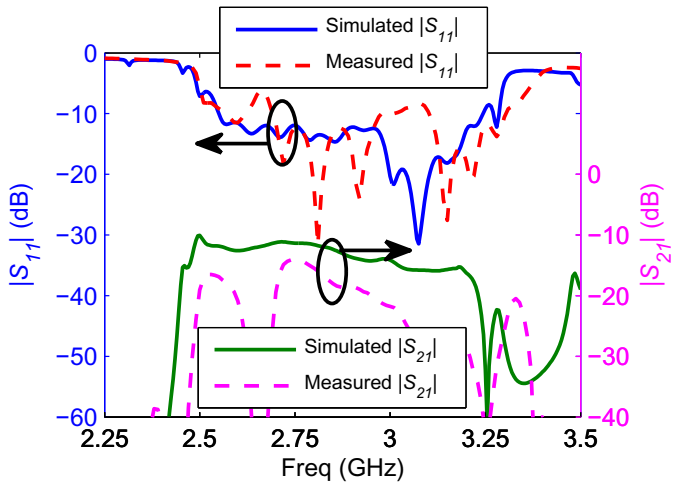

Figure 7.24: Measured and simulated S-parameters of the optimized polarization reconfigurable LWA operating in its LP state.

LWA working in its LP state. The measured $|S_{11}|$ values are below -10 dB from 2.7 to 3.3 GHz (600 MHz), except very near to the transition point (i.e., -9.0 dB at 3.05 GHz). The simulated $|S_{11}| \leq -10$ dB frequency bandwidth is from 2.56 to 3.24 GHz (680 MHz). Additional simulations and measurements have determined that the higher than predicted $|S_{11}|$ values around the transition point result are caused by fabrication inaccuracies. The measured and simulated $|S_{21}|$ values are also shown in Fig. 7.24. The measured $|S_{21}|$ values are less than -14.0 dB (at 2.75 GHz) over the entire LP frequency bandwidth. The measured S-parameters agree reasonably well with their simulated values. The simultaneous low $|S_{11}|$ and $|S_{21}|$ values indicate good radiation performance.

Fig. 7.25 shows the simulated co-polarization (LHCP) and cross-polarization (RHCP) patterns of the polarization-reconfigurable LWA for five frequencies within its LP state bandwidth. The simulated LHCP main beam directions are $-36°$, $-16°$, $0°$, $+14°$, and $+24°$ at 2.7, 2.85, 2.985, 3.075, and 3.15 GHz, respectively. Thus, it is verified that the main beam scans from backwards to forwards through broadside with increasing frequency. The measured co-polarization (LHCP) and cross-polarization (RHCP) patterns are shown

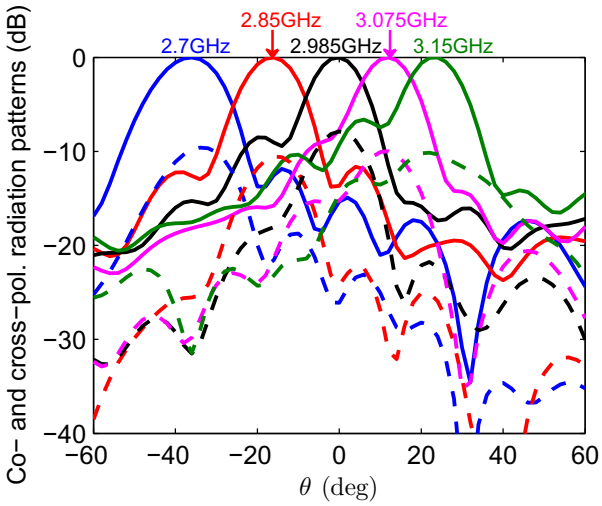

Figure 7.25: Simulated radiation patterns of the optimized polarization-reconfigurable LWA at five frequencies within its LP bandwidth. Solid line: Co-polarization; Dash line: Cross-polarization.

in Fig. 7.26. The main beam directions are −34.3°, −17.1°, 0°, +14.3°, and +20° at 2.75, 2.9, 3.05, 3.15, and 3.2125 GHz, respectively. The measured scanning range agrees well with the simulated one.

The simulated and measured realized gain and cross polarization values are shown in Fig. 7.27 as functions of the source frequency. The measured realized gain varies between 7.8 (at 3.2125 GHz) and 11.7 (at 2.9 GHz) dBi across the −10-dB bandwidth from 2.75 to 3.2125 GHz (462.5 MHz). The simulated realized gain varies between 9.0 (at 3.15 GHz) and 13.0 (at 2.85 GHz) dBi over the frequency band from 2.7 to 3.15 GHz (450 MHz). The measure realized gain values are lower than the simulated one. This outcome is consistent with the fact that the measured radiation patterns shown in Fig. 7.26 have wider half-power beamwidths than their simulated ones. The measured cross polarization levels over the LP frequency band 2.75 to 3.2125 GHz (463.5 MHz) range from −9.5 (at 3.05 GHz) to −6.0 (at 2.75 GHz) dB. The corresponding simulated values range from −11.0 (at 2.875 GHz) to −8.0 (at 3 GHz) dB over the frequency band from 2.7 to 3.15 GHz (450 MHz).

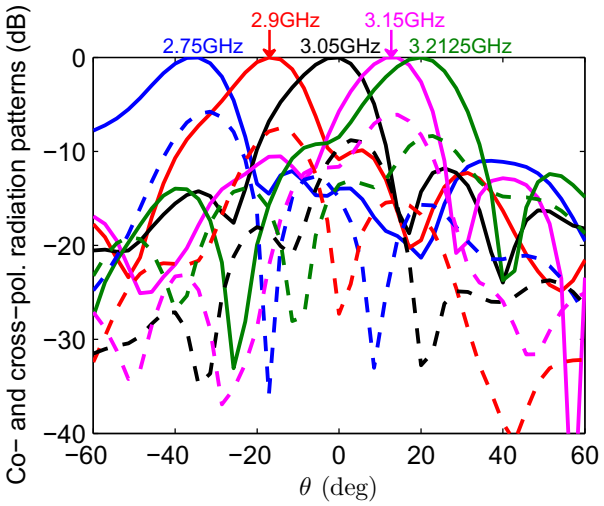

Figure 7.26: Measured radiation patterns of the optimized polarization-reconfigurable LWA at five frequencies within its LP bandwidth. Solid line: Co-polarization; Dash line: Cross-polarization.

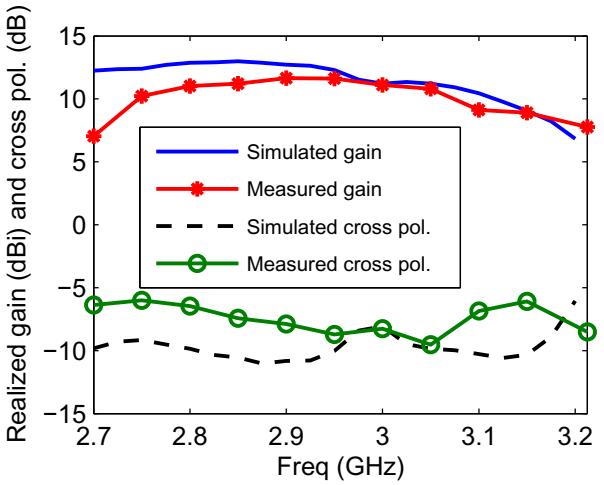

Figure 7.27: Measured and simulated realized gain and cross polarization (cross pol.) values of the optimized polarization-reconfigurable LWA operating in its LP state as functions of the source frequency.

In comparison with their simulated values, the measured lower realized gain and higher cross polarization levels arise from inconsistent diode performance (all of the PIN diodes

are switched ON for this LP state), as well as from fabrication and assembly errors. It is observed that the cross-polarization levels of the polarization-reconfigurable LWA in its LP state are higher than those of the fixed LP LWA. One could achieve similar cross-pol levels in its LP state, but at a cost of a deterioration in its CP performance. The cross-pol increase arises from the presence of the DC bias lines required to control the diode states. The simulated total efficiency of the polarization-reconfigurable LWA in its CP state is also shown in Fig. 7.23. It varies from 74% and 84% within the frequency band between 2.7 and 3.2 GHz.

7.4 Conclusion

A polarization-reconfigurable, frequency-based beam scanning LWA was developed in this chapter. It was demonstrated that scanning from the backward to the forward directions is continuous through broadside and that the antenna can be switched between its LP and CP states. This final optimized system was realized from two other reported antennas. Both a slot-loaded SIW-based CP LWA and a shorted-stub loaded modification of it to obtain a LP LWA were also designed, simulated, fabricated, and measured. It was shown that the main beam of both of these non-reconfigurable antennas could also be scanned from the backward to the forward directions through broadside.

The prototypes of all three antennas verified their simulated performance characteristics. The CP LWA beam was scanned continuously from $-28.6°$ to $+31.5°$ with a 3 dB gain variation. The LP LWA beam was scanned continuously from $-34.3°$ to $+25.7°$ with a 3.45 dB gain variation. The main beam of the polarization-reconfigurable LWA was scanned continuously from $-31.5°$ to $+17.1°$ with a 3.3 dB gain variation in its CP state and from $-34.3°$ to $+20°$ with a 3.9 dB gain variation in its LP state. The measured performance characteristics of all three antennas were shown to be in reasonable agreement

with the simulated values. The optimized reconfigurable LWA has a simple configuration, and its biasing circuits are easily realized.

Chapter 8

Fixed-Frequency Pattern-Reconfigurable Leaky-Wave Antenna

All of the pattern-reconfigurable leaky-wave antennas (LWAs) developed in the Chapters 6 and 7 are frequency-based, i.e., they need to sweep the source frequency to achieve the beam scanning, which may be suitable for wireless sensing platforms. Nevertheless, LWAs with fixed frequency scanning are preferable for future wireless communications. In this chapter, a reconfigurable composite right/left-handed (CRLH) LWA is developed to meet this demand. A variation of a simple single-layer non-reconfigurable frequency-based continuous beam scanning CRLH LWA is considered first. Its dispersion properties are approximately investigated using an equivalent circuit model. It is reported how two groups of varactor diodes can be incorporated into its basic circuit model to electronically control its dispersion behavior. An optimized reconfigurable CRLH LWA with practical DC biasing lines is

then realized from this non-reconfigurable design. Fixed-frequency continuous beam scanning, from backward to forward directions through broadside, is reported over a wide operational frequency band. Simulations predict that the antenna can operate from 4.75 to 5.25 GHz with the main beam being continuously scannable at each frequency point. A prototype was fabricated, assembled, and tested. The measured results confirm its simulated performance characteristics.

8.1 Theory

A classical T-type equivalent circuit of a 1-D CRLH structure is depicted in Fig. 8.1. The inductance L_R and capacitance C_R are naturally associated with a conventional right-handed (RH) transmission line properties. In contrast, the placement of the inductance L_L and capacitance C_L lead to the left-handed (LH) transmission line properties [115, 124, 125]. The inductance L_L in a microstrip version is typically introduced by shorting a via between the line and its ground plane. Similarly, the capacitance C_L is introduced in the transmission line as a series of gaps or as an interdigitated-capacitor.

The phase constant β of this T-type circuit can be expressed as [126]:

$$\beta = \frac{1}{P}\cos^{-1}(1 - \omega^2 L_R C_R - \frac{1}{\omega^2 C_L L_L} + \frac{C_R}{C_L} + \frac{L_R}{L_L}) \tag{8.1}$$

where ω is the angular frequency, i.e., $\omega = 2\pi f$, and P is the length of the unit cell. The cut-off frequencies f_1 and f_2 of this circuit occur when $\beta = 0$ for both the LH and RH dispersion curves. They are calculated as:

$$f_1 = \frac{1}{2\pi\sqrt{L_R C_L}}, \quad \text{and} \quad f_2 = \frac{1}{2\pi\sqrt{L_L C_R}} \tag{8.2}$$

It is now well-known that the open stopband (OSB) can be suppressed if the balanced condition is satisfied, i.e., if $f_1 = f_2$. This, in turn, requires that $L_R/C_R = L_L/C_L$, i.e.,

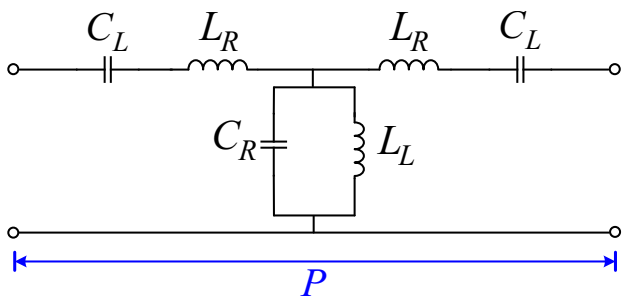

Figure 8.1: T-type equivalent circuit of a 1-D conventional CRLH structure.

the RH and LH impedances are matched [73].

As noted, the main angle, $\theta(f)$, of the beam radiated by a conventional frequency-based LWA at its source frequency f is determined by the relation: [10, 11]:

$$\theta(f) = \sin^{-1}[\beta(f)/k_0(f)] \tag{8.3}$$

It tells us that the main beam angle can be scanned at a fixed frequency if the values of the phase constant β can be varied in an independent manner. To alter the phase constant at a specific frequency, (8.1) indicates that the only choice is to change the circuit parameters if the period length P is fixed, i.e., to change the values of $\widetilde{L}_L, \widetilde{C}_L, \widetilde{L}_R, \widetilde{C}_R$ in some self-consistent manner. This is clarified by expressing the phase constant $\widetilde{\beta}$ at a specific frequency f_0 as:

$$\widetilde{\beta} = \frac{1}{P}\cos^{-1}(1 - \omega_0^2\widetilde{L}_R\widetilde{C}_R - \frac{1}{\omega_0^2\widetilde{C}_L\widetilde{L}_L} + \frac{\widetilde{C}_R}{\widetilde{C}_L} + \frac{\widetilde{L}_R}{\widetilde{L}_L}) \tag{8.4}$$

where $\omega_0 = 2\pi f_0$, and consequently, the main beam angle $\widetilde{\theta}$ as:

$$\widetilde{\theta} = \sin^{-1}(\widetilde{\beta}/k_0(f_0)) \tag{8.5}$$

where $k_0(f_0)$ is the free space wave number at f_0. It is then clear that fixed-frequency beam scanning can occur if some combination of the four CRLH circuit parameters can be controlled to alter the phase constant $\widetilde{\beta}$. We have elected to change those parameters

and, hence, the values of β by introducing a set of switching devices into the circuit, e.g., a set of PIN diodes or varactor diodes, and by controlling them electronically.

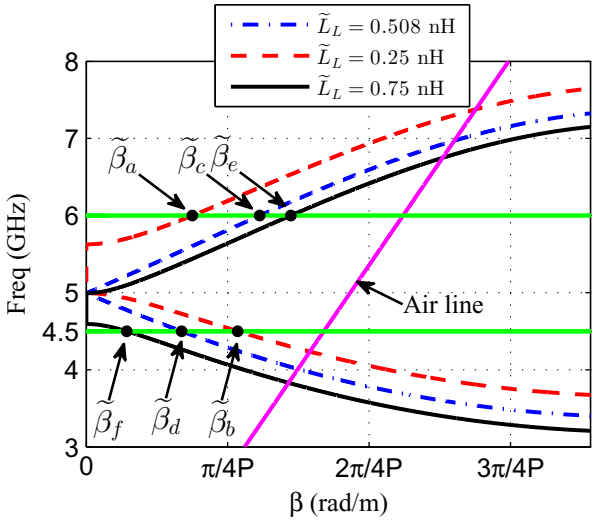

Figure 8.2: Dispersion diagrams for different values of $\widetilde{L}_L$ in the equivalent CRLH circuit.

To illustrate the concept, the values for the circuit parameters and the period length are chosen to be: $\widetilde{L}_R = 1.6$ nH, $\widetilde{C}_R = 2$ pF, $\widetilde{L}_L = 0.508$ nH, $\widetilde{C}_L = 0.635$ pF, and $P = 14$ mm. When the value of a specific parameter is changed, the other values remain fixed in this initial study. Fig. 8.2 shows the dispersion diagrams for different values of $\widetilde{L}_L$. One observes that when $\widetilde{L}_L = 0.508$ nH, a continuous transition at 5.0 GHz is obtained without any gap between the left-handed (LH) and right-handed (RH) portions. Thus, the equivalent CRLH LWA would radiate a broadside beam, i.e., there would be no OSB. On one hand, when $\widetilde{L}_L$ is reduced from 0.508 to 0.25 nH, most of both the RH and LH portions of the dispersion curves shift up in frequency. On the other, when $\widetilde{L}_L$ increases from 0.508 to 0.75 nH, most of both shift down. However, notice that as that inductance increases (decreases), the cut-off frequency for the LH (RH) portion of the gap remains the same while the gap's upper (lower) cut-off frequency increases (decreases) to 5.6 (4.6) GHz through the frequency translation of the RH (LH) portion.

From these dispersion diagrams, one finds at 6.0 GHz that continuous fixed-frequency beam scanning will occur only in the forward quadrant as the value of $\widetilde{\beta}$ increases from $\widetilde{\beta}_a$ ($\widetilde{L}_L = 0.25$ nH) to $\widetilde{\beta}_c$ ($\widetilde{L}_L = 0.75$ nH). Similarly, continuous fixed-frequency beam scanning will occur at 4.5 GHz only in the backward quadrant as $\widetilde{\beta}$ increases from $\widetilde{\beta}_f$ ($\widetilde{L}_L = 0.75$ nH) to $\widetilde{\beta}_b$ ($\widetilde{L}_L = 0.25$ nH). It can then be concluded that continuous scanning through broadside cannot occur if only one circuit parameter is changed, e.g., $\widetilde{L}_L$. Consequently, the effects of simultaneously changing two circuit parameters on the dispersion performance must be investigated.

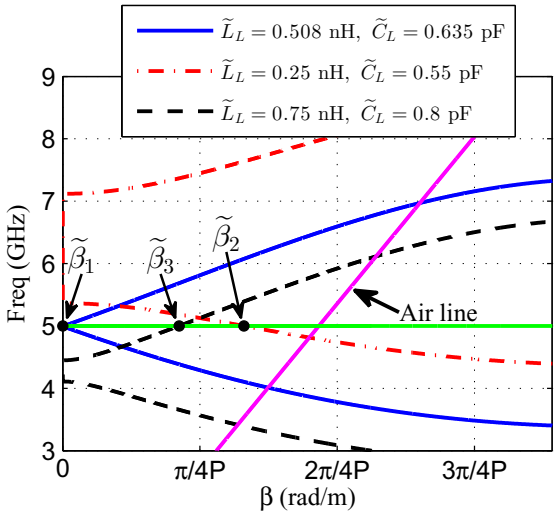

Figure 8.3: Dispersion diagrams for different values of $\widetilde{L}_L$ and $\widetilde{C}_L$ in the equivalent circuit.

Fig. 8.3 shows the different dispersion diagrams when the values of $\widetilde{L}_L$ and $\widetilde{C}_L$ are varied at the same time. We fix the antenna's operating frequency at 5.0 GHz. When $(\widetilde{L}_L, \widetilde{C}_L) = (0.508$ nH, 0.635 pF), $\widetilde{\beta}_1 = 0$ and broadside radiation is realized. On the other hand, when $(\widetilde{L}_L, \widetilde{C}_L)$ decrease separately to (0.25 nH, 0.55 pF), both the LH and RH dispersion curves shift upwards in frequency. Their cut-off frequencies separate, increasing to 5.36 and 7.07 GHz, respectively; and the phase term becomes $\widetilde{\beta}_2$ at 5.0 GHz, realizing a backward main beam direction. On the other hand, when they are increased separately

to (0.75 nH, 0.8 pF), both the LH and RH dispersion curves shift downwards in frequency. Their cut-off frequencies separate, decreasing to 4.45 and 4.11 GHz, respectively; and the phase term becomes $\widetilde{\beta}_3$ at 5.0 GHz, realizing a forward main beam direction. In this manner, it is realized that one can achieve continuous beam scanning from backward to forward through broadside at a fixed frequency by simultaneously changing the values of $\widetilde{L}_L$ and C_L.

Finally, the effects on the dispersion performance were also investigated when three circuit parameters were simultaneously changed. Fig. 8.4 shows the dispersion diagrams when the values of $\widetilde{L}_L$, $\widetilde{C}_L$, and $\widetilde{L}_R$ are varied simultaneously. When $(\widetilde{L}_L, \widetilde{C}_L, \widetilde{L}_R) =$ (0.508 nH, 0.635 pF, 1.6 nH), the beam points in the broadside direction at 5.0 GHz with the phase factor $\widetilde{\beta}_1 = 0$. When all their values are decreased to (0.35 nH, 0.55 pF, 1.3 nH), both the LH and RH dispersion curves shift upwards yielding $\widetilde{\beta}_2$ and a backward beam direction at 5.0 GHz. On the other hand, when $\widetilde{L}_L$ and $\widetilde{C}_L$ are increased to (1.3 nH, 1.1 pF), while the value of $\widetilde{L}_R$ is further reduced to 1.1 nH, one then achieves $\widetilde{\beta}_3$ and a forward beam direction at 5.0 GHz. Thus, one finds that varying three circuit parameters simultaneously, more flexibility in controlling the beam direction is realized. However, it is also recognized that this flexibility would come at the cost of an increased number of the switching elements and the associated complexity of their biasing network.

Several guidelines to change the circuit parameters $(\widetilde{L}_L, \widetilde{C}_L, \widetilde{L}_R, \widetilde{C}_R)$ and, hence, to alter the disperson diagrams in a controllable manner follow from these parameter studies. They are summarized as follows:

1. The values of the phase constant at a specific frequency can be varied by changing one or a combination of the circuit parameters $(\widetilde{L}_L, \widetilde{C}_L, \widetilde{L}_R, \widetilde{C}_R)$. The main beam can then be scanned at a fixed frequency.

2. If only one parameter value is changed while the other three parameters remain fixed, beam scanning at a fixed operating frequency is limited either to the forward

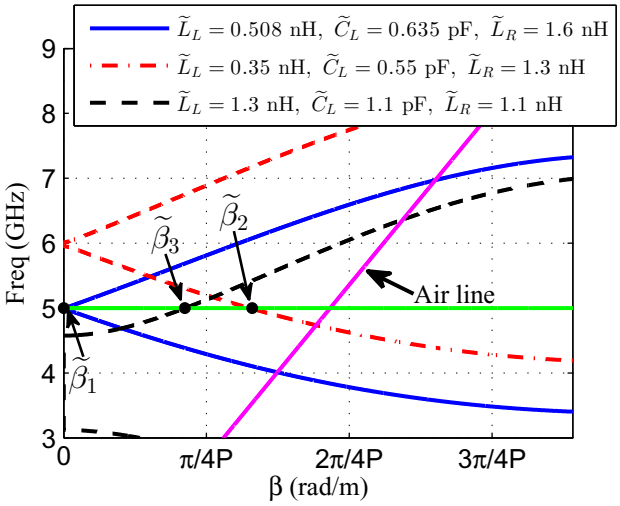

Figure 8.4: Dispersion diagrams for different values of $\widetilde{L}_L$, $\widetilde{C}_L$, and $\widetilde{L}_R$ in the equivalent circuit.

or backward quadrants.

3. When combinations of two to four parameters values are changed simultaneously, the main beam can be continuously scanned at a specific frequency from the backward to the forward quadrant through broadside. There is a tradeoff between flexibility and complexity when the number of tunable parameters increases.

4. Generally, the introduced LH parameters, $\widetilde{L}_L$ and $\widetilde{C}_L$, are easier to modify than their RH ones, $\widetilde{L}_R$ and $\widetilde{C}_R$, because the latter arise naturally from the transmission line.

Based on these guidelines, we elected to control the two LH parameters, $\widetilde{L}_L$ and $\widetilde{C}_L$, to facilitate realizing a fixed-frequency beam scanning LWA.

8.2 Frequency-Based Continuous Beam Scanning CRLH LWA

A simple single-layer frequency-based continuous beam scanning CRLH LWA is developed first. It is shown in Fig. 8.5 and follows from the T-type equivalent circuit shown in Fig. 8.1. A two-layer copper-clad substrate is utilized. It has the following characteristics. It has the relative permittivity (ε_r) 2.2. Its loss tangent ($\tan\delta$) is 0.001. Its height, width, and length are, respectively, 1.575 mm, 33 mm, and 154.5 mm. The main patches, rectangular pads and tapered pads are printed on the top layer. The bottom acts as a solid ground plane. This antenna consists of nine unit cells.

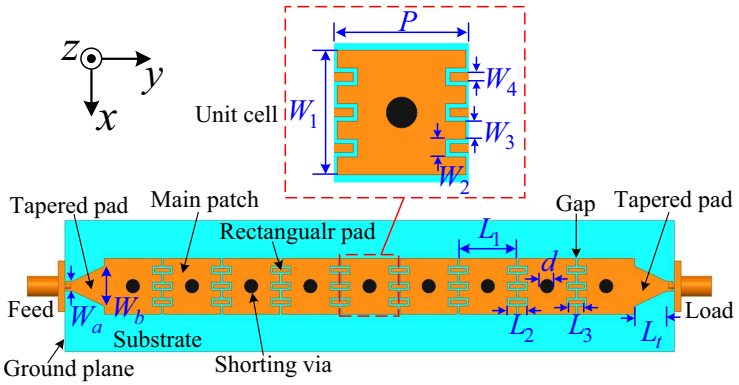

Figure 8.5: Configuration of a single-layer frequency-based continuous beam scanning CRLH LWA. The top inset represents a unit cell of the antenna.

The configuration of each unit cell is shown in the top inset in Fig. 8.5. Its main patch is connected to the solid ground plane with a centrally located shorting via. Meander gaps are etched at both ends of this main patch. Rectangular pads are inserted into the meander gaps. This unit cell evolved naturally from a conventional RH microstrip transmission line. Two widely-used yet simple and effective methods were employed to introduce its LH properties, i.e., the center shorting vias produce the LH inductance and

Table 8.1: Optimized Design Parameter Values (in Millimeters) of the Frequency-Based Continuous Beam Scanning CRLH LWA

Parameters	L_1	L_2	L_3	W_1	W_2	W_3
Values (mm)	14.5	5.1	4.1	14	2	2
Parameters	W_4	P	d	W_a	W_b	L_t
Values (mm)	1	15	3.5	2.5	10	8

the meander gaps yield the LH capacitance.

The length and width of the patch are L_1 and W_1, respectively. The diameter of the shorting vias is d. The dimensions of the meander gap and the rectangular pads are represented by L_2, L_3, W_2, W_3, W_4. The length of the unit cell is P. It represents the length of one period of the LWA. The antenna is fed by a 50 Ω source from the left and terminated in a 50 Ω load on the right. Tapered pads are symmetrically printed at both ends of the antenna. They provide impedance matching of the feed and load SMAs to the central set of unit cells over a wide frequency bandwidth. The dimensions of the tapered pad are W_a, W_b, and L_t.

To obtain the requisite values of the capacitances and inductances to achieve the balanced condition, the preliminary dimensions of the antenna's unit cell were selected and calculated using the microstrip equations for the capacitance and inductance given in [116, 117]. The complete antenna is shown in Fig. 8.5. Its unit cells and matching elements were analysed, simulated, and optimized with the ANSYS HFSS. The optimized values (in millimeters) of the antenna's design parameters are given in Table 8.1. The dispersion diagrams of its unit cell were also obtained and are shown in Fig. 8.6. One can see that a continuous transition between the backward and forward dispersion curves occurs at 4.86 GHz, i.e., there is no bandgap, hence, OSB issue. Therefore, this antenna

can continuously scan the main beam from backward to forward through broadside.

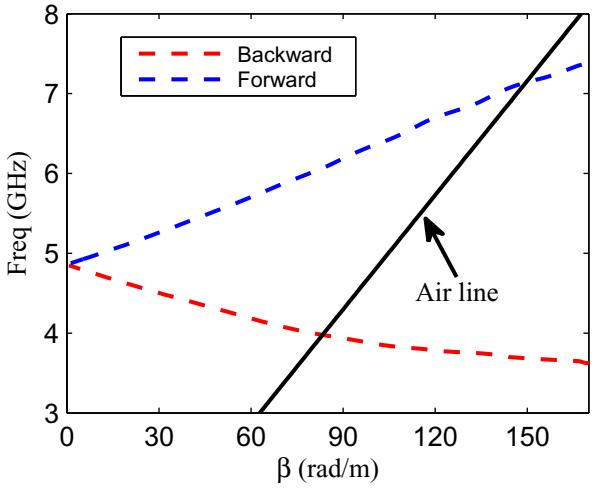

Figure 8.6: Dispersion diagrams of the unit cell of the frequency-based continuous beam scanning CRLH LWA.

Fig. 8.7 shows the corresponding simulated S-parameters as functions of the operating frequency. The simulated $|S_{11}| \leq -10$ dB bandwidth is determined to be 2.01 GHz, from 4.02 to 6.03 GHz. The values actually remain below -8.8 dB down to 4 GHz and below -5.8 dB up to 6.5 GHz. The values of $|S_{21}|$ increase stably with the operating frequency. Their peak value, -5.7 dB, occurs at 6.35 GHz.

The fields radiated by the meander gaps between the adjacent unit cells are the main contributions to the antenna's far-field radiation performance. Thus, the co-polarized component of the electrical field in the YZ plane is E_θ, and its cross-polarized component is E_ϕ. Fig. 8.8 shows the simulated realized gain and beam angle values as functions of the operating frequency. The realized gain exhibits a stable performance with a variation only between 8.2 dBi (at 4 GHz) and 10.8 dBi (at 5.95 GHz). The main beam angle varies from $-58°$ to $+47°$ when the frequency sweeps from 4 to 6.5 GHz. The broadside radiation occurs at 4.9 GHz with a realized gain of 8.8 dBi.

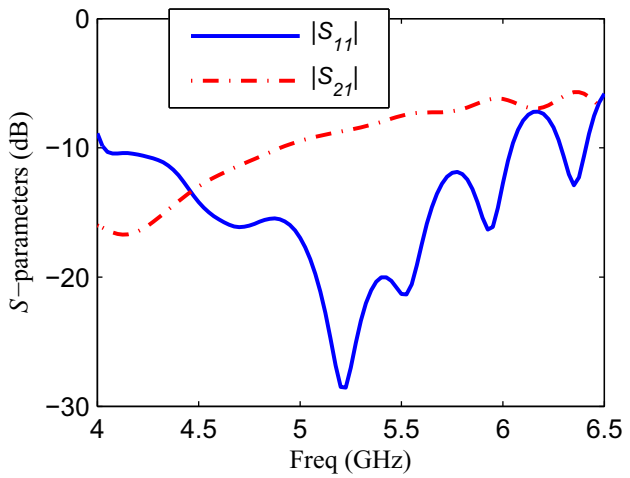

Figure 8.7: Simulated S-parameters of the frequency-based continuous beam scanning CRLH LWA.

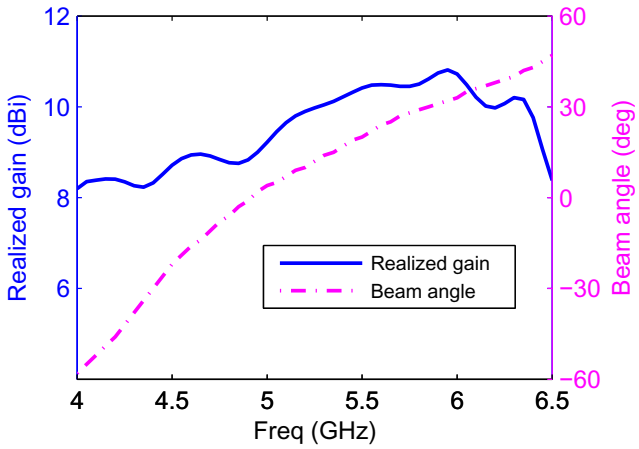

Figure 8.8: Simulated realized gain and beam angle values of the frequency-based continuous beam scanning CRLH LWA.

8.3 Fixed-Frequency Continuous Beam Scanning CRLH LWA

A realizable fixed-frequency beam scanning CRLH LWA emerged from this simple design. Varactor diode switches were introduced to change the CRLH parameters and, hence, to reconfigure the dispersion diagrams for each operating point. A practical layout strategy for the DC biasing lines associated with these switches was also developed.

8.3.1 Antenna Configuration

The two circuit parameters, i.e., $\widetilde{L}_L$ and $\widetilde{C}_L$, were selected for reconfigurability. Two groups of varactor diodes are employed to realize this reconfiguration. Another substrate layer is incorporated into the design for printing their bias lines. This multi-layered configuration is illustrated in Fig. 8.9. It has three metal layers, i.e., the patch layer, ground layer, and biasing layer. The patch and ground layers were, respectively, printed on the top and bottom of the upper substrate. For the lower substrate, all of the metal on its top surface was removed, and the biasing layer was printed on its bottom face. The substrates are the same as the one used in the initial design. The height of the upper substrate and the lower substrate is h_a and h_b, respectively. The other design parameters

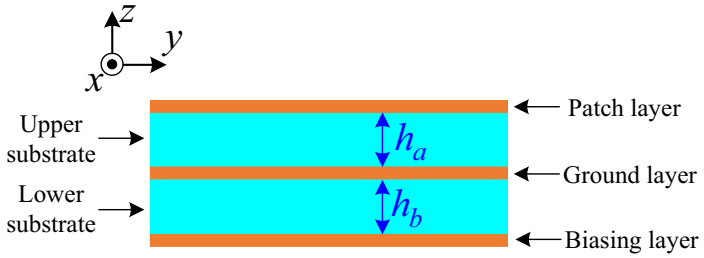

Figure 8.9: Side view (not to scale) of the developed fixed-frequency beam scanning CRLH LWA.

are the same as those in the initial configuration.

Figs. 8.10(a), (b) and (c) show, respectively the patch, ground, and biasing layers. The patches and rectangular pads in the meander gaps of the unit cells, traces that connect the rectangular pads between each unit cell, and the source and termination feedlines with their shorted-stubs are printed on the patch layer, the upper surface of the antenna. One group of the varactor diodes, A, is placed between the central rectangular pads and the main patches. Because these meander gaps introduce the left-handed capacitances $\widetilde{C}_L$, this location of the varactor diodes allows reconfiguration of that capacitance. The varactor diodes A are biased through the trace connecting the three rectangular pads in each meander gap. Note that the directions of these A varactor diodes, which are placed

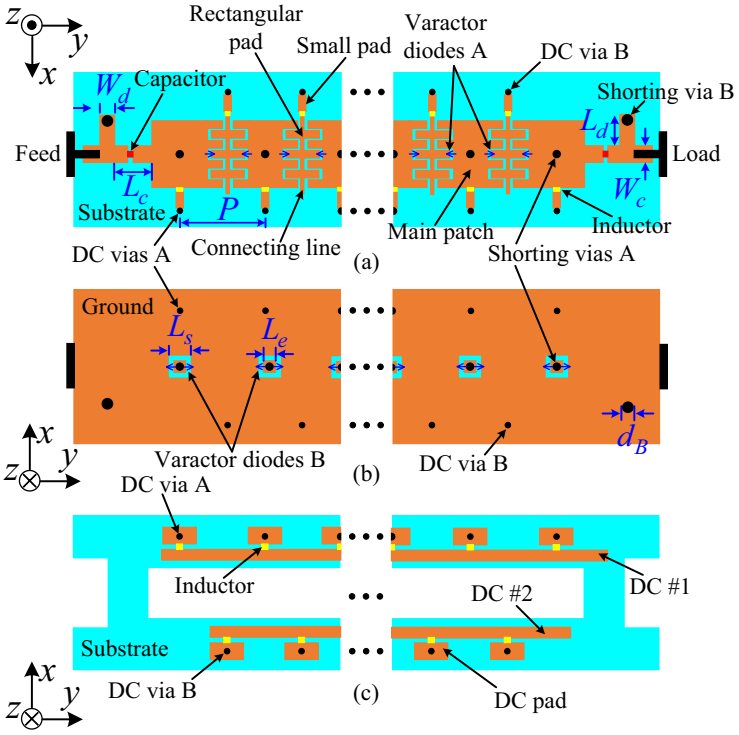

Figure 8.10: The fixed-frequency beam scanning CRLH LWA configuration. (a) Top view of the patch layer. (b) Bottom view of the ground layer. (c) Bottom view of the biasing layer.

at the two ends of each central rectangular pad, are reversed. In this manner, they can be biased simultaneously with a single DC source.

As shown in Fig. 8.10(b), square-ring-shaped slots are etched into the ground plane layer, i.e., the middle metal layer. Smaller square pads are centered in these slots and, consequently, are isolated from the ground plane. The dimensions of the square-ring-shaped slots and the square pads are represented by L_s and L_e. Two varactor diodes B are then reversely soldered between each square pad and the ground plane. Their orientations are opposite to those on the upper layer. Shorting vias A are centrally located with respect to both the main patches on the upper layer and the square pads on the bottom layer. Consequently, the connections between the shorting vias A and the ground plane are controlled by the varactor diodes B. Thus, the left-handed inductance $\widetilde{L}_L$ is introduced when the shorting vias A are turned on. Furthermore, this inductance can be tuned by varying the capacitance of the varactor diodes B. Since the prototype antenna has nine unit cells, eighteen varactor diodes A and twenty varactor diodes B are employed for its frequency and beam reconfiguration.

As shown in Fig. 8.10(c), two groups of DC pads and two long DC biasing lines, DC #1 and DC #2, are printed on the biasing layer. The varactor diodes B are soldered to the ground layer. Because this soldering causes significant bumps, a continuous rectangular slot was cut out of the bottom layer between the DC bias lines in order to have it lie flat on the ground layer. Similar rectangular cuts were made at the ends of this layer to facilitate the placement of the feed and load SMA connectors.

This reconfigurable antenna is again fed by a 50 Ω source from its left side and terminated in 50 Ω load on its right side. However, in contrast to the initial design, tapered termination pads are not employed for matching purposes. The microstrip structures illustrated in Fig. 8.10(a) are used instead. A shorted-stub with a shorting via B is introduced into these terminating lines to facilitate the requisite impedance matching between these

feedlines and the periodic portion of the antenna. The dimensions of the shorted-stub and the shorting via B are denoted by L_c, W_c, L_d, W_d and d_B.

8.3.2 DC Biasing Strategy

For a clear understanding of the DC biasing network, a three-dimensional (3D) view of the entire system is depicted in Fig. 8.11 without the substrates being present. It required a careful design. Two capacitors are located between the feedlines and the first and last main patches to isolate the DC signals while maintaining the continuity of the RF signals. Inductors are employed to choke the RF signal while maintaining the continuity of the DC signal. The positive polarity of each of the varactor diodes A on the patch layer is connected to a main patch. The negative polarity is connected to the rectangular pads in the meander gaps. The positive polarity of each of the varactor diodes B on the ground layer is connected to a small square pad, and then connected to a main patch through a shorting via A. The negative polarity is connected directly to the ground plane. Note that the varactor diodes A and varactor diodes B share the same positive polarity.

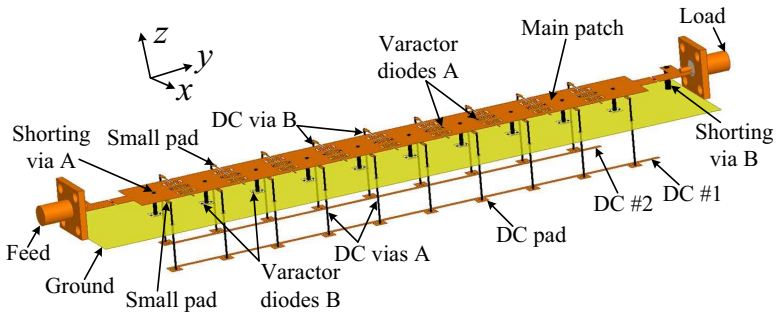

Figure 8.11: A 3D view (not to scale) of the fixed-frequency beam scanning CRLH LWA without the substrates being present.

A set of small rectangular strips are distributed on the patch layer. They are placed close to the outside (horizontal) edges of the main patches. Each one is connected to the main patch of a unit cell through an inductor. Furthermore, these small pads are also

connected to the DC pads on the biasing layer through a DC via A. Each of the latter is connected to the bias line DC #1 through an inductor. Thus, the positive polarity of each varactor diode A and also each varactor diode B is connected to DC #1. Similarly, the connecting lines and, hence, the rectangular pads in the meander slots are all connected to the bias line DC #2 through the small pads on the upper surface, the DC vias B, and the DC pads on the bottom layer. Thus, the negative polarity of each varactor diode A is connected to DC #2. Consequently, when a DC voltage is applied between the bias lines DC #1 and DC #2, all eighteen varactor diodes A can be biased simultaneously with a single DC source. When a DC voltage is applied between the bias lines DC #1 and the ground plane, all twenty varactor diodes B are biased simultaneously. This DC biasing strategy was simple, yet it turned out to be very effective.

8.4 Results and Discussion

8.4.1 Simulated Results

The performance characteristics of the fixed-frequency beam scanning CRLH LWA were optimized with a series of HFSS simulations. The final design parameters are listed in Table 8.2. The simulation results indicated that this fixed-frequency beam scanning LWA

Table 8.2: Design Parameter Values of the Optimized Fixed-Frequency Beam Scanning CRLH LWA

Parameters	L_1	L_2	L_3	W_1	W_2	W_3	W_4	P	d
Values (mm)	13	5	4	14	2	2	1	14	1
Parameters	L_c	W_c	L_d	W_d	L_s	L_e	d_B	h_a	h_b
Values (mm)	9.75	4.5	5	3	3	2	1.5	1.575	0.8

would operate over a 10% frequency bandwidth, i.e., 4.75 to 5.25 GHz, and for each frequency point within the bandwidth, the main beam can be continuously scanned from the backward to forward directions through broadside.

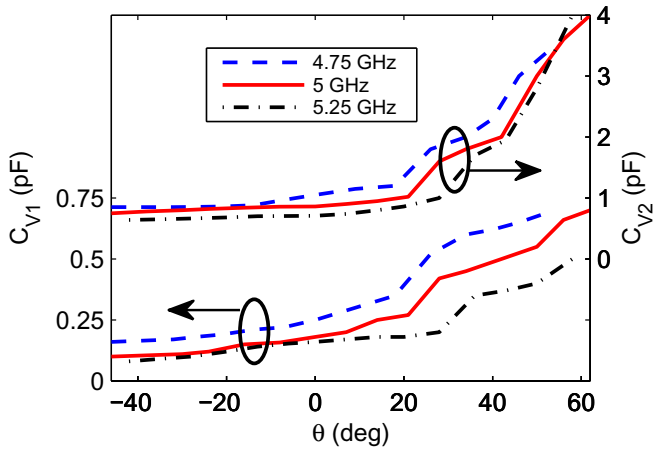

Figure 8.12: Capacitance values of C_{V1} and C_{V2} as functions of the simulated main beam direction at 4.75, 5, and 5.25 GHz.

As illustrations, the simulated performance of the optimized LWA working at 4.75, 5, and 5.25 GHz is shown in Figs. 8.12−8.14. Fig. 8.12 shows the values of the capacitances C_{V1} and C_{V2} as functions of the simulated main beam direction. One notes that with increasing values of (C_{V1}, C_{V2}), the main beam can be continuously scanned from $-46°$ to $+54°$, $-46°$ to $+62°$, and $-42°$ to $+58°$ at 4.75, 5, and 5.25 GHz, respectively. It is noticed that the slopes of these curves are relatively flat for the backward main beam angles and begin to sharply increase for the forward angles. This behavior indicates that the main beam angles in the backward direction are more sensitive to variations in the values of C_{V1} and C_{V2} as compared to the ones in the forward direction. Fig. 8.13 shows the simulated S-parameters as functions of the simulated main beam direction. It is seen that for most main beam angles, the values of $|S_{11}|$ are close to or below -10 dB, and the values of $|S_{21}|$ increase as the main beam scans from backward to forward direction.

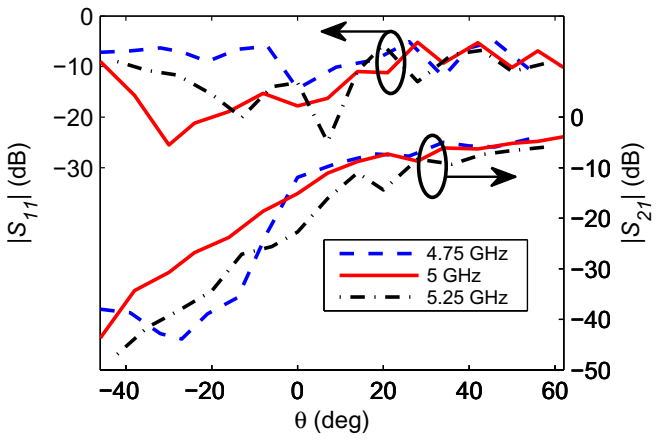

Figure 8.13: S-parameters as functions of the simulated main beam direction at 4.75, 5, and 5.25 GHz.

Simulations also indicate that the radiation efficiency decreases with the increase of the main beam angle. The radiation efficiency is over 90% for the backward main beam angles, and is more than 60% within the whole scanning range. The sidelobe level (SLL) and realized gain as functions of the simulated main beam direction at 4.75, 5, and 5.25 GHz are shown in Fig. 8.14.

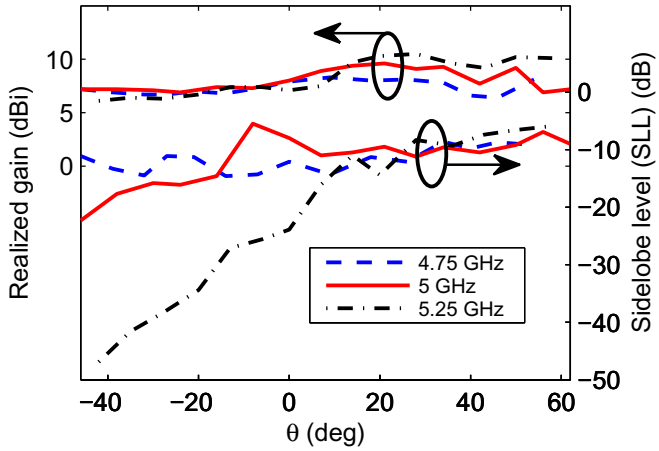

Figure 8.14: Sidelobe level (SLL) and realized gain as functions of the simulated main beam direction at 4.75, 5, and 5.25 GHz.

It is noted that the varactor diodes A and B were treated as lossless for these simulation studies, i.e., they were taken simply to be equivalent to variable capacitors with capacitances C_{V1} and C_{V2}, respectively. No resistance values were included. This choice was made because of the number of diodes and their known manufacturing tolerances. Moreover, discrepancies were expected between their actual performance characteristics and the manufacturer's models, which were specified at a frequency much lower than the antenna's operating frequencies. Nonetheless, it was also anticipated that while the lossless models would predict gain values higher than the actual measured values, the average results of all the diodes would not cause a large difference between the predicted and measured beam angles and radiation patterns. These outcomes were confirmed with the testing of the prototype system.

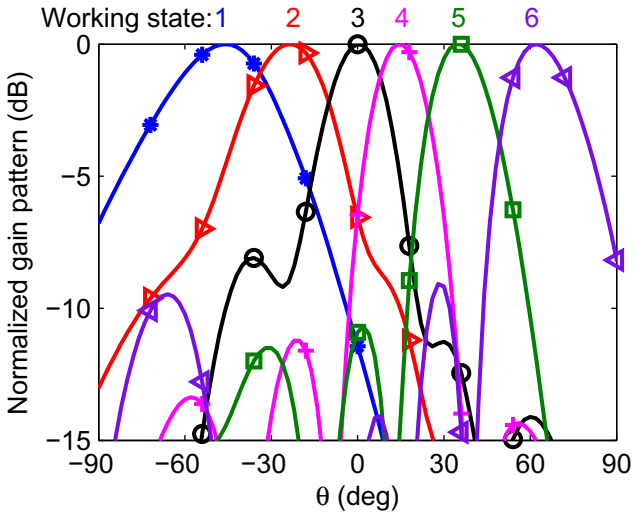

Figure 8.15: Simulated radiation patterns for the antenna's six operating states at 5 GHz.

The simulated radiation patterns for six operating states of the antenna, i.e., States $1-6$, at 5 GHz are shown in Fig. 8.15. It is noted that the half-power beamwidths (HPBWs) of the backward beams are wider than those of the forward beams. For example, the HPBW is 47° for State 1 (C_{V1}, C_{V2}) = (0.1 pF, 0.75 pF) and is 24° for State 5 (C_{V1},

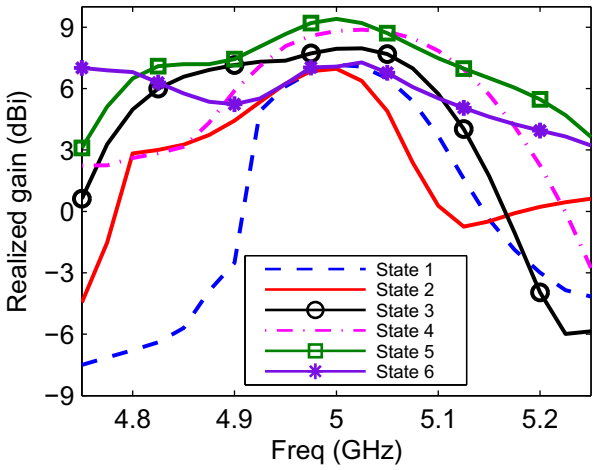

Figure 8.16: Realized gain as a function of the frequency for six operating states of the antenna at 5 GHz.

C_{V2}) = (0.45 pF, 1.8 pF). This feature occurs because the radiation in the first few states (backward pointing) is generated primarily by only the first few unit cells of the LWA while most of them contribute to it for the latter few states (forward pointing). Fig. 8.16 shows the realized gain as a function of the frequency for the above six operating states at 5.0 GHz. One can observe that the antenna's 3-dB operating bandwidth increases as the main beam angle direction increases. This phenomenon is caused by the aforementioned sensitivity of the main beam angles to the values of the capacitances C_{V1} and C_{V2} as illustrated in Fig. 8.12.

8.4.2 Measured Results

This optimized design was fabricated and tested. Figs. 8.17(a) and (b) show photographs of this prototype, respectively, before and after assembly. Two types of commercial varactors were utilized to realize the capacitance tuning. A flip-chip varactor diode MA46H120 produced by MACOM company was used for the varactor diodes A. Its datasheet indicates that when the reverse biasing voltage is varied from 0 to 18 V, the capacitance

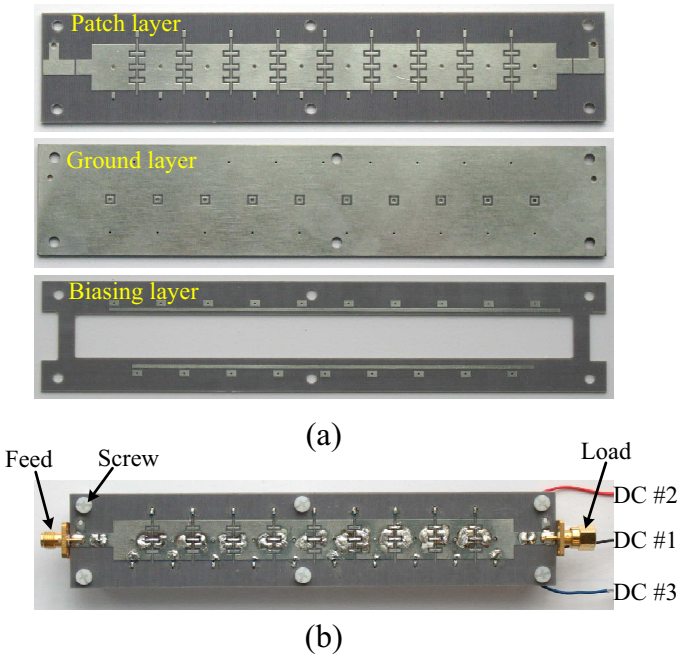

Figure 8.17: Photographs of the fabricated fixed-frequency beam scanning CRLH LWA prototype. (a) Before assembly. (b) After assembly.

value is reduced from 1.3 to 0.15 pF. The associated series resistance is approximately 2 Ω at 0.5 GHz [43]. On the other hand, a silicon abrupt junction varactor diode SMV1405 from Skyworks company was used for the varactor diodes B. Its datasheet indicates that when the reverse biasing voltage is varied from 0 to 30 V, the capacitance value is reduced from 2.67 to 0.63 pF. The associated series resistance is smaller, approximately 0.8 Ω at 0.5 GHz [127]. Unfortunately, these were the lowest loss diodes that we could purchase. Their capacitance ranges fall short of the simulated values and only four (5.25 GHz) and five (5.0 GHz) of the six simulated states could be measured effectively. Every inductor was the surface-mount inductor 0402HP-8N7X (8.7 nH) from Coilcraft. According to its datasheet and confirmed by communications with Coilcraft's technical support, it has a self-resonant frequency at 5.0 GHz and sufficient bandwidth to choke the RF signals within the frequency band of interest while maintaining the DC continuity. Every

DC signal blocking capacitor was selected to be the 600L-0402 capacitor from American Technical Ceramics (ATC) company with a value of 8.2 pF.

Table 8.3: Measured Performance Characteristics of the Fixed-Frequency Beam Scanning CRLH LWA Operating at 5 GHz

Antenna performance	Working states				
	1	2	3	4	5
Voltage V_1 (V)	18	18	10.5	3.1	2.4
Voltage V_2 (V)	16	13	11	2	0.1
S_{11} (dB)	−16.8	−12.9	−10.7	−9.6	−10.0
S_{21} (dB)	−39.9	−34.7	−35.3	−18.3	−20.7
Main beam angle	−37°	−19°	0°	+24°	+32°
Realized gain (dBi)	5.7	4.9	5.4	5.7	4.6

To verify the fixed-frequency beam scanning performance, the far-field radiation characteristics of the prototype were measured using the spherical near-field (SNF) antenna measurement system NSI-700S-50 located at CSIRO, Marsfield, Australia. Due to the limitations of this facility, measurements were only conducted at 5.0 and 5.25 GHz. Table 8.3 presents the measured performance of the fixed-frequency beam scanning CRLH LWA's five working states at 5.0 GHz. All of the measured $|S_{11}|$ values are below −9.6 dB, and those of $|S_{21}|$ are below −18.3 dB. The measured radiation patterns for those five working states are depicted in Fig. 8.18. The measured beam scanning range is from −37° to +32° when (V_1, V_2) is varied from (18V, 16V) to (2.4V, 0.1V). When (V_1, V_2) = (10.5V, 11V), the system is in State 3 and the measured main beam points in the broadside direction with the peak realized gain, 5.4 dBi. Note that the maximum forward beam angle (+32°) of the measured results for State 5 is smaller than the simulated State 6 value, +62°. As discussed, the missing measured state six arises from the limited capacitance

tuning values C_{V2} associated with the SMV1405 varactors, i.e., the required maximum value of C_{V2} is 4.0 pF, whereas the practical maximum value is only 2.67 pF.

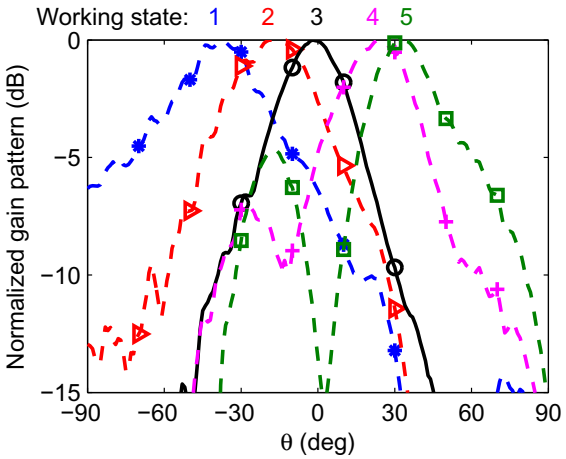

Figure 8.18: Measured radiation patterns for five of the antenna's operating states at 5.0 GHz.

Table 8.4: Measured Performance Characteristics of the Fixed-Frequency Beam Scanning CRLH LWA Operating at 5.25 GHz

Antenna performance	Working states			
	1	2	3	4
Voltage V_1 (V)	18	18	18	3.1
Voltage V_2 (V)	20	16	13	2
S_{11} (dB)	−27.5	−9.6	−15.9	−16.5
S_{21} (dB)	−43.7	−37.1	−45.7	−19.0
Main beam angle	−15°	0°	+13°	+34°
Realized gain (dBi)	5.0	6.4	4.5	6.1

Table 8.4 gives the measured performance of the fixed-frequency beam scanning CRLH LWA in its four working states at 5.25 GHz. The measured $|S_{11}|$ values are below −9.6

dB, and those of $|S_{21}|$ are below -19.0 dB. The measured patterns in those four working states are shown in Fig. 8.19. The measured beam scans from $-15°$ to $+34°$ when (V_1, V_2) is varied from (18V, 20V) to (3.1V, 2V). It points in the broadside in State 2 with the peak realized gain value, 6.4 dBi. The reduced measured scanning range is again due to the limitations of the practical tuning capacitance values of both C_{V1} and C_{V2}.

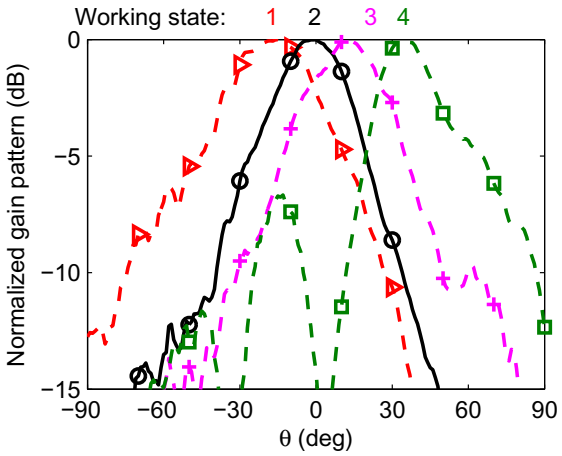

Figure 8.19: Measured radiation patterns for four of the antenna's operating states at 5.25 GHz.

8.4.3 Discussion

One observes that the measured realized gains are lower than their simulated values. The maximum gain difference is around 4.0 dB. It is also noticed that the measured $|S_{21}|$ values are lower than the simulated ones, especially for the forward main beam angles. As anticipated, these outcomes occur because lossless capacitances C_{V1} and C_{V2} were used for the simulations. The resistance associated with each varactor was not included. To improve the future predictive capability associated with the diode models, the simulated realized gain and beam angles were obtained for different loss values of the varactor diodes A and B. The loss was included in the HFSS simulations by incorporating a resistor in

series with each lumped element capacitor representing the varactor diodes A and B. In particular, diode A (B) is represented by a resistor R_{V1} (R_{V2}) in series with the capacitance C_{V1} (C_{V2}). Table 8.5 gives the realized gain values for the six operating states at 5.0 GHz for different combinations of R_{V1} and R_{V2}. The realized gains obtained when (R_{V1}, R_{V2}) = (0 Ω, 0 Ω) denote the lossless case.

Table 8.5: Realized Gain Values for the Six Operating States with Different Values of R_{V1} and R_{V2}

Resistor values (R_{V1}, R_{V2})	Antenna performance	Working states					
		1	2	3	4	5	6
(0 Ω, 0 Ω)	RG (dBi)	7.2	6.9	8.3	9.7	9.3	7.2
	Beam angle	−46°	−24°	0°	+14°	+34°	+62°
(0.5 Ω, 0.2 Ω)	RG (dBi)	6.1	5.8	7.8	8.3	8.0	5.8
	Beam angle	−42°	−22°	4°	+16°	+36°	+62°
(1 Ω, 0.4 Ω)	RG (dBi)	5.7	5.4	7.7	8.1	7.5	5.2
	Beam angle	−42°	−22°	4°	+16°	+36°	+62°
(2 Ω, 0.8 Ω)	RG (dBi)	4.7	4.6	7.1	7.4	6.4	4.5
	Beam angle	−40°	−20°	4°	+16°	+36°	+62°

*RG denotes Realized gain

Table 8.5 indicates that when (R_{V1}, R_{V2}) is varied from (0 Ω, 0 Ω) to (2 Ω, 0.8 Ω), the beam angle shift is less than 6° for all working states and the largest gain variation is around 2.9 dB. Thus, the variations of the resistors confirm both the anticipated non-trivial decreases in the realized gains and the small differences in the main beam angles. For States 1 and 2, the measured realized gains, 5.7 and 4.9 dBi, respectively, suggest that the equivalent (R_{V1}, R_{V2}) values are most likely to be (0.5 Ω, 0.2 Ω). On the

other hand, for States 3 to 5, the measured gains are 5.4, 5.7, and 4.6 dBi, respectively. The equivalent (R_{V1}, R_{V2}) value is most likely (2 Ω, 0.8 Ω). These outcomes confirm the fact that the resistor values of the commercial varactor diodes change with their biasing voltages. Obviously, this feature further complicates any precise modeling effort. Nonetheless, the lossless simulation results proved to be an effective guide to realize the prototype and to anticipate qualitatively its measured performance characteristics.

8.5 Conclusion

A simple CRLH LWA with practical DC biasing lines was demonstrated that achieved fixed-frequency continuous beam scanning in a wide operating band. A theoretical model and numerical simulations predicted that practical fixed wide-angle continuous beam scanning could be realized by simultaneously controlling both the left-handed capacitance and inductance in its CRLH unit cells. A numerically optimized single-layer frequency-based CRLH LWA was developed that scanned the main beam from -58° to $+47^\circ$ with the gain variation of only 2.6 dBi, between 8.2 and 10.8 dBi, when the source frequency was swept from 4 to 6.5 GHz. By developing a means to incorporate a simple yet effective set of DC biasing lines into the design, it was demonstrated that the resulting optimized reconfigurable antenna was able to scan its main beam in an angular range larger than 100° over a wide frequency band from 4.75 to 5.25 GHz.

A prototype was fabricated and tested. The conducted measurements verified the predicted functionality of the antenna. The measured results at 5.0 and 5.25 GHz confirmed that the antenna could continuously scan its main beam through broadside from -37° to $+32^\circ$, and from -15° to $+34^\circ$, respectively. Because of the limitations of the actual capacitance tuning range associated with the commercially-obtained varactor diodes, the measured scanning range was reduced from that predicted by the simulations. Nonethe-

less, the measured results confirmed that a fixed-frequency beam scanning LWA was achieved. Because its unit cell design and DC biasing network are simple, the realized LWA prototype is a promising candidate for future wireless communication systems that require fixed-frequency beam scanning over a large range of frequencies.

Chapter 9

Conclusions and Future Work

9.1 Conclusions

This dissertation focuses on the advancement of the current reconfigurable resonant and leaky-wave antennas technology associated with novel designs or methods to meet the demands for the future wireless systems. Initially, the basis of the resonant antenna and leaky-wave antenna is briefly introduced. Motivated by challenging yet promising research gaps found on reconfigurable resonant and leaky-wave antennas, six research foci are presented and investigated, and the state-of-the-art on each research focus is carefully conducted. Novel antenna designs or methods are developed to fulfill the required functionalities and properties. The advances of the developed antenna systems are summarized as follows:

To realize the multi-linear polarization reconfiguration, initially, a non-reconfigurable center-fed circular patch antenna with a shorting post antenna is developed to excite the fundamental TM_{11} mode with a broadside beam. Accordingly, based on this non-reconfigurable element, four PIN diodes and multiple shorting posts are incorporated to achieve the polarization switching among $\phi = 0°$, $\phi = 45°$, $\phi = 90°$, $\phi = 135°$. The

measured results show that the overlapped $|S_{11}| \leq -10$ dB bandwidth is from 2.33 to 2.5 GHz. The realized gains for all these polarization states vary between 5.3 and 5.9 dBi at 2.45 GHz.

To achieve the pattern reconfigurable resonant antenna with switchable beams, a simple and compact dipole antenna loaded with reconfigurable parasitic striplines and reflecting metal pieces is developed. The antenna was designed, fabricated and assembled. The measured antenna can scan the main beam to five directions, i.e., left endfire, left tilted, broadside, right tilted, and right endfire. The measured realized gains for all these five working modes vary between 5.2 and 6.5 dBi.

To facilitate the combined polarization agility and beam scanning, a cavity-backed proximity-coupled reconfigurable microstrip antenna is developed. By reconfiguring its feed network, three reconfigurable linear polarizations, i.e., $\phi = 0°$, $\phi = 45°$, and $\phi = 90°$, are attained. For each polarization state, the antenna's beam can be scanned to around $+20°$, $0°$, and $-20°$. The realized gains for these nine working states are consistent, varied between 7.2 and 8.1 dBi.

To realize the wide-angle continuous backward-to-forward CP beam scanning with consistent gain, a benzene-ring-shaped slot-loaded CP SIW LWA with PRW vias is developed. An initial I-shaped CP SIW LWA with PRW vias is designed and analysed using equivalent circuit model. Accordingly, the final benzene-ring-shaped slot-loaded SIW LWA with PRW vias is developed and optimized to achieve the desired CP beam-scanning performance. The measured results show that this antenna can scan the main beam from $-42.8°$ to $+54.3°$ with the gain variation between 8 and 11.3 dBic (only 3.3 dBic).

To achieve the polarization reconfigurable continuous backward-to-forward beam scanning LWA, vertical- and horizontal-slots loaded SIW-based CP LWA and a shorted-stub loaded modification of it to obtain a LP LWA were designed, simulated, fabricated, and

measured. Both of these non-reconfigurable antennas can continuously scan the beam from backward to forward. Reconfigurable technology is implemented into the LP LWA structure to switch the polarization between the available CP and LP states. The final reconfigurable system can continuously scan the CP beam from $-28.6°$ to $+31.5°$ with a 3 dB gain variation, and scan the LP beam from $-34.3°$ to $+25.7°$ with a 3.45 dB gain variation.

To realize the fixed-frequency beam scanning LWA over a wide operating band, initially, a single-layer frequency-based CRLH LWA was developed that scanned the main beam from $-58°$ to $+47°$ with the gain variation of only 2.6 dBi, between 8.2 and 10.8 dBi. Based on this frequency-based CRLH LWA, two groups of varactor diodes with simple yet effective set of DC biasing lines have been introduced to scan the main beam in an angular range larger than 100° over a wide frequency band from 4.75 to 5.25 GHz. The antenna prototype was fabricated, and the measured results at 5.0 and 5.25 GHz confirm that the antenna could continuously scan its main beam through broadside from $-37°$ to $+32°$, and from $-15°$ to $+34°$, respectively.

9.2 Future Work

Several advanced antenna designs and methods have been developed in this dissertation, and there are some interesting gaps to work on in the future:

1. In Chapter 5, two-parameter reconfigurable antenna, i.e., combined polarization agility and beam scanning, has been realized. However, with the future demands for multi-functionality and diversity, full reconfigurable antenna, that is frequency-polarization-pattern reconfigurable antenna, with a compact and simple configuration will be attractive.

2. In Chapter 7, frequency-based polarization-reconfigurable beam scanning LWA has

been developed to switch its polarization state between a LP and a CP. Future work could be achieving dual LPs and dual CPs in a single simple feed LWA system.

3. In Chapter 8, fixed-frequency beam scanning LWA has been realized in a wide operating band. To increase the beam scanning coverage, two dimensional fixed-frequency beam scanning LWA is needed.

Chapter 10

Calculation of Phase Constant from T-Type Circuit Parameters

The transmission (ABCD) matrix of a two-port network relates the input voltage and current (V_{in}, I_{in}) to the output (V_{out}, I_{out}) according to [128]:

$$\begin{bmatrix} V_{in} \\ I_{in} \end{bmatrix} = \begin{bmatrix} A & B \\ C & D \end{bmatrix} \times \begin{bmatrix} V_{out} \\ I_{out} \end{bmatrix} \tag{A1}$$

Assume the transmission is lossless, β is the phase constant of this circuit, and P is the length of the unit cell. The relation between the input and out voltages and currents is expressed using phase constant as:

$$\begin{bmatrix} V_{out} \\ I_{out} \end{bmatrix} = \begin{bmatrix} e^{-j\beta P} & 0 \\ 0 & e^{-j\beta P} \end{bmatrix} \times \begin{bmatrix} V_{in} \\ I_{in} \end{bmatrix} \tag{A2}$$

According to (A1) and (A2), one can obtain:

$$\begin{bmatrix} A - e^{j\beta P} & B \\ C & D - e^{j\beta P} \end{bmatrix} \times \begin{bmatrix} V_{out} \\ I_{out} \end{bmatrix} = 0 \tag{A3}$$

If the determinant vanishes, a nontrivial solution for V_{out}, I_{out} exists, and hence

$$\begin{vmatrix} A - e^{j\beta P} & B \\ C & D - e^{j\beta P} \end{vmatrix} = AD - BC + e^{j2\beta P} - e^{j\beta P}(A + D) = 0 \tag{A4}$$

It is known that for a reciprocal network, there is the condition: $AD - BC = 1$. Hence,

$$cos\ \beta P = \frac{A + D}{2} \tag{A5}$$

For the T-type equivalent circuit as shown in Fig. 8.1, the transmission (ABCD) matrix is expressed as:

$$\begin{bmatrix} A & B \\ C & D \end{bmatrix} = \begin{bmatrix} 1 & j\omega L_R + \frac{1}{j\omega C_L} \\ 0 & 1 \end{bmatrix} \times \begin{bmatrix} 1 & 0 \\ \frac{1}{j\omega L_L} + j\omega C_R & 1 \end{bmatrix} \times \begin{bmatrix} 1 & j\omega L_R + \frac{1}{j\omega C_L} \\ 0 & 1 \end{bmatrix} \tag{A6}$$

By solving (A5) and (A6), one can determine the phase constant β using the circuit parameters (L_R, C_R, L_L, and C_L) from the following equation:

$$\beta = \frac{1}{P}\cos^{-1}(1 - \omega^2 L_R C_R - \frac{1}{\omega^2 C_L L_L} + \frac{C_R}{C_L} + \frac{L_R}{L_L}) \tag{A7}$$

Bibliography

[1] J. T. Bernhard, *Reconfigurable Antennas*. Morgan & Claypool, 2007. [Online]. Available: https://ieeexplore.ieee.org/document/6812986

[2] L. Lu, G. Y. Li, A. L. Swindlehurst, A. Ashikhmin, and R. Zhang, "An overview of massive MIMO: benefits and challenges," *IEEE J. Sel. Topics Signal Process.*, vol. 8, no. 5, pp. 742–758, Oct. 2014.

[3] E. G. Larsson, O. Edfors, F. Tufvesson, and T. L. Marzetta, "Massive MIMO for next generation wireless systems," *IEEE Commun. Mag.*, vol. 52, no. 2, pp. 186–195, Feb. 2014.

[4] M. A. Hossain, I. Bahceci, and B. A. Cetiner, "Parasitic layer-based radiation pattern reconfigurable antenna for 5G communications," *IEEE Trans. Antennas Propag.*, vol. 65, no. 12, pp. 6444–6452, Dec. 2017.

[5] L. H. Trinh, F. Ferrero, L. Lizzi, R. Staraj, and J. Ribero, "Reconfigurable antenna for future spectrum reallocations in 5G communications," *IEEE Antennas Wireless Propag. Lett.*, vol. 15, pp. 1297–1300, 2016.

[6] M. Hasan, I. Bahceci, and B. A. Cetiner, "Downlink multi-user MIMO transmission for radiation pattern reconfigurable antenna systems," *IEEE Trans. Wireless Commun.*, vol. 17, no. 10, pp. 6448–6463, Oct. 2018.

[7] R. F. Harrington, *Time-Harmonic Electromagnetic Fields*. McGraw-Hill, 1961.

[8] A. A. Oliner, "Leakage from higher modes on microstrip line with application to antennas," *Radio Science*, vol. 22, no. 6, pp. 907–912, 1987.

[9] D. R. Jackson, C. Caloz, and T. Itoh, "Leaky-wave antennas," *Proc. IEEE*, vol. 100, no. 7, pp. 2194–2206, Jul. 2012.

[10] Y. J. Cheng, W. Hong, K. Wu, and Y. Fan, "Millimeter-wave substrate integrated waveguide long slot leaky-wave antennas and two-dimensional multibeam applications," *IEEE Trans. Antennas Propag.*, vol. 59, no. 1, pp. 40–47, Jan. 2011.

[11] C. Jin and A. Alphones, "Leaky-wave radiation behavior from a double periodic composite right/left-handed substrate integrated waveguide," *IEEE Trans. Antennas Propag.*, vol. 60, no. 4, pp. 1727–1735, Apr. 2012.

[12] C. Jin, A. Alphones, and M. Tsutsumi, "Double periodic composite right/left handed transmission line and its applications to compact leaky-wave antennas," *IEEE Trans. Antennas Propag.*, vol. 59, no. 10, pp. 3679–3686, Oct. 2011.

[13] Z. Li, J. Wang, M. Chen, and Z. Zhang, "New approach of radiation pattern control for leaky-wave antennas based on the effective radiation sections," *IEEE Trans. Antennas Propag.*, vol. 63, no. 7, pp. 2867–2878, Jul. 2015.

[14] A. J. Martinez-Ros, J. L. Gomez-Tornero, and G. Goussetis, "Planar leaky-wave antenna with flexible control of the complex propagation constant," *IEEE Trans. Antennas Propag.*, vol. 60, no. 3, pp. 1625–1630, Mar. 2012.

[15] N. Nguyen-Trong, L. Hall, and C. Fumeaux, "Transmission-line model of nonuniform leaky-wave antennas," *IEEE Trans. Antennas Propag.*, vol. 64, no. 3, pp. 883–893, Mar. 2016.

[16] Z. Li, J. Wang, J. Duan, Z. Zhang, and M. Chen, "Analysis on the radiation property of the bounded modes of periodic leaky-wave structure with finite-length using a hybrid method," *Sci. Rep.*, vol. 6, p. 22917, 2016.

[17] X. Yang, L. Di, Y. Yu, and S. Gao, "Low-profile frequency-scanned antenna based on substrate integrated waveguide," *IEEE Trans. Antennas Propag.*, vol. 65, no. 4, pp. 2051–2056, Apr. 2017.

[18] Y. Geng, J. Wang, Y. Li, Z. Li, M. Chen, and Z. Zhang, "Leaky-wave antenna array with a power-recycling feeding network for radiation efficiency improvement," *IEEE Trans. Antennas Propag.*, vol. 65, no. 5, pp. 2689–2694, May 2017.

[19] D. K. Karmokar, K. P. Esselle, and T. S. Bird, "An array of half-width microstrip leaky-wave antennas radiating on boresight," *IEEE Antennas Wireless Propag. Lett.*, vol. 14, pp. 112–114, 2015.

[20] J. Liu, D. R. Jackson, and Y. Long, "Substrate integrated waveguide (SIW) leaky-wave antenna with transverse slots," *IEEE Trans. Antennas Propag.*, vol. 60, no. 1, pp. 20–29, Jan. 2012.

[21] S. Gao, A. Sambell, and S. S. Zhong, "Polarization-agile antennas," *IEEE Antennas Propag. Mag.*, vol. 48, no. 3, pp. 28–37, Jun. 2006.

[22] P. Y. Qin, Y. J. Guo, and C. Liang, "Effect of antenna polarization diversity on MIMO system capacity," *IEEE Antennas Wireless Propag. Lett.*, vol. 9, pp. 1092–1095, 2010.

[23] C. G. Christodoulou, Y. Tawk, S. A. Lane, and S. R. Erwin, "Reconfigurable antennas for wireless and space applications," *Proc. IEEE*, vol. 100, no. 7, pp. 2250–2261, Jul. 2012.

[24] F. Yang and Y. Rahmat-Samii, "A reconfigurable patch antenna using switchable slots for circular polarization diversity," *IEEE Microw. Wireless Compon. Lett.*, vol. 12, no. 3, pp. 96–98, Mar. 2002.

[25] Y. F. Cao, S. W. Cheung, and T. I. Yuk, "Dual-cap mushroom-like metasurface used in CP reconfigurable monopole antenna for performance enhancement," *IEEE Trans. Antennas Propag.*, vol. 63, no. 12, pp. 5949–5955, Dec. 2015.

[26] H. L. Zhu, S. W. Cheung, X. H. Liu, and T. I. Yuk, "Design of polarization reconfigurable antenna using metasurface," *IEEE Trans. Antennas Propag.*, vol. 62, no. 6, pp. 2891–2898, Jun. 2014.

[27] Y. Li, Z. Zhang, W. Chen, and Z. Feng, "Polarization reconfigurable slot antenna with a novel compact CPW-to-slotline transition for WLAN application," *IEEE Antennas Wireless Propag. Lett.*, vol. 9, pp. 252–255, 2010.

[28] P. Y. Qin, A. R. Weily, Y. J. Guo, and C. Liang, "Polarization reconfigurable U-slot patch antenna," *IEEE Trans. Antennas Propag.*, vol. 58, no. 10, pp. 3383–3388, Oct. 2010.

[29] W. Lin and H. Wong, "Wideband circular polarization reconfigurable antenna," *IEEE Trans. Antennas Propag.*, vol. 63, no. 12, pp. 5938–5944, Dec. 2015.

[30] N. Nguyen-Trong, L. Hall, and C. Fumeaux, "A frequency- and polarization-reconfigurable stub-loaded microstrip patch antenna," *IEEE Trans. Antennas Propag.*, vol. 63, no. 11, pp. 5235–5240, Nov. 2015.

[31] W. Lin and H. Wong, "Polarization reconfigurable wheel-shaped antenna with conical-beam radiation pattern," *IEEE Trans. Antennas Propag.*, vol. 63, no. 2, pp. 491–499, Feb. 2015.

[32] J. Row, W. Liu, and T. Chen, "Circular polarization and polarization reconfigurable designs for annular slot antennas," *IEEE Trans. Antennas Propag.*, vol. 60, no. 12, pp. 5998–6002, Dec. 2012.

[33] A. Panahi, X. L. Bao, K. Yang, O. O'Conchubhair, and M. J. Ammann, "A simple polarization reconfigurable printed monopole antenna," *IEEE Trans. Antennas Propag.*, vol. 63, no. 11, pp. 5129–5134, Nov. 2015.

[34] Y. Wu, C. Wu, D. Lai, and F. Chen, "A reconfigurable quadri-polarization diversity aperture-coupled patch antenna," *IEEE Trans. Antennas Propag.*, vol. 55, no. 3, pp. 1009–1012, Mar. 2007.

[35] F. Ferrero, C. Luxey, R. Staraj, G. Jacquemod, M. Yedlin, and V. Fusco, "A novel quad-polarization agile patch antenna," *IEEE Trans. Antennas Propag.*, vol. 57, no. 5, pp. 1563–1567, May 2009.

[36] L. Chang, W. Lai, J. Cheng, and C. Hsue, "A symmetrical reconfigurable multipolarization circular patch antenna," *IEEE Antennas Wireless Propag. Lett.*, vol. 13, pp. 87–90, 2014.

[37] L. Huitema, H. Wong, W. Lin, and A. Crunteanu, "Reconfigurable multi-slot antenna for bio-medical applications," in *2016 10th European Conference on Antennas and Propagation (EuCAP)*, Apr. 2016, pp. 1–4.

[38] T. Debogovic, S. Skokic, and J. Bartolic, "Electronically switchable multipolarization circular patch antenna for conformal arrays," in *2006 First European Conference on Antennas and Propagation*, Nov. 2006, pp. 1–4.

[39] P. Y. Qin, Y. J. Guo, A. R. Weily, and C. Liang, "A pattern reconfigurable U-slot antenna and its applications in MIMO systems," *IEEE Trans. Antennas Propag.*, vol. 60, no. 2, pp. 516–528, Feb. 2012.

[40] Y. Tawk, J. Costantine, F. Makhlouf, M. Nassif, L. Geagea, and C. G. Christodoulou, "Wirelessly automated reconfigurable antenna with directional selectivity," *IEEE Access*, vol. 5, pp. 802–811, 2017.

[41] S. H. Chen, J. Row, and K. Wong, "Reconfigurable square-ring patch antenna with pattern diversity," *IEEE Trans. Antennas Propag.*, vol. 55, no. 2, pp. 472–475, Feb. 2007.

[42] C. Deng, Y. Li, Z. Zhang, and Z. Feng, "A circularly polarized pattern diversity antenna for hemispherical coverage," *IEEE Trans. Antennas Propag.*, vol. 62, no. 10, pp. 5365–5369, Oct. 2014.

[43] N. Nguyen-Trong, L. Hall, and C. Fumeaux, "A frequency- and pattern-reconfigurable center-shorted microstrip antenna," *IEEE Antennas Wireless Propag. Lett.*, vol. 15, pp. 1955–1958, 2016.

[44] W. Lin, H. Wong, and R. W. Ziolkowski, "Wideband pattern-reconfigurable antenna with switchable broadside and conical beams," *IEEE Antennas Wireless Propag. Lett.*, vol. 16, pp. 2638–2641, 2017.

[45] S. Yong and J. T. Bernhard, "Reconfigurable null scanning antenna with three dimensional null steer," *IEEE Trans. Antennas Propag.*, vol. 61, no. 3, pp. 1063–1070, Mar. 2013.

[46] F. A. Dicandia, S. Genovesi, and A. Monorchio, "Null-steering antenna design using phase-shifted characteristic modes," *IEEE Trans. Antennas Propag.*, vol. 64, no. 7, pp. 2698–2706, Jul. 2016.

[47] T. Sabapathy, M. Jusoh, R. B. Ahmad, M. R. Kamarudin, and P. J. Soh, "A ground-plane-truncated, broadly steerable Yagi-Uda patch array antenna," *IEEE Antennas Wireless Propag. Lett.*, vol. 15, pp. 1069–1072, 2016.

[48] L. Y. Ji, Y. J. Guo, P. Y. Qin, S. Gong, and R. Mittra, "A reconfigurable partially reflective surface (PRS) antenna for beam steering," *IEEE Trans. Antennas Propag.*, vol. 63, no. 6, pp. 2387–2395, June 2015.

[49] Z. Lu, X. Yang, and G. Tan, "A multidirectional pattern-reconfigurable patch antenna with CSRR on the ground," *IEEE Antennas Wireless Propag. Lett.*, vol. 16, pp. 416–419, 2017.

[50] M. Li, S. Xiao, Z. Wang, and B. Wang, "Compact surface-wave assisted beam-steerable antenna based on HIS," *IEEE Trans. Antennas Propag.*, vol. 62, no. 7, pp. 3511–3519, Jul. 2014.

[51] X. Ding and B. Wang, "A novel wideband antenna with reconfigurable broadside and endfire patterns," *IEEE Antennas Wireless Propag. Lett.*, vol. 12, pp. 995–998, 2013.

[52] J. Ren, X. Yang, J. Yin, and Y. Yin, "A novel antenna with reconfigurable pattern-susing H-shaped structures," *IEEE Antennas Wireless Propag. Lett.*, vol. 14, pp. 915–918, Dec. 2015.

[53] F. Farzami, S. Khaledian, B. Smida, and D. Erricolo, "Pattern-reconfigurable printed dipole antenna using loaded parasitic elements," *IEEE Antennas Wireless Propag. Lett.*, vol. 16, pp. 1151–1154, 2017.

[54] L. Wu, A. J. Farrall, and P. R. Young, "Substrate integrated waveguide switched beam antenna," *IEEE Trans. Antennas Propag.*, vol. 63, no. 5, pp. 2301–2305, May 2015.

[55] S. Genovesi, A. D. Candia, and A. Monorchio, "Compact and low profile frequency agile antenna for multistandard wireless communication systems," *IEEE Trans. Antennas Propag.*, vol. 62, no. 3, pp. 1019–1026, Mar. 2014.

[56] S. Zhang, G. H. Huff, J. Feng, and J. T. Bernhard, "A pattern reconfigurable microstrip parasitic array," *IEEE Trans. Antennas Propag.*, vol. 52, no. 10, pp. 2773–2776, Oct. 2004.

[57] J. Row and C. Tsai, "Pattern reconfigurable antenna array with circular polarization," *IEEE Trans. Antennas Propag.*, vol. 64, no. 4, pp. 1525–1530, Apr. 2016.

[58] X. Yuan, Z. Li, D. Rodrigo, H. S. Mopidevi, O. Kaynar, L. Jofre, and B. A. Cetiner, "A parasitic layer-based reconfigurable antenna design by multi-objective optimization," *IEEE Trans. Antennas Propag.*, vol. 60, no. 6, pp. 2690–2701, Jun. 2012.

[59] D. Rodrigo, B. A. Cetiner, and L. Jofre, "Frequency, radiation pattern and polarization reconfigurable antenna using a parasitic pixel layer," *IEEE Trans. Antennas Propag.*, vol. 62, no. 6, pp. 3422–3427, Jun. 2014.

[60] A. Grau, H. Jafarkhani, and F. D. Flaviis, "A reconfigurable multiple-input multiple-output communication system," *IEEE Trans. Wireless Commun.*, vol. 7, no. 5, pp. 1719–1733, May 2008.

[61] D. Piazza, P. Mookiah, M. D'Amico, and K. R. Dandekar, "Experimental analysis of pattern and polarization reconfigurable circular patch antennas for MIMO systems," *IEEE Trans. Veh. Technol.*, vol. 59, no. 5, pp. 2352–2362, Jun. 2010.

[62] W. I. Liu, T. R. Chen, S. H. Chen, and J. S. Row, "Reconfigurable microstrip antenna with pattern and polarisation diversities," *Electron. Lett.*, vol. 43, no. 2, pp. 77–78, January 2007.

[63] W. Cao, B. Zhang, A. Liu, T. Yu, D. Guo, and K. Pan, "A reconfigurable microstrip antenna with radiation pattern selectivity and polarization diversity," *IEEE Antennas Wireless Propag. Lett.*, vol. 11, pp. 453–456, 2012.

[64] S. Raman, P. Mohanan, N. Timmons, and J. Morrison, "Microstrip-fed pattern- and polarization- reconfigurable compact truncated monopole antenna," *IEEE Antennas Wireless Propag. Lett.*, vol. 12, pp. 710–713, 2013.

[65] C. Gu, S. Gao, H. Liu, Q. Luo, T. Loh, M. Sobhy, J. Li, G. Wei, J. Xu, F. Qin, B. Sanz-Izquierdo, and R. A. Abd-Alhameed, "Compact smart antenna with electronic beam-switching and reconfigurable polarizations," *IEEE Trans. Antennas Propag.*, vol. 63, no. 12, pp. 5325–5333, Dec. 2015.

[66] T. K. Nguyen, H. H. Tran, and N. Nguyen-Trong, "A wideband dual-cavity-backed circularly polarized crossed dipole antenna," *IEEE Antennas Wireless Propag. Lett.*, vol. 16, pp. 3135–3138, 2017.

[67] W. Lin, S. L. Chen, R. W. Ziolkowski, and Y. J. Guo, "Reconfigurable, wideband, low-profile, circularly polarized antenna and array enabled by an artificial magnetic conductor ground," *IEEE Trans. Antennas Propag.*, vol. 66, no. 3, pp. 1564–1569, Mar. 2018.

[68] S. Paulotto, P. Baccarelli, F. Frezza, and D. R. Jackson, "Full-wave modal dispersion analysis and broadside optimization for a class of microstrip CRLH leaky-wave antennas," *IEEE Trans. Microw. Theory Tech.*, vol. 56, no. 12, pp. 2826–2837, Dec. 2008.

[69] Y. Li, Q. Xue, E. K.-N. Yung, and Y. Long, "The periodic half-width microstrip leaky-wave antenna with a backward to forward scanning capability," *IEEE Trans. Antennas Propag.*, vol. 58, no. 3, pp. 963–966, Mar. 2010.

[70] D. K. Karmokar and K. P. Esselle, "Periodic U-slot-loaded dual-band half-width microstrip leaky-wave antennas for forward and backward beam scanning," *IEEE Trans. Antennas Propag.*, vol. 63, no. 12, pp. 5372–5381, Dec. 2015.

[71] M. H. Rahmani and D. Deslandes, "Backward to forward scanning periodic leaky-wave antenna with wide scanning range," *IEEE Trans. Antennas Propag.*, vol. 65, no. 7, pp. 3326–3335, Jul. 2017.

[72] G. Minatti, F. Caminita, M. Casaletti, and S. Maci, "Spiral leaky-wave antennas based on modulated surface impedance," *IEEE Trans. Antennas Propag.*, vol. 59, no. 12, pp. 4436–4444, Dec. 2011.

[73] A. Lai, T. Itoh, and C. Caloz, "Composite right/left-handed transmission line metamaterials," *IEEE Microwave Mag.*, vol. 5, no. 3, pp. 34–50, Sep. 2004.

[74] Nasimuddin, Z. N. Chen, and X. Qing, "Multilayered composite right/left-handed leaky-wave antenna with consistent gain," *IEEE Trans. Antennas Propag.*, vol. 60, no. 11, pp. 5056–5062, Nov. 2012.

[75] ——, "Substrate integrated metamaterial-based leaky-wave antenna with improved boresight radiation bandwidth," *IEEE Trans. Antennas Propag.*, vol. 61, no. 7, pp. 3451–3457, Jul. 2013.

[76] H. Lee, J. H. Choi, C. T. M. Wu, and T. Itoh, "A compact single radiator CRLH-inspired circularly polarized leaky-wave antenna based on substrate-integrated waveguide," *IEEE Trans. Antennas Propag.*, vol. 63, no. 10, pp. 4566–4572, Oct. 2015.

[77] S. Otto, Z. Chen, A. Al-Bassam, A. Rennings, K. Solbach, and C. Caloz, "Circular polarization of periodic leaky-wave antennas with axial asymmetry: Theoretical proof and experimental demonstration," *IEEE Trans. Antennas Propag.*, vol. 62, no. 4, pp. 1817–1829, Apr. 2014.

[78] M. M. Sabahi, A. A. Heidari, and M. Movahhedi, "A compact CRLH circularly polarized leaky-wave antenna based on substrate-integrated waveguide," *IEEE Trans. Antennas Propag.*, vol. 66, no. 9, pp. 4407–4414, Sep. 2018.

[79] D. F. Guan, P. You, Q. Zhang, Z. H. Lu, S. W. Yong, and K. Xiao, "A wide-angle and circularly polarized beam-scanning antenna based on microstrip spoof surface plasmon polariton transmission line," *IEEE Antennas Wireless Propag. Lett.*, vol. 16, pp. 2538–2541, 2017.

[80] Q. Zhang, Q. Zhang, and Y. Chen, "High-efficiency circularly polarised leaky-wave antenna fed by spoof surface plasmon polaritons," *IET Microw. Antennas Propag.*, vol. 12, no. 10, pp. 1639–1644, 2018.

[81] S. Paulotto, P. Baccarelli, F. Frezza, and D. R. Jackson, "A novel technique for open-stopband suppression in 1-D periodic printed leaky-wave antennas," *IEEE Trans. Antennas Propag.*, vol. 57, no. 7, pp. 1894–1906, Jul. 2009.

[82] J. Liu, X. Tang, Y. Li, and Y. Long, "Substrate integrated waveguide leaky-wave antenna with H-shaped slots," *IEEE Trans. Antennas Propag.*, vol. 60, no. 8, pp. 3962–3967, Aug. 2012.

[83] Y. L. Lyu, F. Y. Meng, G. H. Yang, D. Erni, Q. Wu, and K. Wu, "Periodic SIW leaky-wave antenna with large circularly polarized beam scanning range," *IEEE Antennas Wireless Propag. Lett.*, vol. 16, pp. 2493–2496, 2017.

[84] D. K. Karmokar, Y. J. Guo, P. Y. Qin, K. P. Esselle, and T. S. Bird, "Forward and backward beam-scanning tri-band leaky-wave antenna," *IEEE Antennas Wireless Propag. Lett.*, vol. 16, pp. 1891–1894, 2017.

[85] J. T. Williams, P. Baccarelli, S. Paulotto, and D. R. Jackson, "1-D combline leaky-wave antenna with the open-stopband suppressed: Design considerations and com-

parisons with measurements," *IEEE Trans. Antennas Propag.*, vol. 61, no. 9, pp. 4484–4492, Sep. 2013.

[86] Y. L. Lyu, X. X. Liu, P. Y. Wang, D. Erni, Q. Wu, C. Wang, N. Y. Kim, and F. Y. Meng, "Leaky-wave antennas based on noncutoff substrate integrated waveguide supporting beam scanning from backward to forward," *IEEE Trans. Antennas Propag.*, vol. 64, no. 6, pp. 2155–2164, Jun. 2016.

[87] Y. Dong and T. Itoh, "Composite right/left-handed substrate integrated waveguide and half mode substrate integrated waveguide leaky-wave structures," *IEEE Trans. Antennas Propag.*, vol. 59, no. 3, pp. 767–775, Mar. 2011.

[88] W. Cao, Z. N. Chen, W. Hong, B. Zhang, and A. Liu, "A beam scanning leaky-wave slot antenna with enhanced scanning angle range and flat gain characteristic using composite phase-shifting transmission line," *IEEE Trans. Antennas Propag.*, vol. 62, no. 11, pp. 5871–5875, Nov. 2014.

[89] G. C. Wu, G. M. Wang, H. X. Peng, X. J. Gao, and J. G. Liang, "Design of leaky-wave antenna with wide beam-scanning angle and low cross-polarisation using novel miniaturised composite right/left-handed transmission line," *IET Microw. Antennas Propag.*, vol. 10, no. 7, pp. 777–783, 2016.

[90] A. Kianinejad, Z. N. Chen, and C. W. Qiu, "A single-layered spoof-plasmon-mode leaky wave antenna with consistent gain," *IEEE Trans. Antennas Propag.*, vol. 65, no. 2, pp. 681–687, Feb. 2017.

[91] C. S. Prasad and A. Biswas, "Dielectric image line-based leaky-wave antenna for wide range of beam scanning through broadside," *IEEE Trans. Antennas Propag.*, vol. 65, no. 8, pp. 4311–4315, Aug. 2017.

[92] S. L. Chen, F. Wei, P. Y. Qin, Y. J. Guo, and X. Chen, "A multi-linear polarization reconfigurable unidirectional patch antenna," *IEEE Trans. Antennas Propag.*, vol. 65, no. 8, pp. 4299–4304, Aug. 2017.

[93] Z. Chen and H. Wong, "Liquid dielectric resonator antenna with circular polarization reconfigurability," *IEEE Trans. Antennas Propag.*, vol. 66, no. 1, pp. 444–449, Jan. 2018.

[94] Y. J. Guo, P. Y. Qin, S. L. Chen, W. Lin, and R. W. Ziolkowski, "Advances in reconfigurable antenna systems facilitated by innovative technologies," *IEEE Access*, vol. 6, pp. 5780–5794, 2018.

[95] L. Ji, P. Y. Qin, Y. J. Guo, C. Ding, G. Fu, and S. Gong, "A wideband polarization reconfigurable antenna with partially reflective surface," *IEEE Trans. Antennas Propag.*, vol. 64, no. 10, pp. 4534–4538, Oct. 2016.

[96] M. R. M. Hashemi and T. Itoh, "Composite right/left-handed leaky-wave transmission-line with switchable polarization capability," in *2011 41st European Microwave Conference*, Oct. 2011, pp. 495–498.

[97] Y. Dong and T. Itoh, "Substrate integrated composite right-/left-handed leaky-wave structure for polarization-flexible antenna application," *IEEE Trans. Antennas Propag.*, vol. 60, no. 2, pp. 760–771, Feb. 2012.

[98] R. O. Ouedraogo, E. J. Rothwell, and B. J. Greetis, "A reconfigurable microstrip leaky-wave antenna with a broadly steerable beam," *IEEE Trans. Antennas Propag.*, vol. 59, no. 8, pp. 3080–3083, Aug. 2011.

[99] R. Guzman-Quiros, J. L. Gomez-Tornero, A. R. Weily, and Y. J. Guo, "Electronically steerable 1-D Fabry-Perot leaky-wave antenna employing a tunable high

impedance surface," *IEEE Trans. Antennas Propag.*, vol. 60, no. 11, pp. 5046–5055, Nov. 2012.

[100] D. K. Karmokar, K. P. Esselle, and S. G. Hay, "Fixed-frequency beam steering of microstrip leaky-wave antennas using binary switches," *IEEE Trans. Antennas Propag.*, vol. 64, no. 6, pp. 2146–2154, Jun. 2016.

[101] K. Zhang, H. Yu, X. Ding, and Q. Wu, "Experimental validation of active holographic metasurface for electrically beam steering," *Opt. Express*, vol. 26, no. 5, pp. 6316–6324, Mar. 2018.

[102] J. M. Montero, A. M. Ocampo, and N. J. G. Fonseca, "C-band multiple beam antennas for communication satellites," *IEEE Trans. Antennas Propag.*, vol. 63, no. 4, pp. 1263–1275, Apr. 2015.

[103] R. Guzman-Quiros, J. L. Gomez-Tornero, A. R. Weily, and Y. J. Guo, "Electronic full-space scanning with 1-D Fabry-Perot LWA using electromagnetic band-gap," *IEEE Antennas Wireless Propag. Lett.*, vol. 11, pp. 1426–1429, 2012.

[104] M. Wang, H. F. Ma, H. C. Zhang, W. X. Tang, X. R. Zhang, and T. J. Cui, "Frequency-fixed beam-scanning leaky-wave antenna using electronically controllable corrugated microstrip line," *IEEE Trans. Antennas Propag.*, vol. 66, no. 9, pp. 4449–4457, Sep. 2018.

[105] L. Chang, Y. Li, Z. Zhang, and Z. Feng, "Reconfigurable 2-bit fixed-frequency beam steering array based on microstrip line," *IEEE Trans. Antennas Propag.*, vol. 66, no. 2, pp. 683–691, Feb. 2018.

[106] S. Lim, C. Caloz, and T. Itoh, "Electronically scanned composite right/left handed microstrip leaky-wave antenna," *IEEE Microw. Wireless Compon. Lett.*, vol. 14, no. 6, pp. 277–279, Jun. 2004.

[107] A. Suntives and S. V. Hum, "A fixed-frequency beam-steerable half-mode substrate integrated waveguide leaky-wave antenna," *IEEE Trans. Antennas Propag.*, vol. 60, no. 5, pp. 2540–2544, May 2012.

[108] B. Che, T. Jin, D. Erni, F. Meng, Y. Lyu, and Q. Wu, "Electrically controllable composite right/left-handed leaky-wave antenna using liquid crystals in PCB technology," *IEEE Trans. Compon. Packag. Manuf. Technol.*, vol. 7, no. 8, pp. 1331–1342, Aug. 2017.

[109] R. Garg, P. Bhartia, I. J. Bahl, and A. Ittipiboon, *Microstrip antenna design handbook*. Artech house, 2001.

[110] Y. J. Guo, A. Paez, R. A. Sadeghzadeh, and S. K. Barton, "A circular patch antenna for radio LAN's," *IEEE Trans. Antennas Propag.*, vol. 45, no. 1, pp. 177–178, Jan 1997.

[111] D. M. Pozar, "Microstrip antennas," *Proc. IEEE*, vol. 80, no. 1, pp. 79–91, Jan. 1992.

[112] G.-Y. Chen and J.-S. Sun, "A printed dipole antenna with microstrip tapered balun," *Microw. Opt. Technol. Lett.*, vol. 40, no. 4, pp. 344–346, 2004.

[113] D. Sun and L. You, "A broadband impedance matching method for proximity-coupled microstrip antenna," *IEEE Trans. Antennas Propag.*, vol. 58, no. 4, pp. 1392–1397, Apr. 2010.

[114] Y. Liu, S. Chen, Y. Ren, J. Cheng, and Q. H. Liu, "A broadband proximity-coupled dual-polarized microstrip antenna with l-shape backed cavity for x-band applications," *Int. J. Electron. Commun.*, vol. 69, no. 9, pp. 1226–1232, 2015.

[115] C. Caloz and T. Itoh, *Electromagnetic Metamaterials: Transmission Line Theory and Microwave Applications.* John Wiley & Sons, 2005.

[116] H. Mosallaei and K. Sarabandi, "Design and modeling of patch antenna printed on magneto-dielectric embedded-circuit metasubstrate," *IEEE Trans. Antennas Propag.*, vol. 55, no. 1, pp. 45–52, Jan. 2007.

[117] H. W. Johnson, M. Graham *et al.*, *High-speed digital design: a handbook of black magic.* Prentice Hall Upper Saddle River, NJ, 1993, vol. 1.

[118] D. K. Karmokar, Y. J. Guo, P. Y. Qin, S. L. Chen, and T. S. Bird, "Substrate integrated waveguide-based periodic backward-to-forward scanning leaky-wave antenna with low cross-polarization," *IEEE Trans. Antennas Propag.*, vol. 66, no. 8, pp. 3846–3856, Aug. 2018.

[119] C. A. Balanis, *Antenna Theory: Analysis and Design.* John Willey & Sons, 1997.

[120] ——, "Antenna theory: a review," *Proc. IEEE*, vol. 80, no. 1, pp. 7–23, Jan. 1992.

[121] T. Oh, Y. Lim, C. Chae, and Y. Lee, "Dual-polarization slot antenna with high cross-polarization discrimination for indoor small-cell MIMO systems," *IEEE Antennas Wireless Propag. Lett.*, vol. 14, pp. 374–377, 2015.

[122] H.-R. Chuang and L.-C. Kuo, "3-D FDTD design analysis of a 2.4-Ghz polarization-diversity printed dipole antenna with integrated balun and polarization-switching circuit for WLAN and wireless communication applications," *IEEE Trans. Microw. Theory Tech.*, vol. 51, no. 2, pp. 374–381, Feb. 2003.

[123] S. L. Chen, P. Y. Qin, C. Ding, and Y. J. Guo, "Cavity-backed proximity-coupled reconfigurable microstrip antenna with agile polarizations and steerable beams," *IEEE Trans. Antennas Propag.*, vol. 65, no. 10, pp. 5553–5558, Oct. 2017.

[124] G. V. Eleftheriades and K. G. Balmain, *Negative-Refraction Metamaterials: Fundamental Principles and Applications*. John Wiley & Sons, 2005.

[125] N. Engheta and R. W. Ziolkowski, *Metamaterials: Physics and Engineering Explorations*. John Wiley & Sons, 2006.

[126] Y. Dong and T. Itoh, "Metamaterial-based antennas," *Proc. IEEE*, vol. 100, no. 7, pp. 2271–2285, Jul. 2012.

[127] Y. Cai, K. Li, Y. Yin, S. Gao, W. Hu, and L. Zhao, "A low-profile frequency reconfigurable grid-slotted patch antenna," *IEEE Access*, vol. 6, pp. 36 305–36 312, 2018.

[128] D. M. Pozar, "Microwave Engineering." 3rd ed., New York: Wiley, 2005.